UNIVERSITY OF CALIFORNIA, SAN DIEGO

Measurement of the Anisotropic Temperature Relaxation

Rate in a Magnetized Pure Electron Plasma

A dissertation submitted in partial satisfaction of the

requirements for the degree Doctor of Philosophy
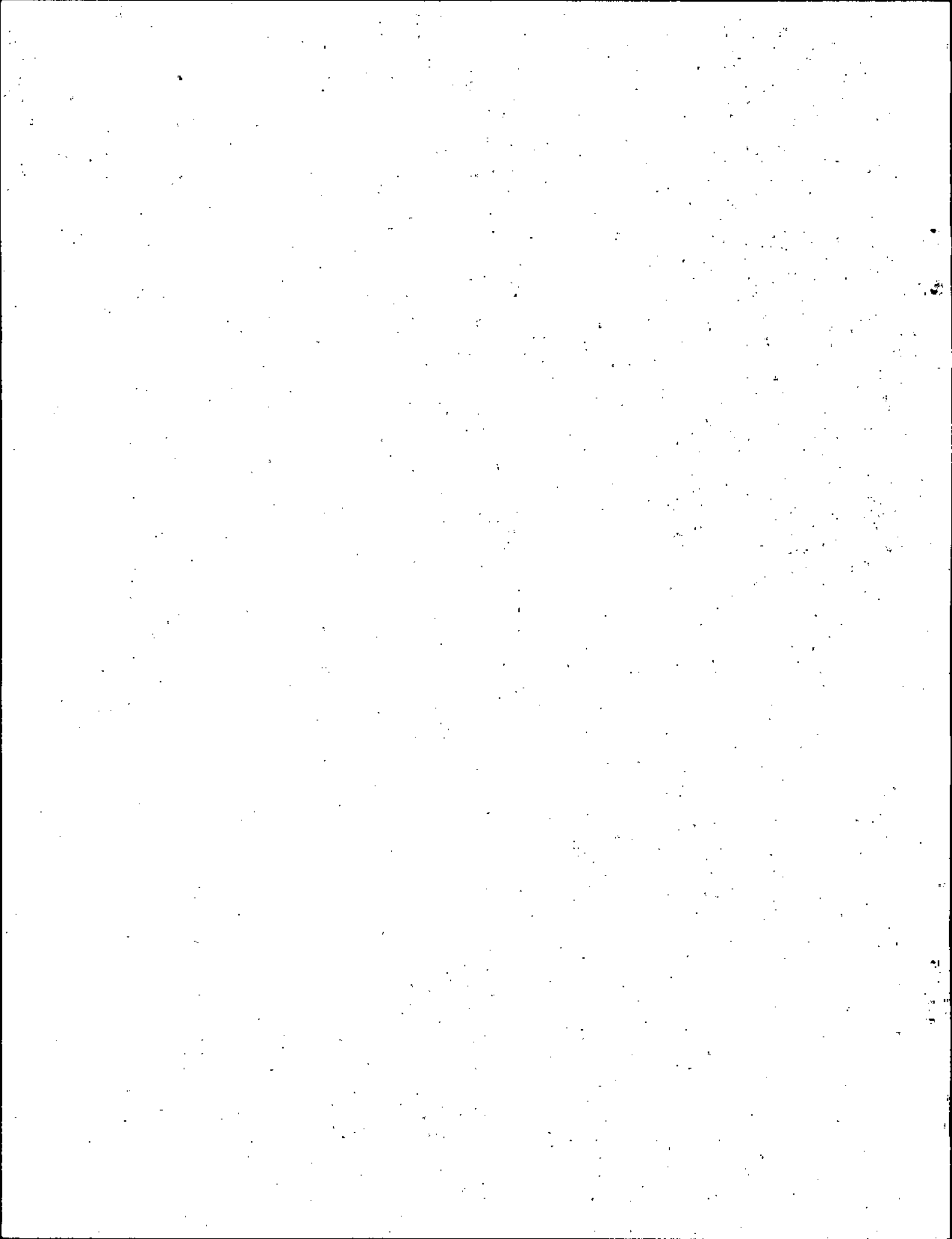
in Physics

by

Alan Walter Hyatt

Committee in charge:

    Professor John H. Malmberg, Chairperson
    Professor Thomas M. O'Neil
    Professor Ralph H. Lovberg
    Professor David R. Miller
    Professor Charles W. Van Atta

1988

The dissertation of Alan Walter Hyatt is approved,

and it is acceptable in quality and form for publica-

tion on microfilm:

David R. Miller

Charles W. Van Atta

Thomas O'Neil

Ralph H. Porberg

John H. Malmberg
                                    Chairperson

University of California, San Diego

1988

iii

TABLE OF CONTENTS

LIST OF FIGURES

ACKNOWLEDGMENTS

First and foremost, I would like to thank my advisor, Prof. John Malmberg, for an invaluable education. His knowledge and insight, of which he gives freely, extends far beyond the discipline of physics. I consider it a privilege to have had the opportunity to learn the scientific method from him. I would also like to thank Dr. Fred Driscoll for his perceptive direction, and who, along with my fellow student Kevin Fine, designed and constructed the device used in this study. I thank Prof. Tom O'Neil for helpful theoretical discussions and for his effective advocacy of the theoretical viewpoint.

In addition, I would like to thank the plasma group post-docs and my fellow students, most especially Kevin Fine and Paul Hjorth, for their help and encouragement over the course of my studies. My graduate experience is all the richer for the spirited discussion (some of which concerned physics) that we shared.

I also want to thank Ms. Annetta Whiteman, who performed prodigies in the typing of this manuscript, and Ms. JoAnn Christina, who gracefully keeps the Malmberg group functioning smoothly.

Finally, I would most especially like to thank my family for their wonderful support and encouragement over the long road from neophyte to professional. The journey would have been bleak indeed without them.

VITA

July 22, 1948 - Born - Los Angeles, California

1966-1971   University of California, San Diego

1971-1978   Draftsman, County of San Diego

1978   B.A., University of California, San Diego

1978-1986   Draftsman, County of San Diego

1978-1988   Ph.D., University of California, San Diego

PUBLICATIONS

"The Pure Electron Plasma at Cryogenic Temperatures" (abstract) (with J. H. Malmberg and C. F. Driscoll), Bull. Am. Phys. Soc. 28, 1047 (1983).

"The Cryogenic Pure Electron Plasma" (with J. H. Malmberg, T. M. O'Neil and C. F. Driscoll), Proceedings of the 1984 Sendai Symposium on Non-Linear Phenomena, 31 (1984).

"Observation of Anisotropic Temperature Relaxation" (abstract), (with J. H. Malmberg, C. F. Driscoll, K. S. Fine, B. R. Beck and D. L. Eggleston), Bull. Am. Phys. Soc. 30, 1552 (1985).

"Injection Techniques for a Pure Electron Plasma" (abstract) (with B. R. Beck and J. H. Malmberg), Bull. Am. Phys. Soc. 31, 1391 (1986).

"Observation of Anisotropic Temperature Relaxation" (abstract), (with C. F. Driscoll and J. H. Malmberg), Bull. Am. Phys. Soc. 31, 1391 (1986).

"Measurement of the Anisotropic Temperature Relaxation Rate in a Pure Electron Plasma" (abstract), (with C. F. Driscoll and J. H. Malmberg), Bull. Am. Phys. Soc. 32, 1755 (1987).

"Measurement of the Anisotropic Temperature Relaxation Rate in a Pure Electron Plasma" (with C. F. Driscoll and J. H. Malmberg), Phys. Rev. Lett. 59, 2975 (1987).

FIELDS OF STUDY

Major Field: Physics

Studies in Plasma Physics
Professors John H. Malmberg, Thomas M. O'Neil and
William B. Thompson

Studies in Mechanics
Professors Keith A. Brueckner and William B. Thompson

Studies in Electromagnetism
Professor Robert A. Swanson

Studies in Quantum Mechanics
Professors David Y. Wong, William B. Frazer and
Harry Suhl

Studies in Thermodynamics
Professor Shang-keng Ma

Studies in Relativity and Cosmology
Professor Robert J. Gould

ABSTRACT OF THE DISSERTATION

Measurement of the Anisotropic Temperature Relaxation

Rate in a Magnetized Pure Electron Plasma

by

Alan Walter Hyatt

Doctor of Philosophy in Physics

University of California, San Diego, 1988

Professor John H. Malmberg, Chairperson

The anisotropic temperature relaxation rate is obtained from the measured time evolution of $T_\perp$ and $T_\parallel$ in a magnetized plasma consisting of only electrons. The magnetic field defines the parallel axis. The velocity space anisotropy is induced in a plasma which has evolved to a quiescent Maxwellian state. An essentially one-dimensional axial compression (or expansion) changes $T_\parallel$ while $T_\perp$ remains essentially unchanged. The time scale over which the compression occurs is short compared to the electron-electron collision time. The nature of the compression is such that the parallel velocity distribution remains approximately Maxwellian after the compression, albeit with a different temperature. The perpendicular velocity

distribution remains essentially unaffected during the compression since few momentum exchanging collisions occur.

After the compression is completed the temperature anisotropy relaxes to a final equilibrium on the collisional time scale. The relaxation rate is obtained from measurements of $T_\perp$ and $T_\parallel$ as functions of time. The relaxation of the anisotropy is found to be nearly exponential.

The relaxation rate is obtained as a function of the measured plasma density and the final equilibrium temperature. The measured rate is compared with the absolute (no adjutable parameters) prediction of a Fokker-Planck theory calculated in the weak field regime by Ichimaru and Rosenbluth, and which is modified by a strong magnetic field approximation due to Montgomery, Joyce and Turner. The measured rate is also compared with the theoretical prediction of Ichimaru and Rosenbluth without the strong magnetic field approximation. The measured rate and the prediction of the modified theory are found to statistically agree to about 5%. The unmodified theory predicts a rate which is over 20% larger than the measured rate.
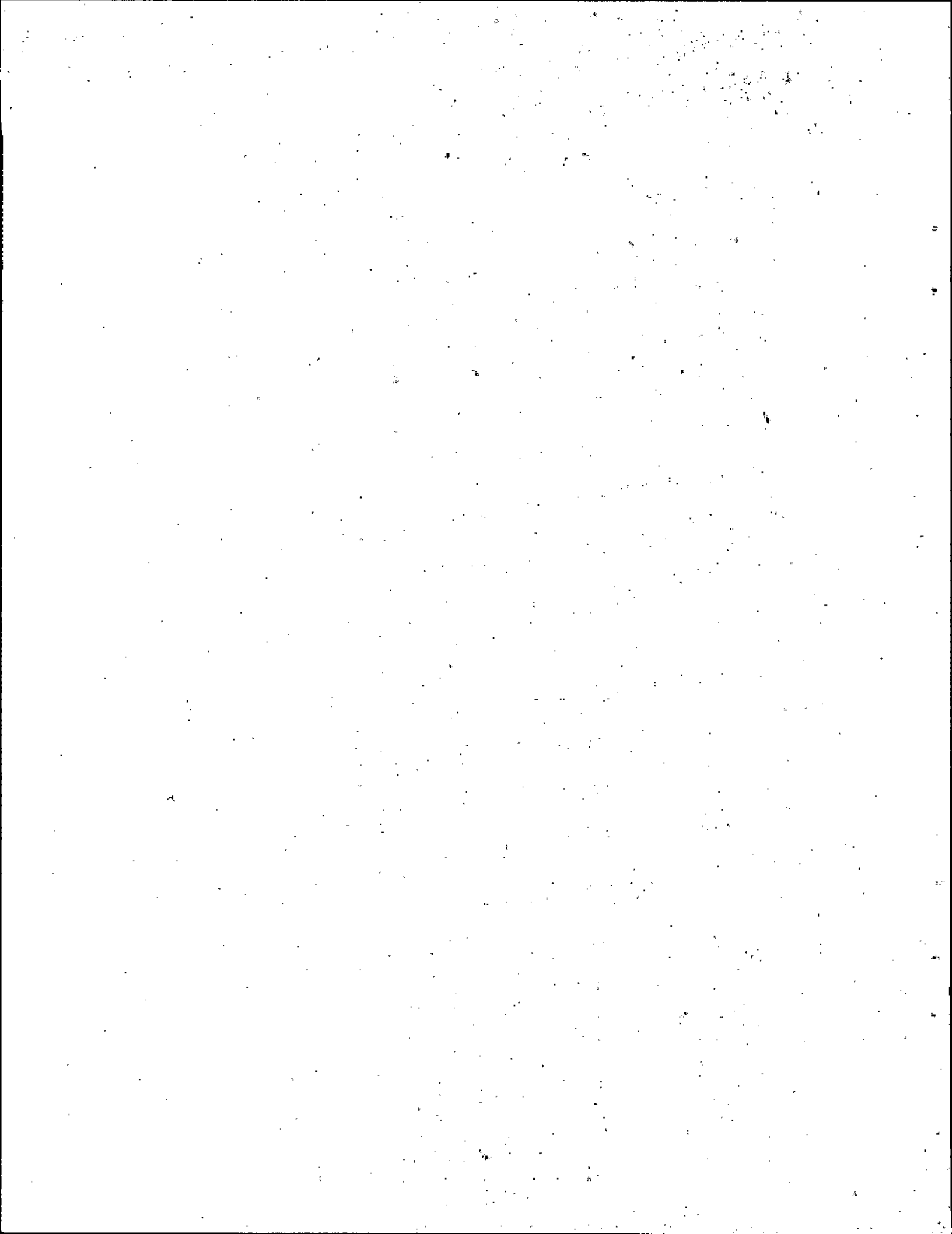
I. Introduction

In this thesis I describe a simple and direct experiment which measures the rate at which an experimentally induced velocity space anisotropy in a magnetized pure electron plasma relaxes to equilibrium via electron-electron collisions. This anistropy is characterized by $T_{\perp} \neq T_{\parallel}$, the temperature associated with the degrees of freedom perpendicular and parallel to the applied magnetic field.

This anisotropic temperature relaxation is a specific case of collisional velocity space transport in plasmas. The study of velocity space transport in plasmas involves investigation into how the mutual interactions of a system of charged particles modify the particles' distribution of velocities in time. Collisional transport refers to particles interacting with particles, or more properly, with properties of the plasma which reflect the discrete particle nature of the plasma, such as the electric field fluctuations caused by the random motions of the particles. Collective transport, the interaction of particles with averaged, fluid properties of the plasma, can also change the distribution function in time.

Collisional velocity space transport is of fundamental interest to plasma physics. A few of the areas of plasma physics in which this transport can play a dominant role are in determining the rate at which equipartition of energy occurs in plasmas, the rate at which particles are scattered into the velocity space loss cone in a magnetic

1

mirror confinement device, and in determining the momentum transfer between electrons and ions. This momentum scattering underlies the concept of plasma resistivity, and hence is important to the Ohmic heating schemes employed in tokamaks. Each of these effects depend upon the collisional transfer of momentum among the plasma particles.

A theoretical description of collisional velocity space transport in plasmas has been the subject of continuing interest for over 70 years. Small momentum transfer collisions are thought to dominate, which has led to a Fokker-Planck formulation of the transport process. Such a formulation neglects the effects of the (assumed) rare large momentum transfer collisions. In fact, there are many assumptions and approximations made of necessity when rates are analytically calculated for specific cases from general Fokker-Planck theories.

While there have been many experimental measurements of configuration space transport, there have been only a few experimental measurements of collisional velocity space transport rates in plasmas. For the most part, these experiments have uncertainties of the order of unity or larger. Hiskes and Futch[1] present measurements of the rate at which ions are transported into the loss cone of a magnetic mirror for several devices, and find that at best the agreement with collisional theory is in the factor-of-two range. The theoretical rates are generated by a Fokker-Planck code which requires

the input of initial conditions, and in some cases, there are free parameters which are adjusted to bring the output of the code into agreement with some measured quantity. Burke and Post[2] present the results of their experiments on fast test ions slowing in a neutral plasma, and contrast these results with those of other similar experiments. Their results differ from theory by a factor of 3 with uncertainties of order unity. The other experimental results referred to by Burke and Post differ from theory by factors of 1/3 to 8.

The resistivity measurements of Lin et al. and Mohler[3] together agree quite well with the theoretical predictions of Spitzer and Härm,[4] over a reasonable range of temperatures and densities, with experimental accuracies on the order of 10-20%. They measure the average conductivity in the shock wave front of a gas. This shock wave is produced in a shock tube. The average charge density and shock wave temperature are calculated from the measured Mach number. Although a resistivity measurement does not measure a transport rate per se, it does measure one of the bedrocks of collisional velocity space transport in plasmas - the effective cross-section for momentum transfer between charged particles in a plasma.

In our experiment we directly measure the relevant parameters of charge density, and the temperatures $T_\perp$ and $T_\parallel$ as they relax to a common equilibrium. Further, the experimental conditions are contrived so that both the density and total thermal energy remain

3

essentially constant in space over the measured volume and constant in time over the relaxation to final thermal equilibrium. To my knowledge, this experiment is the first measurement of this relaxation rate, and is the first unambiguous precision measurement of collisional velocity space transport. I compare the experimental results, obtained over a two decade range of measured relaxation rates, with a Fokker-Planck theoretical calculation of those rates, and find absolute (there are no adjustable parameters) agreement to about 5%.

This thesis is organized as follows. The second chapter discusses the basis of the Fokker-Planck approach and the relevant theory, including the anisotropic temperature relaxation rate calculation. This rate is calculated in the weak magnetic field limit. The approximation which suitably modifies this rate for application to the strongly magnetized regime of our pure electron plasma is also discussed. The third chapter describes the experimental apparatus, its operation, and the equilibrium pure electron plasma it produces. The diagnostics for the density and temperature $T_\perp$ and $T_\parallel$ are also discussed. The fourth chapter describes the experiment and how the anisotropic temperature relaxation rates are measured. The method of analysis whereby the raw relaxation data is reduced to yield a rate which can be compared with theory is also discussed. The fifth chapter presents a summary of the results, compares those results with theory and states the conclusions.

II. Theory

A general theory of collisional velocity space transport in magnetized plasmas has been developed by Ichimaru and Rosenbluth[5,6] (I-R). A similar theory, addressed to a single species plasma in a uniform neutralizing background, has been developed by Montgomery, Joyce and Turner[7,8] (M-J-T). I-R calculate the rate for our specific anisotropy, although only for a weak magnetic field. M-J-T have proposed an approximation that in general will allow the use of non-magnetized rate calculations to be applied in the strong field regime. Both theories are based upon the Fokker-Planck formalism.

The Fokker-Planck formalism calculates the statistical evolution of a particle's (or a distribution of particles') phase space coordinates in time as the particle is subjected to rapidly fluctuating forces. When applied in configuration space, the Fokker-Planck formalism gives rise to Brownian motion, such as that of a heavy particle in a fluid, first theoretically described by Einstein.[9] This motion is determined by two effects: a frictional opposition to the particle motion due to the relative wind of fluid the particle sees in its own frame, and a diffusive "random walk" in space due to the random accelerations produced by the fluctuations. Particles also display Brownian motion in velocity space; the particle's velocity undergoes a frictional slowing, and a diffusive random walk in velocity space. These two effects tend to drive an ensemble of Brownian particles

5

into equilibrium with the fluid: the average relative velocity of the Brownian particles with respect to the fluid tends to zero, and the average kinetic energy of the Brownian particles tends to that of the fluid particles.

A. The Maxwell-Boltzmann Formalism

Historically, transport in gases of particles (including particles with interact via a $1/r$ potential, such as unmagnetized plasmas and stellar clusters) was first treated theoretically by the Maxwell-Boltzmann formalism. This formalism, embodied in the Boltzmann equation,[10] generalizes the Liouville equation to calculate the rate of change of the single particle distribution function in a volume element of phase space due to particle interactions which are treated as isolated two-body collisions. Individual collisions can move participants into or out of the phase space volume element. The Boltzmann equation calculates the rate of change of the distribution function due to these collisions by summing over probabilities of occurrence of all collisions which transport particles into or out of the volume element. This probability is parameterized by the impact parameter b, the distance of closest approach in the absence of any interaction.

The Maxwell-Boltzmann formalism should work very well in calculating transport coefficients for gases of particles whose interactions are such that the average interparticle separation is much larger than the interaction range, and whose average kinetic energy is

6

much larger than its average potential energy. Chapman and Enskog[11] devised a general method of solving the integro-differential Boltzmann equation, and show that the Boltzmann equation is well verified experimentally for several molecular gases, where the interaction potentials drop off quite sharply.

A plasma (or a stellar cluster) is a gas of particles which undergo long range interactions. One aspect of the long-range interaction is the Debye shielding effect, which sets the effective range over which thermal particles can interact at about the Debye length, λ_D. By definition, the plasma parameter $\Lambda \equiv n\lambda_D^3$ (the number of particles within the interaction range of a given particle), where n is the particle density, must be much larger than unity for a charged gas to be a plasma. (In our pure electron plasmas $\Lambda \simeq 10^6 - 10^8$.) All particles within a Debye length about a given particle are somewhat correlated in position with that particle, and are more or less simultaneously interacting with each other and with the given particle.

At first glance, it would appear that the Maxwell-Boltzmann formalism is ill-suited to describe transport in $1/r$ potential gases. However, by estimating the cumulative effect of all the two body collisions (as if each occurred in isolation) on a thermal particle which traverses a Debye sphere, it can easily be shown that the net effect of this traversal (excluding the rare single large angle scattering collision) is only a very small change in the particle's velocity. From

classical mechanics and the Coulomb potential, we see that, in the center of mass frame, the relative velocity vector, v, is rotated by a single collision through an angle

$$\theta = 2 \tan^{-1}(q_1 q_2 / bmv^2) \qquad (2.A.1)$$

in a plane defined by the initial conditions. The q_i's are the respective charges, m is the reduced mass, and b is the impact parameter. When $b \sim \lambda_D$, then $\theta \sim \Lambda^{-1}$. Even for the relatively rare case $b \sim n^{-1/3}$, then $\theta \sim \Lambda^{-2/3}$, which is still quite small. Assume Λ separate collisions with random θ-plane orientations, and neglect the effect of the relatively rare collision with $b \lesssim n^{-1/3}$ by assuming $\theta \sim \Lambda^{-1}$ for all collisions. The individual θ's statistically add to $\Lambda^{1/2} \theta$, which gives an estimate of θ_T, the total deflection a thermal particle suffers in crossing a Debye sphere, as $\Lambda^{-1/2} \lesssim \theta_T$. To this approximation, the total deflection is then on the order of 10^{-3} radians (less than 1°) for most plasmas.

(Slightly more rigorous estimates of θ_T lead to an estimate of the "mean-free path" (the distance a thermal particle must travel before the effects of distant collisions add to give $\theta_T \sim$ unity) of m.f.p. $\sim \Lambda \lambda_D / \ln \Lambda$. A similar estimate of the mean free path traveled before a single large angle scattering collision occurs gives a m.f.p. $\sim \Lambda \lambda_D$. Since $\ln \Lambda \sim 10\text{-}20$, large scattering collisions can be neglected to an accuracy of $\sim 10\%$ or so.)

8

The fact that a particle's trajectory is hardly perturbed by all its surrounding neighbors as it passes through their mutual interaction region means that to good approximation the interaction between any two particles may be treated as if it occurs in isolation. This, in turn, implies that the Maxwell-Boltzmann formalism should be adequate to describe the transport properties of a plasma with a sufficiently large Λ, providing the interaction is somehow cut off at a range of about λ_D. This can be done either by invoking the dielectric nature of the plasma in order to modify the interaction potential,[12,13] or by simply setting λ_D as the upper limit of possible impact parameters in the Boltzmann equation.[14]

B. The Fokker-Planck Formalism

The fact that the sum of many individual collisions in a plasma leads to only a small deflection of a particle's trajectory (i.e., a small $\Delta\vec{v}$), and that large angle collisions are relatively rare, has led to the development of a Fokker-Planck formulation of transport in a plasma. This formalism should be more generally valid in that transport need not be calculated from considerations of isolated two-body interactions. In practice, however, the complexity of calculating the friction and diffusion coefficients has led to essentially the same assumption of isolated trajectories, either in assuming only small deflections are important and expanding the Boltzmann equation in powers of small Δv, which yields a Fokker-Planck equation,[7,8,13,15-17] or

in the calculation of total force field fluctuations at the particle position.[5,6,18,20-23] Calculations from either approach have led to identical results for the friction and diffusion coefficients, at least when there is no magnetic field. The main utility of the Fokker-Planck formulation, as presently applied to plasmas (and gravitating particles), seems to be in the display of the frictional and diffusive (Brownian) nature of the transport.

The Fokker-Planck coefficients for an unmagnetized plasma with an arbitrary velocity distribution were first derived by Rosenbluth, McDonald and Judd,[17] and Thompson and Hubbard,[22,23] using the Boltzmann and net force approaches, respectively. The Lenard-Balescu equation[24,25] (the Vlasov equation generalized to include two particle interactions) can be put into Fokker-Planck form.

The Fokker-Planck equation is usually derived from the following assumptions: 1) the particle velocity changes only infinitesimally on a time scale τ, which is much longer than characteristic time scale of a force field fluctuation; and 2) the fluctuations felt by the particle depend only upon the particle's phase space coordinates, not on its past history (a Markov process). (See ref. 6 for a derivation of the Fokker-Planck equation from these assumptions.) The Fokker-Planck equation, in the absence of external fields and spatial gradients, is

$$\frac{\partial f(\vec{v})}{\partial t} = -\nabla_{\vec{v}} \cdot (\vec{F}(\vec{v}) f(\vec{v})) + \frac{1}{2} \nabla_{\vec{v}} \nabla_{\vec{v}} : (\vec{\vec{D}}(\vec{v}) f(\vec{v})) \ , \qquad (2.\,B.\,1)$$

where $f(\vec{v})$ is the velocity distribution function, and $\vec{F}(\vec{v})$ and $\vec{\vec{D}}(\vec{v})$ respectively, are the coefficients of friction and diffusion in velocity space. These coefficients are given by

$$\vec{F}(\vec{v}) = \frac{\langle \Delta \vec{v} \rangle}{\tau} \ , \qquad (2.\,B.\,2)$$

$$\vec{\vec{D}}(\vec{v}) = \frac{\langle \Delta \vec{v} \, \Delta \vec{v} \rangle}{\tau} \ . \qquad (2.\,B.\,3)$$

The "$\langle \ \rangle$" indicates an ensemble average of the resulting net $\Delta \vec{v}$ and $\Delta \vec{v} \, \Delta \vec{v}$ calculated from the effects of the fluctuating force on the particle over the (relatively) long time τ. When the fluctuating force approach is taken, the calculation of $\Delta \vec{v}$ is performed by integrating the fluctuating forces on the particle along its trajectory. This calculation is fairly straightforward when a magnetic field is absent; the trajectory is then calculated by expanding the force about the unperturbed trajectory, which is a straight line. The unperturbed trajectory becomes a helical path when a magnetic field is present; this increases the complexity of the calculation considerably, except when the field strength is such that r_g , the particle gyroradius, is much greater than λ_D . In this small field limit, the trajectory can be approximated as straight. In addition, the dielectric shielding properties of the plasma are modified by the magnetic field.

Several workers,[26-29] as well as I-R and M-J-T, have developed Fokker-Planck approaches to transport in magnetized plasmas. The rest of this chapter, however, is devoted to the theory of I-R, and a discussion of an approximation proposed by M-J-T useful in simplifying the evaluation of the Fokker-Planck coefficients when the plasma is strongly magnetized.

C. The Theory of Ichimaru and Rosenbluth

Rather than re-deriving the general magnetized theory of I-R, which can be found in detailed form in refs. 5-6, the discussion is limited to some of the features and approximations within the theory. The method of calculating energy relaxation rates is given, and the results of the specific calculation of the relaxation of the anisotropic temperature distribution, assuming a bi-Maxwellian velocity distribution function, is discussed.

The I-R procedure for calculating $\langle \Delta \vec{v}(\tau) \rangle$ and $\langle \Delta \vec{v}(\tau) \, \Delta \vec{v}(\tau) \rangle$ is to calculate $\vec{v}(t)$ from the time integration of the Taylor expanded total electric field $\vec{E}_T(\vec{r}_o(t), t)$ about the particle's unperturbed trajectory, $\vec{r}_o(t)$. By definition, $\Delta \vec{v}(t) = \vec{v}(t) - \vec{v}(0)$. This expansion is in accord with the Fokker-Planck assumption that $\Delta \vec{v}(\tau)$ becomes infinitesimal as τ becomes small. The total electric field is approximated as

$$\vec{E}_T(\vec{r}_o(t), t) = \vec{E}_{ind}(\vec{r}_o(t), t) + \vec{E}_f(\vec{r}_o(t), t) . \qquad (2.C.1)$$

$\vec{E}_{ind}(\vec{r}_o(t), t)$ is the polarization field the particle induces in the plasma. This field is calculated from all the rest of the particles treated as a dielectric medium responding to a moving "test" charge. This medium cannot respond infinitely fast, since it too is composed of moving particles. Therefore, as the medium attempts to shield the moving test particle, the test particle has moved away from the symmetry center of the shielding. The test particle thus sees a retarding electric field induced by its own motion through the dielectric medium. On the other hand, the fluctuating field, $\vec{E}_f(\vec{r}_o(t), t)$, is calculated at the position of the test charge as if the test charge was not present; $\vec{E}_f$ is then due only to the statistical fluctuations in the dielectric medium. The spectrum of $\vec{E}_f$ is assumed to be stationary in time and space. I-R calculate the fluctuating field at a particular point due to the motion of all the particles, each acting as a test particle moving along unperturbed trajectories and interacting with the dielectric medium.

From the above discussion it is easy to see that $|\vec{E}_{ind}| \neq 0$ for any test particle with nonzero velocity, and $\langle \vec{E}_f \rangle = 0$, as long as the plasma has no spatial gradients. The brackets refer to an ensemble average. The ensemble fluctuations of $\vec{E}_{ind}$ can be neglected in favor of the average value.

The quantity $\Delta \vec{v}$ is then calculated as an integration of $\vec{E}_T$ by expanding $\vec{E}_T(\vec{r}(t), t)$ to second order along the unperturbed trajectory

and integrating from $t = 0$ to $t = \tau$. $\langle \Delta \vec{v}(\tau) \rangle$ and $\langle \Delta \vec{v}(\tau) \Delta \vec{v}(\tau') \rangle$ are then calculated from the lowest surviving ensemble averaged order in the expansion. Using an argument due to Hubbard,[18] who concluded that $|\vec{E}_{ind}|^2 \ll |\langle \vec{E}_f \vec{E}_f \rangle|$, I-R neglect $|\vec{E}_{ind}|^2$ in the diffusion tensor $\vec{\vec{D}}(\vec{v})$. $\vec{E}_{ind}$ is retained in the friction coefficient, $\vec{F}(\vec{v})$. Since $\langle E_f \rangle = 0$, the lowest surviving term of the ensemble averaged $\vec{E}_f$ expansion is $\langle \vec{E}_f \vec{E}_f \rangle$. The time integral of $\langle \vec{E}_f \vec{E}_f \rangle$ is then seen as the autocorrelation function of $\vec{E}_f$.

The quantities $\langle \vec{E}_f \vec{E}_f \rangle$ and $\vec{E}_{ind}$ are calculated assuming: 1) the fluctuations are longitudinal, which simplifies the form of $\langle \vec{E}_f \vec{E}_f \rangle$ to the product of a unit diagonal tensor times a function; and 2) that the dielectric medium can be calculated in the electrostatic approximation, in which a scalar dielectric response function describes the linearized longitudinal response of the magnetized plasma to a test charge. The simplified Fokker-Planck coefficients then take the form

$$\vec{\vec{D}}(\vec{v}) = \begin{pmatrix} D_\perp(v_\parallel, v_\perp) & & 0 \\ & D_\perp(v_\parallel, v_\perp) & \\ 0 & & D_\parallel(v_\parallel, v_\perp) \end{pmatrix} \qquad (2.C.2)$$

$$\vec{F}(\vec{v}) = \frac{1}{2} \nabla_{\vec{v}} \cdot \vec{\vec{D}}(\vec{v}) + \frac{q}{m} \vec{E}_{ind}(\vec{v}) \qquad (2.C.3)$$

where the magnetic field defines the parallel direction. The terms $D_\perp$, $D_\parallel$ and $\vec{E}_{ind}$ are calculated from the plasma distribution function, $f(\vec{v})$, from which $\langle \vec{E}_f \vec{E}_f \rangle$ and $\vec{E}_{ind}$ are calculated. Since the Fokker-Planck coefficients are calculated from the linearized

14

dielectric response of the plasma, Debye shielding is retained in the coefficients; an impact parameter cutoff at λ_D appears naturally. However, an imposed cutoff at small impact parameter must be adopted to avoid a logarithmic divergence in the coefficients. This divergence can be traced to the calculation of the dielectric response function. This calculation is made in the plasma fluid limit (essentially an expansion in powers of Λ^{-1}), and doesn't correctly describe the plasma response when the test particle closely encounters a plasma particle. The small impact parameter cutoff is chosen to be the classical distance of closest approach, $b_o \equiv q_1 q_2 / T$. This value of b produces a large angle collision, and can be viewed as the point where a Fokker-Planck formulation breaks down.

Energy relaxation rates are calculated from the expression for the rate of change of an ensemble of test particles with the same velocity:

$$\left\langle \frac{d}{dt} \left(\frac{1}{2} m v^2 \right) \right\rangle = \frac{\left\langle \frac{1}{2} m \Delta (v^2) \right\rangle}{\tau} = \frac{m}{2\tau} \left\langle \left| \vec{v} + \Delta \vec{v} \right|^2 - \left| \vec{v} \right|^2 \right\rangle \quad (2.C.4)$$

which is then multiplied by the test particle velocity distribution and integrated over all velocities. Equation (2.C.4) can be put in terms of the Fokker-Planck coefficients:

$$\frac{d}{dt} \left(\frac{1}{2} m v^2 \right) = m \vec{v} \cdot \vec{F}(\vec{v}) + \frac{m}{2} \, \text{Tr} \, \vec{D}(\vec{v}) \quad (2.C.5)$$

where "Tr" is the trace operation.

D. Anisotropic Temperature Relaxation Rate

This procedure of I-R for calculating energy relaxation rates is applied to the calculation of the rates at which the parallel and perpendicular energy (referred to the magnetic axis) changes:

$$\frac{d}{dt}\left(\frac{1}{2}m\dot{v}_\parallel^2\right) = m\vec{v}_\parallel \cdot \frac{\langle \Delta\vec{v}_\parallel\rangle}{\tau} + \frac{m}{2\tau}\langle \Delta\vec{v}_\parallel \Delta\vec{v}_\parallel\rangle \qquad (2.D.1)$$

$$\frac{d}{dt}\left(\frac{1}{2}mv_\perp^2\right) = m\vec{v}_\perp \cdot \frac{\langle \Delta\vec{v}_\perp\rangle}{\tau} + \frac{m}{2\tau}\langle \Delta\vec{v}_\perp \Delta\vec{v}_\perp\rangle \qquad (2.D.2)$$

which in terms of the Fokker-Planck coefficients are

$$\frac{d}{dt}\left(\frac{1}{2}mv_\parallel^2\right) = m\vec{v}_\parallel \cdot \vec{F}(v_\perp, v_\parallel) + \frac{m}{2}D_\parallel(v_\perp, v_\parallel) \qquad (2.D.3)$$

$$\frac{d}{dt}\left(\frac{1}{2}mv_\perp^2\right) = m\vec{v}_\perp \cdot \vec{F}(v_\perp, v_\parallel) + m D_\perp(v_\perp, v_\parallel) \qquad (2.D.4)$$

Equations (2.D.3) and (2.D.4) are then multiplied by a bi-Maxwellian velocity distribution

$$f(v_\perp, v_\parallel) = \left(\frac{m}{2\pi T_\perp}\right)\left(\frac{m}{2\pi T_\parallel}\right)^{1/2}\exp\left[-\frac{mv_\perp^2}{2T_\perp} - \frac{mv_\parallel^2}{2T_\parallel}\right] \qquad (2.D.5)$$

and integrated over $v_\perp$ and $v_\parallel$. The friction and diffusion coefficients are also determined from the bi-Maxwellian distribution. The values of $T_\perp$ and $T_\parallel$ need not be close to each other, since this method is not dependent upon an expansion about equilibrium.

The velocity integrations can, in principle, be carried out for any value of magnetic field. However, in order to actually integrate the resultant product of (2.D.3) or (2.D.4) with (2.D.5), the limit of

small magnetic field is taken by I-R. This approximation (essentially one of performing the calculation in the weak field regime $r_g \gg \lambda_D$), along with the assumption of Maxwellian $v_\perp$ and $v_\parallel$ distributions, leads to a series of terms involving the impact parameter. Only one of these terms, $\ln(\lambda_D/b_{min})$, diverges as $b_{min} \rightarrow 0$. The other terms are hence neglected in its favor by I-R. This is the well-known "dominant term" approximation of Chandrasekhar.[30] Adoption of this approximation renders the calculation of the rate uncertain at the $1/\ln \Lambda$ level (about 10%). A further simplification is made by assuming only a single species plasma neutralized by a static dielectric background. (The equivalent background is provided by the magnetic field in a pure electron plasma.)

With these approximations, the coupled collisional anisotropic temperature relaxation rate equations are given by I-R as

$$\frac{d}{dt} T_\perp = -\frac{1}{2} \frac{d}{dt} T_\parallel = \frac{8}{15} \left(\frac{\pi}{m}\right)^{1/2} \frac{nq^4 \ln \Lambda}{T_{eff}^{3/2}} (T_\parallel - T_\perp) \qquad (2.D.6)$$

Here Λ is given as λ_D/b_o, where $b_o = q^2/T$ is the average classical distance of closest approach; Λ is thus seen as the plasma parameter $n\lambda_D^3$. The effective temperature, T_{eff}, is given by I-R as

$$T_{eff}^{-3/2} = \frac{15}{4} \int_{-1}^{1} \frac{dx \; x^2(1-x^2)}{[(1-x^2)T_\perp + x^2 T_\parallel]^{3/2}} \qquad . \qquad (2.D.7)$$

17

This integral can be solved by parameterizing the anisotropy as $A \equiv T_\perp / T_\parallel - 1$; then

$$T_{\text{eff}}^{-3/2} = \frac{15}{4} T_\parallel^{-3/2} A^{-2} \left[-3 + (A+3) \begin{Bmatrix} \tan^{-1}\sqrt{A}/\sqrt{A} \;\; ; \;\; A > 0 \\ \\ \tanh^{-1}\sqrt{-A}/\sqrt{-A}; \; A < 0 \end{Bmatrix} \right]$$

(2.D.8)

Equations (2.D.6) and (2.D.8) are seen to give the same anisotropic temperature relaxation rate as is given by Book[31]; there is no reference given by Book for this rate.

The I-R rate equations (2.D.6) can be decoupled if there are no external sources or sinks of thermal energy. $T_\parallel$ and $T_\perp$ are then related through $\frac{1}{3} T_\parallel + \frac{2}{3} T_\perp = T_f = $ constant. Then the two rate equations become identical, with $T_\parallel$ and $T_\perp$ interchangeable, as

$$\frac{d}{dt}(T_\perp - T_f) = -\nu_\perp (T_\perp - T_f)$$

(2.D.9)

where the rate, $\nu_\perp$, can be written as

$$\nu_\perp = \frac{8}{5} \left(\frac{\pi}{m}\right)^{1/2} \frac{nq^4 \ln \Lambda}{T_f^{3/2}} H(A) \; .$$

(2.D.10)

The function $H(A)$ is then found from (2.D.8) and the definition of A to be

$$H(A) = \frac{15}{4} \frac{\left(\frac{2}{3} A + 1\right)^{3/2}}{A^2} \left[-3 + (A+3) \begin{Bmatrix} \tan^{-1}\sqrt{A}/\sqrt{A} \;\; ; \;\; A > 0 \\ \\ \tanh^{-1}\sqrt{-A}/\sqrt{-A}; \; A < 0 \end{Bmatrix} \right]$$

(2.D.11)

$H(A) \to 1$ as $\pm A \to 0$. The evolution in the limit of vanishing anisotropy is seen to be exponential with a rate

$$\nu_{\perp_o} = \frac{8}{5}\left(\frac{\pi}{m}\right)^{1/2} \cdot \frac{nq^4 \ln \Lambda}{T_f^{3/2}} \qquad (2.D.12)$$

For comparison purposes, the rate at which an isotropic Maxwellian distribution (at temperature T_t) of test particles comes into equilibrium with an unmagnetized isotropic Maxwellian plasma at temperature T is given by Spitzer,[32, 33] as well as I-R,[6] as

$$\nu_o = \frac{4}{3}\left(\frac{\pi}{m}\right)^{1/2} \frac{nq^4 \ln \Lambda}{T_f^{3/2}} = \frac{5}{6}\nu_{\perp_o} \qquad (2.D.13)$$

in the limit $T_t \to T_f$. The two rates ν_o and $\nu_{\perp_o}$ are not identical in the limit of vanishing anisotropy because the functional forms of $\vec{F}(\vec{v})$ and $\vec{\vec{D}}(\vec{v})$ are different, even in the limit.

The rate given by (2.D.10) as it stands is unsuitable to describe the relaxation process in a strongly magnetized plasma, defined by the parameter regime $\lambda_D \gg r_g$. However, using a general result of M-J-T,[7, 8] equation (2.D.10) can be applied in the strongly magnetized regime to good approximation as long as the Coulomb logarithm, $\ln \Lambda$, is modified by the substitution of $\bar{r}_g$ for λ_D in Λ; i.e. $\ln \Lambda \to \ln(\bar{r}_g/b_o)$. $\bar{r}_g$ is the thermal velocity gyroradius.

This substitution implies that the largest effective impact parameter is $\bar{r}_g$, not the Debye shielding length. Physically, this

result is seen to be in agreement with the concept of adiabatic invariance as applied to the gyromotion of the particle around its guiding center. The gyromotion is viewed as the motion of an oscillator of energy $E = \frac{1}{2} m v_\perp^2$ and frequency $\omega = qB/mc$. According to adiabatic theory,[34] such an oscillator has an adiabatic invariant, $I \equiv E/\omega$, which remains constant so long as the parameters (which includes field quantities) of the oscillator are changed slowly compared to ω. In a constant magnetic field B, the invariant I (with all constants suppressed, I is usually referred to as $\mu \equiv v_\perp^2/B$, the particle gyromoment) will result in a constant perpendicular energy even in the presence of slowly varying electric fields.

A Coulomb collision involves the action of just such varying electric fields upon a particle. The electric field of each particle in a magnetized plasma can be thought of as the sum of three parts; an average monopole term, which falls off as r^2, a dipole term due to the gyromotion, which falls off as r^3, and higher order poles. Consider a test particle interacting with the first two field terms of another particle, i.e. a "collision." If the particles pass each other at a distance much larger than r_g, but smaller than λ_D, then the monopole field at the test particle position will vary only slowly during the passage, and the dipole term will have been greatly reduced by its r^{-3} dependence. The perpendicular energy of the test particle will thus hardly be affected, and although the particles may exchange

parallel energy, such two-particle exchanges do not contribute to isotropization. Only when the particles pass by each other on the scale of r_g does the monopole field vary rapidly enough to break the adiabatic invariant of the test particle and affect its perpendicular energy. This exchange of perpendicular and parallel energy does tend to isotropize both the perpendicular and parallel degrees of freedom.

The component of the friction coefficient in the parallel direction that is due to the collective response of the fluid (E_{ind}), however, may well continue to have an interaction range of λ_D, since it is essentially due only to the monopole terms of the interaction. Nevertheless, approximating an effective impact parameter cutoff at $\bar{r}_g$ seems physically reasonable, and recent numerical studies of this anisotropy by Hjorth[35] indicate that in the regime $b_o \ll r_g \ll \lambda_D$ the M-J-T approximation is correct.

The theoretical predictions of I-R and M-J-T are not without some controversy. Kaiser[36] has disputed the I-R method of calculating energy loss rates in magnetized plasmas, due to oversimplifications in the evaluation of $\vec{D}(\vec{v})$ and in the expansion of $\vec{E}$ along the unperturbed orbits. He concludes, however, that the final expression is valid, basically because the magnetic field does no work on the particles. Matsuda[37] has questioned the validity of the M-J-T approximation, and suggests that, in the strongly magnetized regime (such as that of our plasma), corrections to the Coulomb logarithm

may be as large as $\ln \Lambda$ for certain velocity classes. No Maxwellian averaged correction was quoted, and from the few numerical predictions, it is not clear what form such a correction would take.

The magnetized pure electron plasma used in this study of the anisotropic temperature relaxation rate is in the magnetized regime $\overline{r}_g \ll \lambda_D$. The appropriate theoretical rate calculation is then given by the I-R calculation (2.D.9) with the argument of the Coulomb logarithm suitably modified to $\ln \Lambda_e = \ln \overline{r}_g/b_o$ as per the M-J-T approximation.

III. The Experimental Device

A. The Equilibrium Plasma

The experimental device used for this study is the third generation of a family of devices pioneered by Malmberg and deGrassie.[38] These devices produce and confine a nonneutral plasma consisting of only electrons within a series of conducting coaxial cylinders. The basic geometry of these devices is cylindrically symmetric. The radial confinement of the plasma is provided by a uniform axial magnetic field produced by a concentric external solenoid. The axial confinement is provided by applying sufficiently strong potentials to conducting cylinders whose axial separation fix the plasma length. This creates potential energy barriers that are sufficiently large enough to reflect any electron back into the confinement region.

Malmberg and O'Neil,[39] and O'Neil,[40, 41] have shown that in the absence of external torques applied to the plasma (such as those caused by collisions with neutrals or interactions with fields which break cylindrical symmetry), these nonneutral plasmas can, in principle, be confined indefinitely.

The key to indefinite confinement of a pure electron plasma is the conservation of total canonical angular momentum of the electrons,

$$P_\theta = \sum_j \left(mv_{\theta_j} - \left(\frac{e}{c}\right) A_\theta(r_j) \right) r_j \ , \qquad (3.A.1)$$

where r_j , v_{θ_j} are the jth electrons radial coordinate and azimuthal velocity, respectively, and $A_\theta(r) = B_z r/2$ is the vector potential of the uniform axial magnetic field. The electron charge and mass is -e and m , respectively, and c is the speed of light in a vacuum. For B_z sufficiently large, the diamagnetic field can be neglected in A_θ , and the electron angular momentum, $mr_j v_{\theta_j}$, can also be neglected in the sum. Thus $P_\theta \simeq -(m\Omega/2) \sum_j r_j^2$, where $\Omega = eB_z/mc$ is the electron gyrofrequency. Conservation of P_θ implies conservation of the mean square radius of the plasma, and hence in the absence of torques the plasma can be radially confined indefinitely. The presence of image charges on the confining cylinders doesn't materially change this result.[41]

It is easy to show that the mrv_θ component of the P_θ sum may be neglected with respect to the field component. Let $v_\theta \hat{\theta}$ ($\hat{\theta}$ is the azimuthal direction in cylindrical coordinates) be composed of two parts. One part is the gyrocenter drift velocity $\vec{v}_d$, which is given by $\vec{v}_{dn} = c\vec{E}(r_c) \times \vec{B}_z/B_z^2 \simeq \omega_d(r_c) r_c \hat{\theta}$. It is caused by the column's radial electric field $E(r_c)\hat{r}$ at the electron gyrocenter, r_c. The other part is the $\hat{\theta}$ component of the electron gyrovelocity, $\vec{v}_g$, about the gyrocenter, $\vec{v}_g = \vec{r}_g \times \vec{\Omega}$, where $\vec{r}_g$ is the gyroradius. After some manipulation, (3.A.1) can be rewritten as

$$P_\theta = \frac{m}{2} \sum_j \left(\Omega - 2\omega_d(r_{cj}) \right) \left(r_{gj}^2 - r_{cj}^2 \right) . \qquad (3.A.2)$$

For our plasmas, $\omega_d(r_j) \sim \omega_p^2/\Omega \ll \Omega$, where ω_p is the plasma frequency, and the mean squared gyroradius is much smaller than the mean squared radius of the plasma, and hence $P_\theta \simeq -\frac{m\Omega}{2} \sum_j r_{cj}^2$.

If the plasma can be confined long enough, the interactions among the electrons will eventually drive the system to a global thermal equilibrium. The distribution of such an equilibrium state is given by[42, 43]

$$f(\vec{v}, \vec{r}) = Z^{-1} \exp\left[-(H - \omega P_\theta)/T\right] \tag{3.A.3}$$

where H is the Hamiltonian for the electrons in a magnetic field, and Z is the partition sum. Such a distribution is stable against all fluctuations and hence is quiescent. These distributions describe a rigid body rotating with angular frequency ω (i.e., no shear in azimuthal velocity) about the axis of symmetry, a global Maxwellian velocity distribution (of temperature T) in a frame rotating with the body, and a density distribution which is a monotonically decreasing function of radius. This density function is characterized by a central density n_o extending out to some radius, after which the density rapidly decreases to zero over the scale of a few Debye lengths. The values of ω, T and n_o are set by the initial conditions of the plasma: N electrons, total energy E, and total canonical angular momentum P_θ.

Prasad and O'Neil[44] have shown that when a local coordinate which is perpendicular to the surface is employed, the equilibrium

plasma density monotonically decreases to zero on the scale of a few Debye lengths over the entire plasma surface. Thus, while the detailed shape of the end of the plasma can be quite complicated, in general the z-dependence of the density distribution for long plasmas is straightforward; $n(r, z)$ is essentially constant along z until near the end of the plasma, where the density decreases to zero over the scale of a few Debye lengths.

These thermal equilibrium distributions can be completely realized in an ideal device: one that is characterized by a perfect vacuum (no neutrals or contaminating ions) and perfectly θ symmetric fields. Such a device cannot be constructed. However, if the torque input to the plasma can be kept small enough so that the rate at which the mean plasma radius changes (external transport processes) is much smaller than the rate at which the plasma moves towards thermal equilibrium (internal transport), then states closely approaching thermal equilibrium can be observed.

A plasma in such an equilibrium state is very interesting experimentally. Internal transport processes become more amenable to experiment as the external transport processes decrease in magnitude. The pursuit of the equilibrium state has, in part, driven the evolution of the pure electron containment devices. Better vacuum systems and construction techniques allowed more precise control of neutrals. More attention to maintaining the cylindrical symmetry of

the group of confining cylinders reduced electrostatic field asymmetries. Using nonmagnetic materials where possible, and requiring symmetric geometries where magnetic materials (such as stainless steel) must be used, reduced magnetic field asymmetries. Taking great care with the design and construction of both the main solenoid and the axial alignment "trimming" coils also reduced magnetic field asymmetries.

The third generation device was designed and constructed so as to reduce external transport enough to allow observation of the thermal equilibrium state. It was therefore given the appellation "EV" - Equilibrium Voltage confinement - following the nomenclature of its predecessors. EV's diagnostic capabilities include the ability to scan both the density and the plasma kinetic energy component perpendicular to the field as a function of radius. Transport can then be measured by obtaining the density and energy profiles as functions of time. Driscoll et al.[45] have done this for spatial transport of electrons and thermal energy. They have shown a confined electron plasma approaching the global thermal equilibrium state in EV.

Such an equilibrium plasma is an ideal subject for the production of velocity space anisotropies characterized by two different Maxwellian temperatures, $T_\perp \neq T_\parallel$ (the magnetic field provides the reference axis), and the measurement of the subsequent collisional

27

relaxation. The characteristic relaxation rate can be much larger than the rate of external transport, depending upon B_z, and thus the relaxation can be measured under conditions of temporally constant total thermal energy and density. Furthermore, by measuring the rates in a radially localized region about the axis, the radial gradients of density and temperature are also essentially zero.

B. The Experimental Apparatus - EV

The confinement and analysis regions of the EV apparatus, which has been previously described,[46] are schematically shown in Figure 1. The confinement region consists of eight electrically isolated coaxial cylinders of inner radius $R_w = 3.81$ cm; all have a length of 7.62 cm except for L2, which is 3.81 cm long. One cylinder has four electrically isolated wall sections evenly spaced around the cylinder; these sections can be used to launch and/or detect plasma waves but for these experiments are interconnected to emulate a uniform cylinder. There is also a spirally wound tungsten filament, which when heated by a D. C. electric current provides a source of electrons. An accelerating grid is placed just in front of the filament. Another grid is placed just behind the filament and is electrically connected to the filament center.

The analysis region includes an electrically isolated circular collimator plate whose axis is offset from and parallel to the confinement region's symmetry axis. The collimator plate is free to rotate
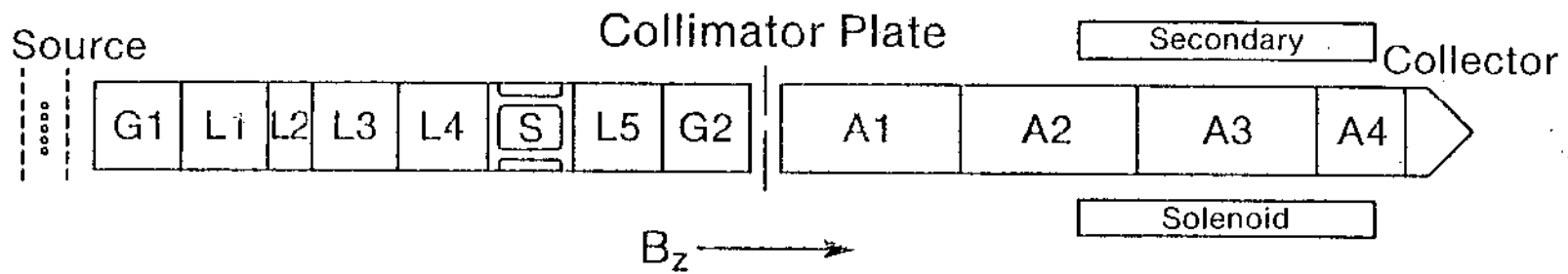
Figure 1. The EV apparatus. The confinement region extends from the source to cylinder G2. The analysis region extends from the collimator plate to the collector.

about its axis. This plate has three small holes of various diameters (1/8", 3/16", 1/4") spaced 120° apart on a radius of 1.9", which is equal to the axial offset. In principle, any hole can be rotated to coincide with the device's symmetry axis, or to any desired radius from that axis. In practice, a stepping motor (400 steps = 2π) can move the desired hole to one of the many possible incremented radial locations, with an estimated uncertainty of about one half step. Behind the plate, coaxial with the confinement region's symmetry axis, are four electrically isolated cylinders with $R_\omega = 3.81$ cm; all have lengths of 12.70 cm except for A_4, which is 7.62 cm long. Behind these is an electrically isolated charge collection electrode. All confinement and analysis cylinders, as well as the charge collection electrode and the collimator plate, are made from OFHC copper. All cylinders, the collimator plate, and the collection electrode are gold-plated after machining to control oxidation. Concentric with and centered lengthwise upon cylinder A_3 is a small solenoid of length 20.45 cm. This solenoid is water cooled, and is placed in a stainless steel jacket. It provides a secondary magnetic field used for energy analysis.

The confinement and analysis regions are supported within a concentric cylindrical vacuum vessel constructed of low permeability stainless steel. The system is initially roughed out by LN_2 cooled absorption pumps. A 500 ℓ/s ion pump, a LN_2 cold trap, and a Ti

30

sublimation pump maintain an operating pressure of 10^{-11}-10^{-10} torr after the complete system is baked to 200°C. Surrounding the vacuum vessel is the water-cooled main solenoid, which is precision wound on aluminum coil form. This solenoid is capable of producing uniform axial magnetic fields from 0 to 470 Gauss. The solenoid has a 40.3 cm diameter and is 217.3 cm long. In addition, there are two sets of rectangular trimming coils outside of the main solenoid. They produce magnetic fields, B_x and B_y, which are perpendicular to the main field and each other. They were originally intended to provide a precision method of aligning the resultant B field direction with the confinement region symmetry axis, but, as will be noted in Appendix B, they also can be employed to provide a very effective means of reducing the level of density fluctuations in the confined plasma. Fluctuation reduction can lead to enhanced statistical accuracy of density and temperature measurements.

A microcomputer was used to monitor, direct, and analyze the experiment, although a purely manual mode of operation was often used when new experimental configurations were tried, since it was usually easier to turn a knob than modify a program. Utilizing the computer during a data set run was a necessity, since each temperature or density measurement required computer analysis of a large amount of data generated by hundreds of individual shots. Each shot requires the generation of a nearly identical plasma upon which the

same experiment is conducted. At an appropriate point during the experiment, a destructive measurement is made.

C. Operation of EV

The anisotropic temperature relaxation rate measurement requires the creation of a known anisotropy and measurement of the subsequent temporal evolution of that anisotropy. The anisotropy is measured by measuring the perpendicular temperature of the plasma and the average plasma density (averaged along the magnetic field line) to an accuracy of about 5% at any radius. The parallel temperature can easily be measured only on the plasma axis, and only for the energetic tail of the parallel velocity distribution. The accuracy of this measurement is on the order of 10%. Each of these measurements require many individual destructive shots, each of which involves a dump of the plasma to measure the charge (sometimes as a function of energy) along field lines at a chosen plasma radius.

This means that the operation of EV is geared toward cyclic operation; each cycle must produce an identical plasma, create the identical anisotropy, and make a measurement at the same time of evolution. Each cycle consists of four phases: (1) an inject phase, where the plasma column is formed and captured; (2) a "sample preparation" phase, where the plasma is manipulated to the desired density and temperature in a near equilibrium state; (3) an experiment phase where the desired thermal anisotropy is created and then

allowed to relax for a fixed amount of time; (4) a "dump and measure" phase, where a charge measurement is made as the plasma is destroyed, which leaves the device ready for the next cycle.

When enough individual measurements have been made to enable a density or temperature measurement of sufficient accuracy, the fixed time of evolution in the experiment phase can be changed and the process begun again. The amount of data (number of shots) required by each measurement varies; up to hundreds of individual identical shots may be required to measure a density or temperature with sufficient precision. Thousands of shots are required to monitor enough of the temporal evolution of a given anisotropy to calculate its relaxation rate.

All of these shots must be performed with nearly identical plasmas. Since they cannot be exactly identical, the fluctuations in the amount of charge, and the energy distribution of the particles along field lines at any given plasma radius will, to an extent, determine how many shots will be required for a given accuracy level. Since each shot takes from 1-2 seconds, and hence the measurement of a rate can take hours, a technique which lowers the level of fluctuations was investigated and then put into service for some of the rates measured in the latter stages of this study. Appendix B describes this technique. It permits measurements of greater accuracy for a given time spent.

C. 1. The Inject Phase

The inject phase starts with all confinement cylinders held at ground potential except for the two cylinders chosen as the confinement barriers (G1 and L5, say), which have large negative potentials applied to them. The inject gate (G1 in this case) potential is rapidly switched to ground and held there. Electrons thermionically emitted from a negatively biased tungsten filament then form a column that extends from the source through the grounded cylinders to the potential barrier formed by the large negative potential applied to the dump gate (L5).

The dynamics of the column formation are not well understood, and such understanding seems a formidable problem, but the equilibrium characteristics of the column have been addressed by a simple model of Malmberg and deGrassie.[38] The essence of the model is twofold: electrons do not significantly move across field lines, and the potential within the column (due to space charge) far from the source matches that of the source to lowest order. The column is assumed long enough so that the potential is independent of z. The EV device employs a tungsten wire filament with a planar Archimedes spiral geometry perpendicular to and centered on the confinement axis. The filament is resistively heated by passing a D.C. current through the wire. This source geometry produces, to lowest order, a parabolic radial potential across the filament. This potential is

then matched by the potential of a column whose charge density is radially uniform out to at most the maximum radius of the filament. The radius of the plasma is determined by the requirement that the potential at the column axis match that of the filament center, which can be adjusted with an independent bias supply. The magnitude of the charge density is set by the ratio of the potential drop across the filament to the square of the filament radius. The narrow range of applied D.C. filament current which yields sufficient thermionic emission yet doesn't cause structural weakness results in a charge density of about 10^7 electrons/cm^3. In principle, this density can be raised by applying a short duration voltage pulse to the filament, in addition to the D.C. heating current. This increases the potential drop across the filament for the duration of the pulse. Capture could then be effected once the column is established at the enhanced density determined by the voltage pulse. The pulse duration must be kept short in order to limit the heat load on the filament. This technique has not as yet been implemented on EV.

Once the column is established, the inject gate potential is ramped from ground to the final confinement potential, V_c. This pinches off the column from the source and traps it between the inject and dump gates. Figure 2a shows a captured plasma schematically. The time required to establish the column is on the order of a few electron transit times - approximately 10 μsec. The inject gate

potential is usually ramped to V_c on a time scale that avoids the occurrence of the diocotron wave of lowest azimuthal mode number, $\ell = 1$.[47-49] The ramp time scale must be much longer than the diocotron period. With an appropriate choice of inject and dump gates, and by varying the magnitude of V_c, confined plasma lengths over the range $4 \leq L_p \leq 40$ cm can be attained. The plasma radius is about that of the filament ($R_p \simeq 2$ cm) and the plasma density is about 10^7 cm^{-3}.

C.2. The Sample Preparation Phase

The captured plasma can be axially expanded or compressed if densities other than 10^7 cm^{-3} are desired. Assume the initially confined plasma is trapped between G1 and G2, i.e. is contained in L1 through L5. If the potential on L1-L4 is then ramped to V_c, the electrons of the plasma, which are continually bouncing along field lines between G1 and G2, will eventually be unable to penetrate the rising potential barrier within L1-L4. Figure 2b schematically shows an axially compressed plasma. The plasma is then axially confined in L5 and S only, which means the density will approximately triple. If we reverse the process, then the plasma will eventually reenter L1-L4. This axial expansion will then lower the density by approximately a factor of 3. We attain our measured density range of 3×10^6 cm$^{-3} < n < 3.5 \times 10^7$ cm^{-3} from compressing or expanding the initially captured plasma. In both compression

36
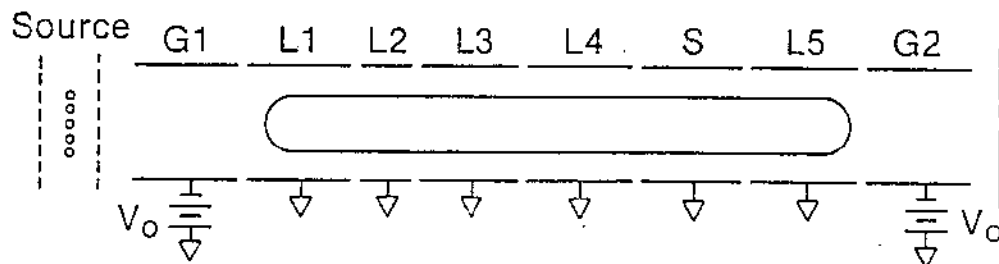
(a) Captured Plasma

(b) Compression
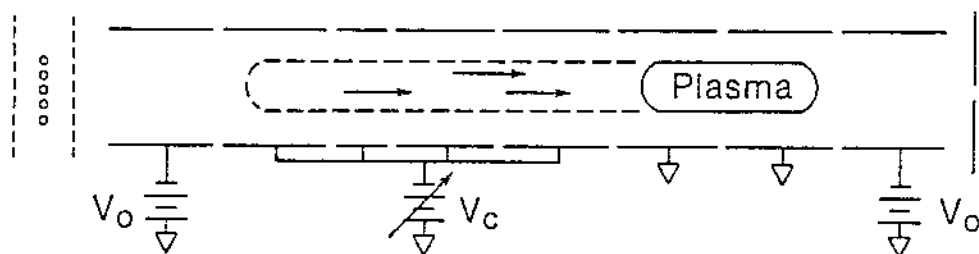
Figure 2. (a) The captured plasma is axially confined between the inject and dump gates by applied potentials. (b) An axial compression is accomplished by slowly ramping the potential V_c applied to the compress gates (L1-L4) until all electrons are excluded from the compress volume.

and expansion cases, there will be a polarization drift in the radial direction due to the net change in the column's radial space charge electric field as the density increases or decreases. This effect is discussed in Appendix F, and is shown to be negligible for the range of compressions used in this study. Hence, these compressions are essentially axial, as is shown in Figure 3.

Figure 3 shows three plots of measured projection density, $Q(r)$, where $Q(r)$ is the total charge along field lines that pass through the collimator hole (see section 3.C.4.iii), taken (a) just before an expansion; (b) 0.3 msec after an expansion, and (c) 50 msec after the expansion, when the initial anisotropy has relaxed to equilibrium. Also shown are measurements of $T_\perp)r)$ at various radii (isolated crosses). $T_\perp$ is measured in eV with the full vertical scale equal to 5 eV. The vertical extent of the cross is an estimated RMS error bar. $Q(r)$ is measured in volts with the full vertical scale equal to 10 volts. The solid curve is drawn between average values of $Q(r)$ at given values of r; the individual measurements of $Q(r)$ are given by the short horizontal lines. The horizontal axis is the radius in units of 0.5 cm; $r = 0$ is the vertical solid line at the center of the graph. The dashed vertical lines represent the confinement cylinder wall radius. The data is taken as a function of collimator hole position, which is varied along an arc which passes through the confinement axis. The data is not exactly symmetric about the $r = 0$
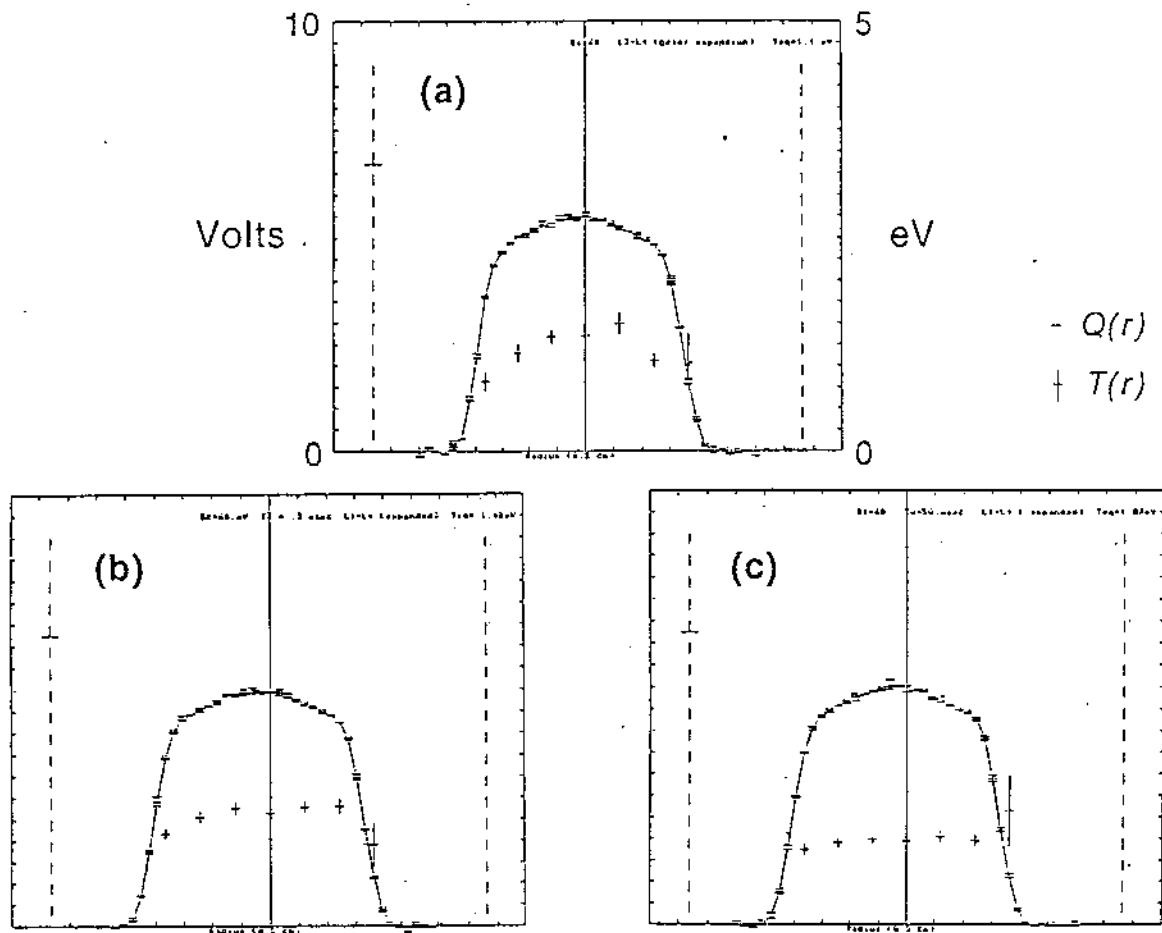
Figure 3. Three plots of Q(r), the number of electrons along field lines (measured in volts), and $T_\perp(r)$, the perpendicular temperature, taken at various radii: (a) just before an expansion; (b) 0.3 msec after the expansion, and (c) 50 msec after the expansion, when the anisotropy has relaxed to equilibrium. The solid line connects averaged values of Q(r). The vertical extent of the $T_\perp(r)$ cross denotes an estimated RMS error bar. Full vertical scale is 10 V for Q(r), and 5 eV for $T_\perp(r)$. The solid vertical line is the approximate position of the r = 0 axis; the two vertical dashed lines represent the cylinder wall radius.

39

line due to both the fluctuating nature of the individual measurements and the uncertainty in hole position relative to the confinement axis. The true symmetry axis may vary from graph to graph; the $r = 0$ line is just a guideline. There are two important points to be drawn from these figures. One is that $Q(r)$ is unchanged by the expansion, which implies no net radial transport of electrons. The other is that $T_\perp(r)$ is essentially independent of r in the vicinity of the symmetry axis during the relaxation of the anisotropy.

The desired temperature is obtained by cyclically compressing and expanding the plasma axially in such a manner as to perform a net amount of work on the plasma each cycle. At the end of each cycle, the density has returned to its initial value, and the temperature has increased due to the net amount of work done on the plasma. This process is described in Appendix A. The essential feature is the utilization of a one dimensional axial compression. Such a compression heats only the parallel degree of freedom. It must be accomplished on a time scale small enough so that there are no collisions which transfer energy into the perpendicular degrees of freedom. The power supply which provides the compressing potential does work on the plasma, and the amount of work it does depends, in part, on $T_\parallel$, the temperature of the parallel motion. This work raises $T_\parallel$, but $T_\perp$, the perpendicular temperature, remains unchanged. By keeping the plasma compressed for a time comparable to a collision

time, the parallel and perpendicular degrees of freedom relax towards a common value. This lowers $T_{\parallel}$ (and raises $T_{\perp}$), and thus when the plasma undergoes a 1-D expansion back to its original volume, the amount of work done by the plasma on the power supply in expansion is less than the amount of work done by the supply on the plasma during compression. There is thus a net amount of work done on the plasma over one cycle.

Neither the density nor temperature can be increased arbitrarily, since raising either increases the total energy of each electron. If the applied potential barriers are insufficient to reflect these electrons, then they are no longer axially confined. The currently available high voltage operational amplifier electronics limit V_c to about -300 V. Figure 4a shows an idealized schematic of the potential energy as a function of z. Also shown is a Maxwellian parallel kinetic energy distribution measured at $z = 0$, the plasma center. Electrons cannot be confined when the sum of their parallel kinetic energy and potential energy exceed the confining barrier height.

If the radial electric and pressure forces on a charged fluid element of the plasma are too great, the axial magnetic field cannot radially confine the element. The maximum charge density (which produces the radial electric field) that can be confined by a given magnetic field is determined by the Brillouin limit.[50,51] This maximum density is decreased by the presence of radial pressure

41
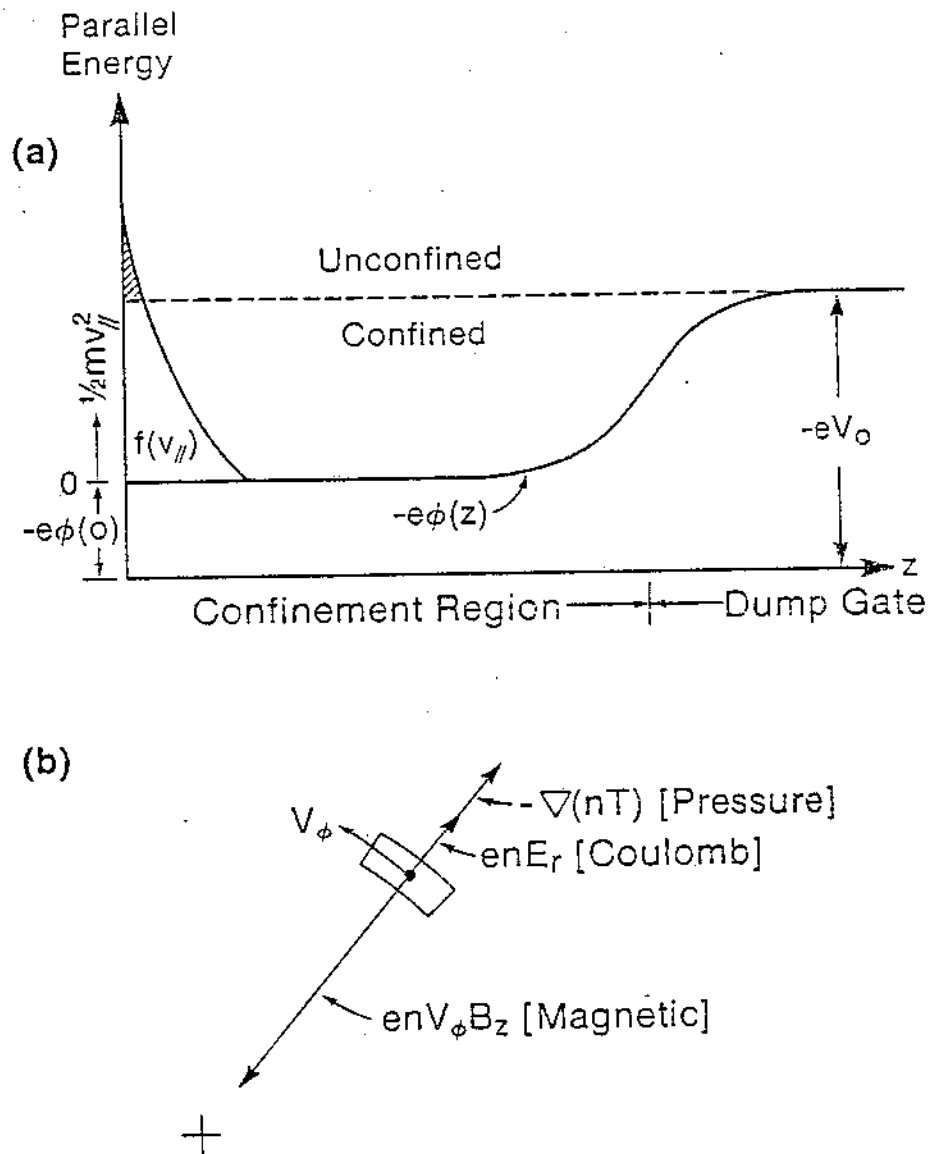
Figure 4.   Axial or radial deconfinement can occur if temperature
or density limits are exceeded. (a) shows axial deconfine-
ment when excessive thermal energy exceeds the height of
the confining potential energy well. z is the axial co-
ordinate and the ordinate is the potential energy as a func-
tion of z. A Maxwellian parallel kinetic energy distribu-
tion is schematically added to the potential at z = 0; the
sum of this potential and the parallel kinetic energy of an
electron is the relevant total energy of the electron. The
electrons in the cross hatched tail region are not confined
by the well. (b) shows a radial force diagram on a charge
fluid element. The azimuthal velocity, v_ϕ , is due to the
sum of the radial electric field and pressure gradient
drift velocities.

(temperature effects). The Brillouin limit can easily be derived from consideration of the radial forces on a charged fluid element, shown in Figure 4b. The electric and pressure forces cause an azimuthal drift of the fluid element. This azimuthal movement of charge in a magnetic field in turn causes a radially inward magnetic force. It is the sum of these radial forces which determine the orbit of the fluid elements about the axis. The Brillouin limit is reached when the net centripedal force required for circular orbits, which increases as the square of the azimuthal velocity, can no longer be provided by the magnetic force, which increases only linearly with the azimuthal velocity. At this limit, the sum of the electric and pressure forces is exactly half of the magnetic force. The angular velocity of the fluid element, ω, is equal to $\Omega/2$ at the Brillouin limit. This limit can be rewritten as $2r_g^2 \leq \lambda_D^2$. Thus the pure electron plasmas produced in these electrostatic/magnetic confinement devices are always in the strongly magnetized regime, $r_g < \lambda_D$, of transport theory.

If the temperature is elevated to a level at which a significant fraction of the electrons are energetic enough to ionize the background neutrals at a sufficiently rapid rate, then the additional physics of ionization can complicate the data analysis of the processes under study. The temperatures used in this study ranged over 0.7 eV $\leq$ T ≤ 8.5 eV. The densities and temperatures studied were not limited by the effects described above, which tends to limit high density and

43

temperature combinations. Rather, low density and high temperature combinations were limited by experimental conditions. The basic scaling of the collisional velocity space equilibration rate is density/ $(\text{temp})^{3/2}$-low densities coupled with high temperatures yield low rates. A desire to keep this rate much larger than other background transport rates limited the combinations of densities and temperatures chosen, as did the available compression/expansion ratios.

Once the desired density and temperature are attained, the plasma is then allowed to evolve to a state of near thermal equilibrium. The time scale of this evolution is on the order of 1 sec at 281 Gauss, the magnetic field strength primarily used in this study. 281 Gauss was chosen so as to minimize the thermal equilibration time - which seems to increase linearly with B_z [49] - and yet maintain an acceptably large characteristic external transport time - which increases as the square of B_z. [46] At the end of this holding period the plasma is ready for the experiment phase to proceed.

At some point during this sample preparation the fluctuation reducing technique described in Appendix B may be employed to improve shot-to-shot reproducibility. This technique is most effective when the plasma is long and B_z is greater than about 150 Gauss.

C. 3.   The Experiment Phase

The experiment phase begins with a 1-D axial compression (or expansion) that creates the initial anisotropy in velocity space. This anisotropy is characterized by two essentially Maxwellian velocity distributions with temperatures $T_{\parallel} \neq T_{\perp}$. The compression typically takes approximately 1 ms to complete. After the compression is finished, the induced anisotropy relaxes for an amount of time determined by a timing circuit which is started at the end of the compression. The timing circuit triggers a plasma dump and measurement at the end of the desired time interval.

The compression (or expansion) which produces the initial anisotropy also changes the density, and it could be asked whether or not this change in parameters, which certainly moves the state of the plasma away from the original thermal equilibrium, would also initiate further transport which might complicate the relaxation process by providing sources or sinks of energy and/or density. However, the fact that the large density and temperature fluctuations have already been smoothed out during the holding stage tends to keep any such transport rates small. See Figure 3, which shows the number of electrons along field lines and temperature data taken just before an expansion, just after, and after the induced anisotropy has relaxed. To within the accuracy of the charge measurements, there has been no net radial particle transport over the time of relaxation.

Also, temperature measurements taken after the anisotropy has relaxed are essentially constant over time scales comparable to the relaxation time. Figure 5 shows a typical anisotropy relaxation data set, which is comprised of temperatures taken just before the velocity space anisotropy is created, during its relaxation, and after it has decayed. Note there is no significant temperature change following the relaxation over several relaxation time periods. These two experimental results allow the deduction that the relaxation occurs in conditions of essentially constant density and thermal energy.

The essence of the measurement of the anisotropic temperature relaxation rate is in following the time evolution of the anisotropy after it has been created. This is done by measuring the anisotropy repeatedly at various times after the anisotropy is induced. These intervals are chosen to adequately cover the relaxation throughout the decay and well into the final equilibrium. The measured time evolution of the anisotropy is then analyzed to yield a relaxation rate.

The dump and measure phase is triggered after the desired time interval of relaxation has been counted out by a digital clock circuit which has a fundamental clock rate of 10 MHz provided by a crystal-controlled oscillator. Interval timing uncertainty is of the order of 1 μsec with this circuit. The interval starts at the end of the compress (or expand) potential ramp. The initial anisotropy is defined to be that which exists at the end of the compress ramp.
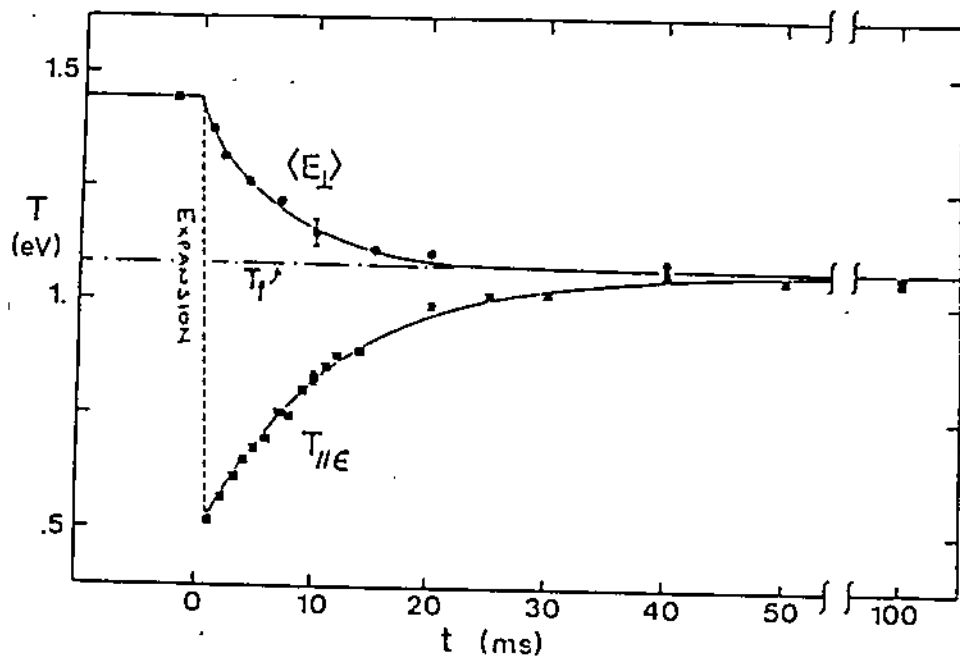
Figure 5. The relaxation of a given anisotropy to equilibrium is shown by a plot of $\langle E_\perp \rangle$ and $T_{\parallel \epsilon}$ measurements made as functions of time. The plasma is in equilibrium for times $t < 0$. Note the $T_{\parallel \epsilon}$ value measured at $t < 0$. The expansion which induces the initial anisotropy starts at $t = 0$ and continues for roughly 1 msec. The solid lines represent the best fit of a simple exponential decay model to the data. The rate best fit to the $\langle E_\perp \rangle$ data is $\nu_\perp = 146 \pm 10$ sec^{-1}; the rate best fit to the $T_{\parallel \epsilon}$ data is $\nu_\perp = 90 \pm 6$ sec^{-1}. $T_f = 1.07$ eV and $\bar{n} = 0.54 \times 10^7$ cm^{-3}. Characteristic error bars are shown at $t = 10$ msec.

C. 4. The Dump and Measure Phase

The dump and measure phase depends upon which type of measurement is to be made - perpendicular temperature, $T_\perp$, parallel temperature, $T_\parallel$, or density, n. In all cases, triggering the dump and measure phase initiates a process which allows the confined plasma to escape past the dump gate by reducing the dump gate potential energy barrier. The escaped electrons then travel axially down the field lines, where they eventually encounter the positively biased collimator plate. Most of the electrons are stopped and collected by the plate, but some will be on field lines that pass through the hole in the plate. These electrons pass through the collimator hole to enter the analysis region. Figure 6 schematically shows the trajectories of the dumped electrons.

Depending upon the particular measurement desired, some or all of these electrons will pass through the analysis region to encounter and be collected by the positively biased collector electrode. The amount of collected charge is calculated from the measured rise in voltage at the input of the first stage amplifier (Figure 7 shows the charge measurement circuit diagram) due to the increase in charge on the total distributed capacitance of the input to the amplifier. This distributed capacitance and the gains of the amplifiers are carefully calibrated to an accuracy of about 3%.

Radially Positionable
Collimator Hole

Secondary

Collector

A1   A2   A3   A4

Solenoid

B_z
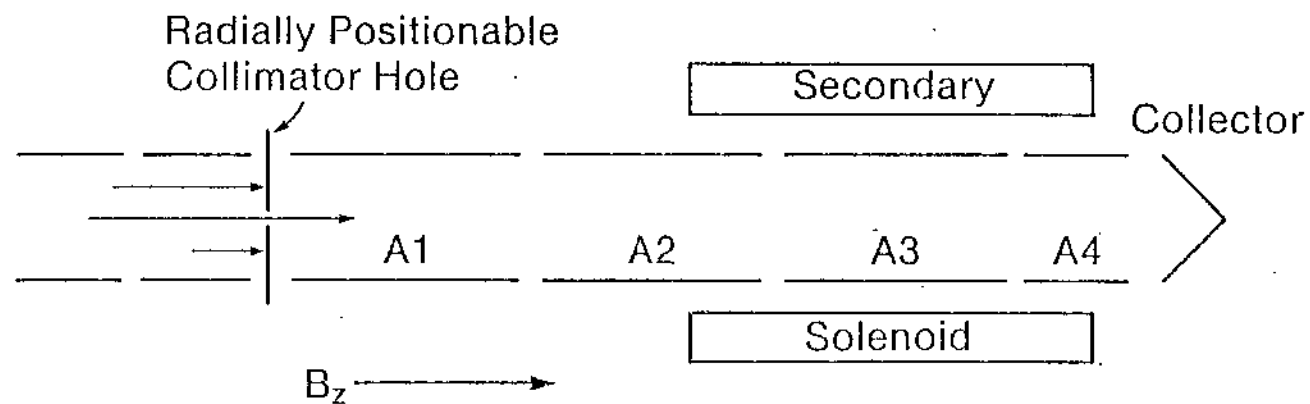
Figure 6. The dumped electrons travel axially down the field lines.
Most electrons encounter the collimator plate, but those
on field lines which pass through the collimator hole enter
the analyzer region.
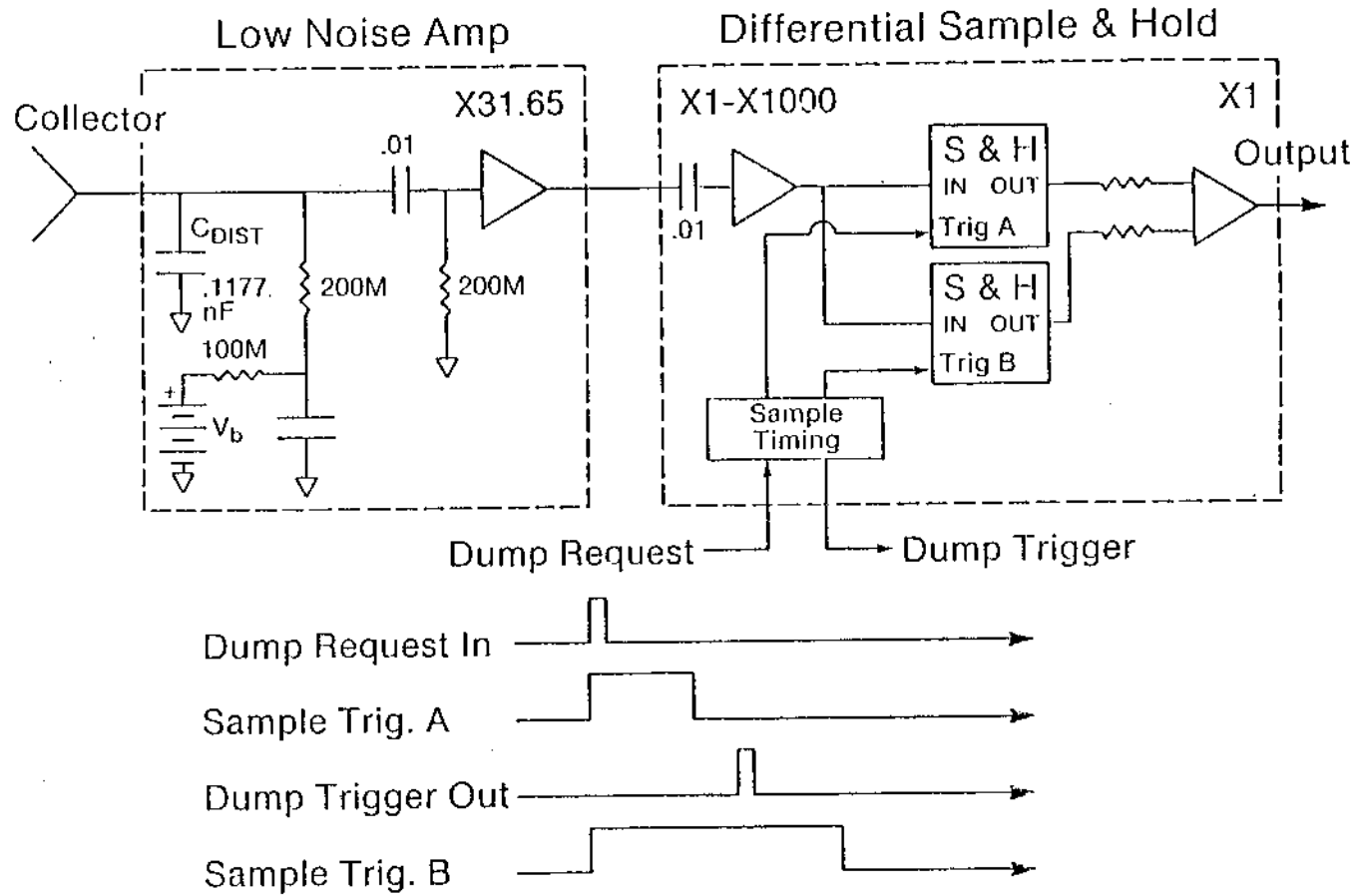
Figure 7. Block schematic of the charge collection and measurement circuit. An initial input "dump request" pulse is generated by the experimental timing circuitry at the desired time. The three output pulses generated by the measurement circuit are timed so that sample and hold "A" holds the signal measured just before the electrons are dumped and sample and hold "B" holds the signal just after. The typical interval between "A" and "B" holds is on the order of 10 μsec. The low noise amplifier section includes a heavily filtered biasing potential, V_b, which enhances charge collection efficiency. The sample and hold circuitry follows the input signal while the trigger pulse is up and holds the signal value at the time the pulse falls.

This charge induced voltage is measured by a differential sample and hold circuit which is triggered by a "predump" pulse after a specified evolution time. The sample and hold circuit then measures the output of the collector amplifier chain both before and after the plasma is dumped, and subtracts them. This differencing scheme is helpful in that it filters out noise whose frequency is much lower than the inverse difference time (about 30 kHz).

(i) Perpendicular Temperature Measurement

The perpendicular temperature measurement measures the average perpendicular kinetic energy, $\langle E_\perp(r) \rangle$, of the plasma at any chosen radius to an accuracy believed better than 5%. The average is over the distribution of perpendicular velocities along the field lines which pass through the collimator hole. We assume there is no z dependence to this distribution. The measurement of $\langle E_\perp \rangle$ is accomplished by first measuring the change in the number of collimated electrons which pass through an electrostatic potential energy barrier as the barrier height is varied about a chosen value. Second, the barrier height is fixed at that value and the change in the number of electrons which pass through both the barrier and an additional secondary magnetic field as that additional field varies about zero is measured. This extra field forms a magnetic mirror (or cusp) field which subtracts (or adds) an amount of parallel kinetic energy from each electron within it. This amount is in proportion to the electron

perpendicular energy as measured before entering the mirror. The ratio of these two measurements yields $\langle E_\perp \rangle$ directly.

The perpendicular temperature measurement requires many individual shots to acquire the data necessary for analysis. These shots are taken with plasmas that are as similar as possible. Each shot provides one charge measurement. The analyzer parameters under which each charge measurement is made, such as analyzer cylinder potential or secondary magnetic field strength, are adjusted between shots.

The basic measurement is initiated when the potential applied to the dump gate is abruptly switched to ground. The now unconfined plasma then axially expands under the combined influence of its un-opposed axial electric space charge field and kinetic energy. Far downstream from the original confinement volume, the unconfined expanded plasma has a greatly reduced space charge potential energy. The lost potential energy has gone into parallel kinetic energy. Con-sequently, the parallel kinetic energy distribution, $f(E_\parallel)$, of the un-confined plasma contains a complicated mix of the original confined parallel kinetic energies and space charge potential energies, which is determined by the dynamics of the disassembly process. Since plasmas in EV usually have space charge potential energies which are much larger than kinetic energy, $f(E_\parallel)$ bears little resemblance to the confined distribution.

The perpendicular kinetic energy distribution, $h(E_\perp)$, of the disassembled plasma remains essentially identical to that of the confined plasma. This is due to a wide separation of characteristic frequencies: the relatively large gyrofrequency, the inverse time period over which the space charge electric fields change during disassembly, and the relatively low frequency of collisions.

The characteristic time scale over which the electric fields change during the dump disassembly is estimated by measuring the time interval over which electrons, which have passed through the collimator, encounter the positively biased collection electrode after a dump. This time is on the order of 1 μsec. Collision frequencies are typically 10-1000 sec^{-1}. The electron gyrofrequency at 281 Gauss, on the other hand, is approximately 5×10^9 rad/sec. This separation of frequencies insures that the electron gyromagnetic moment, here written with all constants suppressed as $\mu = v_\perp^2/B$, remains an adiabatic invariant throughout the disassembly process. Since B_z remains fixed, $v_\perp^2$ is also unchanging, and thus $h(E_\perp)$ remains unchanged by the disassembly process. Also, there is no time for collisions to affect $h(E_\perp)$.

The measurement technique used to probe $h(E_\perp)$ was first employed by deGrassie,[52] and was based on previous work by Hsu and Hirshfield.[53] The following theory discussion is similar to that of deGrassie. Assume the collimated beam of escaped electrons has a

kinetic energy distribution which is separable, i.e., $g(E_\parallel, E_\perp) = f(E_\parallel) h(E_\perp)$. Let cylinders A1, A2 and A4 be grounded, and let cylinder A3 have an applied negative potential V_A. Further assume that the beam has essentially no space charge. Finally, let the secondary magnetic field solenoid induce field strength $B_s(z)$ in the same direction as B_z. We ask what the parallel kinetic energy of an electron must be in order to pass through A3 to reach the collector. We find that it must be greater than $-eV_A$ plus an amount proportional to $E_\perp$.

We calculate the change a dumped electron's parallel kinetic energy suffers in traveling from well outside of the secondary field to the axial position of maximum secondary field (i.e., well within the mirror). The magnetic field varies over this path from $B = B_z$ to $B = B_z + B_s$, where B_s denotes the maximum of $B_s(z)$. We assume that μ remains a good adiabatic invariant over this path. Then, the constancy of $\mu = v_\perp^2/B$ over this path coupled with the conservation of total energy $\left(\frac{1}{2}m(v_\perp^2 + v_\parallel^2) = \text{const.}\right)$ leads to $\Delta E_\parallel = -\gamma_{max} E_\perp$, where $\Delta E_\parallel$ is the amount the electron parallel energy changes over the path, $E_\perp$ is the electron perpendicular energy as measured well outside of the secondary field (which is its value in the confined plasma), and γ is the ratio B_s/B_z.

Since any electron of energies $E_\parallel$, $E_\perp$ well outside the field will have parallel energy $E_\parallel^* = E_\parallel - \gamma E_\perp$ in the center of the field,

we may think of the secondary field as providing an additional, additive "effective" energy barrier to the electron. This effective magnetic barrier height is equal to $\gamma_{max} E_\perp$. It adds to the electrostatic potential barrier provided by V_A. Since the solenoid and A_3 are designed so that the individual barrier maxima are achieved at the same axial position, the maximum barrier height presented to an electron of initial perpendicular energy $E_\perp$ is $-eV_A + \gamma E_\perp$. Thus an electron must have a parallel energy $E_{\parallel} > -eV_A + \gamma E_\perp$ in order to pass through the barrier to reach the charge collector.

In fact, the solenoid $-A_3$ combination is designed so that the maximum total barrier height is given by $-eV_A + \gamma E_\perp$ even for negative values of γ (a cusp field configuration). This requires solenoidal field extension past both ends of the potential barrier. Therefore the design of the solenoid is such as to require it to be longer than and axially centered upon A_3. Were this not the case, then negative values of γ might only cause a local dip in the barrier height, leaving the maximum independent of γ. In the subsequent discussion, it will be assumed that the maximum barrier height is always dependent upon γ. Figure 8 schematically shows the two barrier components presented to an electron of energy $E_\perp$ as functions of z for both positive and negative γ, as well as the total barrier height. The axial extent of both the solenoid and A_3 is long enough so that the barrier heights are to good approximation independent of radius near the axial center.
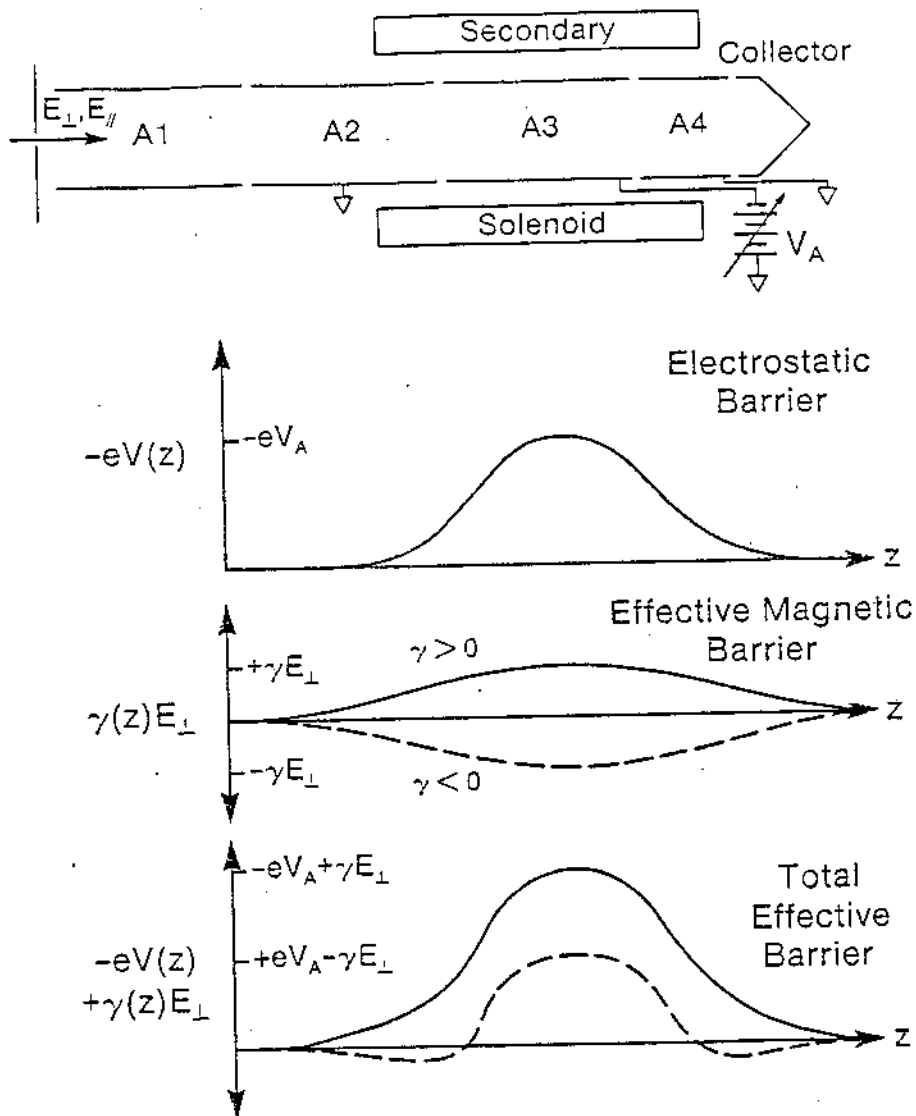
Figure 8. The analyzing section is shown in schematic form, along with graphs of the electrostatic and effective magnetic barriers as functions of axial position z. The dashed lines represent barriers generated by values of $\gamma < 0$. The solenoid and cylinder A3 are axially positioned so that the maximum effective barrier height is given by the sum of the individual barrier maximums.

Figure 9 graphically shows the region of energy space for which an electron will be transmitted through the analyzer region to the collector. The boundary between transmission and reflection is derived from $E_{\parallel} \geq -eV_A + \gamma E_{\perp}$. Integrating the energy distribution function over the region of transmission then gives the total number of electrons which reach the collector:

$$N(V_A, \gamma) = N_T \int_0^{\infty} dE_{\perp} \int_{-eV_A + \gamma E_{\perp}}^{\infty} dE_{\parallel} \, f(E_{\parallel}) h(E_{\perp}) , \qquad (3.C.i.1)$$

where N_T is the number of electrons which have passed through the collimator hole. Both $f(E_{\perp})$ and $h(E_{\perp})$ are normed to unity, i.e., $N(0,0) = N_T$. Two simple partial derivatives with respect to the lower limit of integration of the $E_{\parallel}$ variable yield:

$$\frac{\partial N(V_A, \gamma)}{\partial \gamma} = - N_T \int_0^{\infty} dE_{\perp} \, E_{\perp} \, h(E_{\perp}) \, f(-eV_A + \gamma E_{\perp}). \qquad (3.C.i.2)$$

$$\frac{\partial N(V_A, \gamma)}{\partial V_A} = e N_T \int_0^{\infty} dE_{\perp} \, h(E_{\perp}) \, f(-eV_A + \gamma E_{\perp}) \qquad (3.C.i.3)$$

If these derivatives are evaluted at $\gamma = 0$, then

$$\frac{\partial N(V_A, 0)}{\partial \gamma} = -N_T \, f(-eV_A) \int_0^{\infty} dE_{\perp} \, E_{\perp} \, h(E_{\perp}) \qquad (3.C.i.4)$$

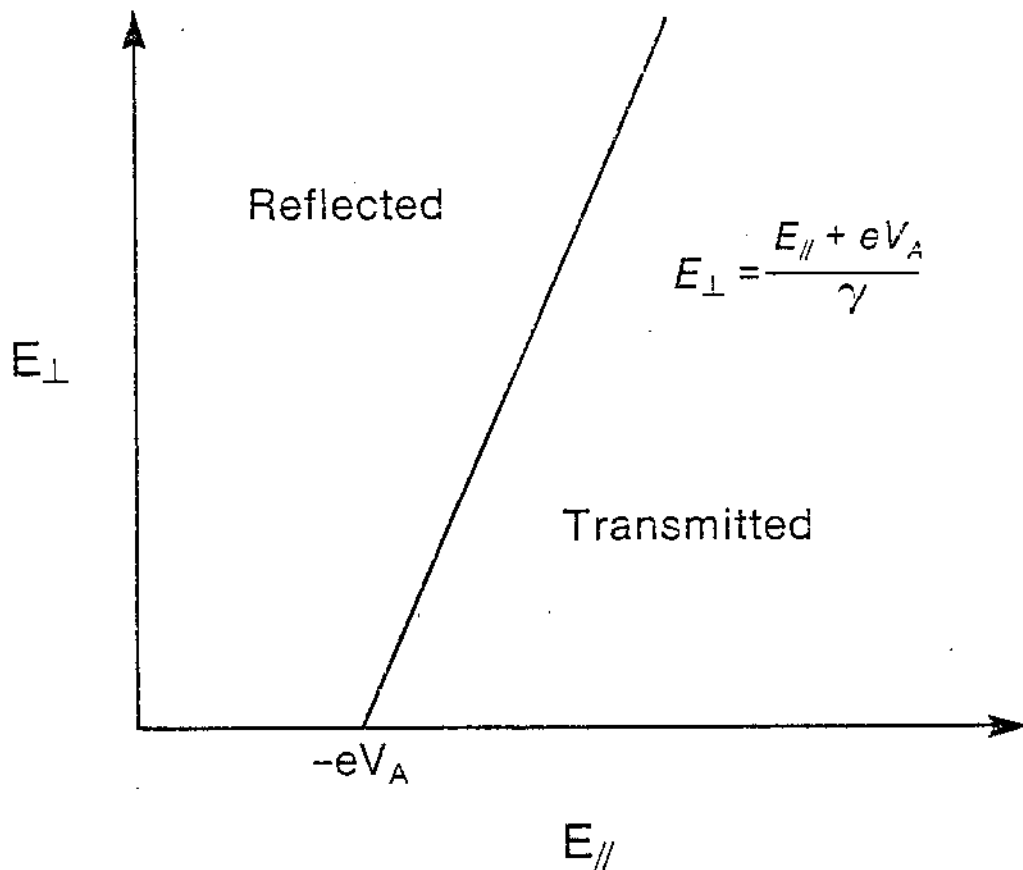Figure 9. Reflection and transmission regions in energy space. $E_\perp$, $E_\parallel$ are the electron perpendicular and parallel kinetic energies an electron has after it is dumped but is still far from the secondary solenoid. $-eV_A + \gamma E_\perp$ is the maximum effective barrier height presented to an electron of energy $E_\perp$.

58

$$\frac{\partial N(V_A, 0)}{\partial V_A} = e N_T \, f(-eV_A) \qquad\qquad (3.\,C.\,i.\,5)$$

and thus, if both derivatives are evaluated at the same value of $V_A = \tilde{V}_A$ chosen such that $f(-e\tilde{V}_A)$ is not zero), then

$$-e \left(\frac{\partial N(\tilde{V}_A, 0)}{\partial \gamma} \right) \Big/ \left(\frac{\partial N(\tilde{V}_A, 0)}{\partial V_A} \right) = \int_0^\infty dE_\perp E_\perp h(E_\perp) \equiv \langle E_\perp \rangle \, ,$$
$$(3.\,C.\,i.\,6)$$

where $\langle E_\perp \rangle$ is the average perpendicular kinetic energy of those confined electrons which are at the same radius as the collimator hole. This result is independent of the form of $h(E_\perp)$, and of $\tilde{V}_A$, as long as $f(-e\tilde{V}_A) \neq 0$ and $g(E_\parallel, E_\perp)$ is separable. Of course, if $h(E_\perp)$ is a Maxwellian distribution, then $\langle E_\perp \rangle = T_\perp$. The experimental details of how $\langle E_\perp \rangle$ is measured are given in Appendix C.

If the energy distribution function $g(E_\parallel, E_\perp)$ is not separable, then the measured value of $\langle E_\perp \rangle$ will be a function of $\tilde{V}_A$. A true measurement of $\langle E_\perp \rangle$ will then require an average of measured $\langle E_\perp \rangle$ over all $\tilde{V}_A$. Measurements of $\langle E_\perp \rangle$ at various $\tilde{V}_A$ values lead to the conclusion that to good approximation $\langle E_\perp \rangle$ is independent of $\tilde{V}_A$ and hence $g(E_\parallel, E_\perp)$ is separable. Figure 10a shows $N(V_A, 0)$, the transmitted electron charge (when $\gamma = 0$) as a function of V_A, for a plasma which is not yet in thermal equilibrium but was held long enough to be Maxwellian in kinetic energy. All measurements were taken on axis ($r = 0$). Figure 10b shows $\langle E_\perp \rangle$ measured
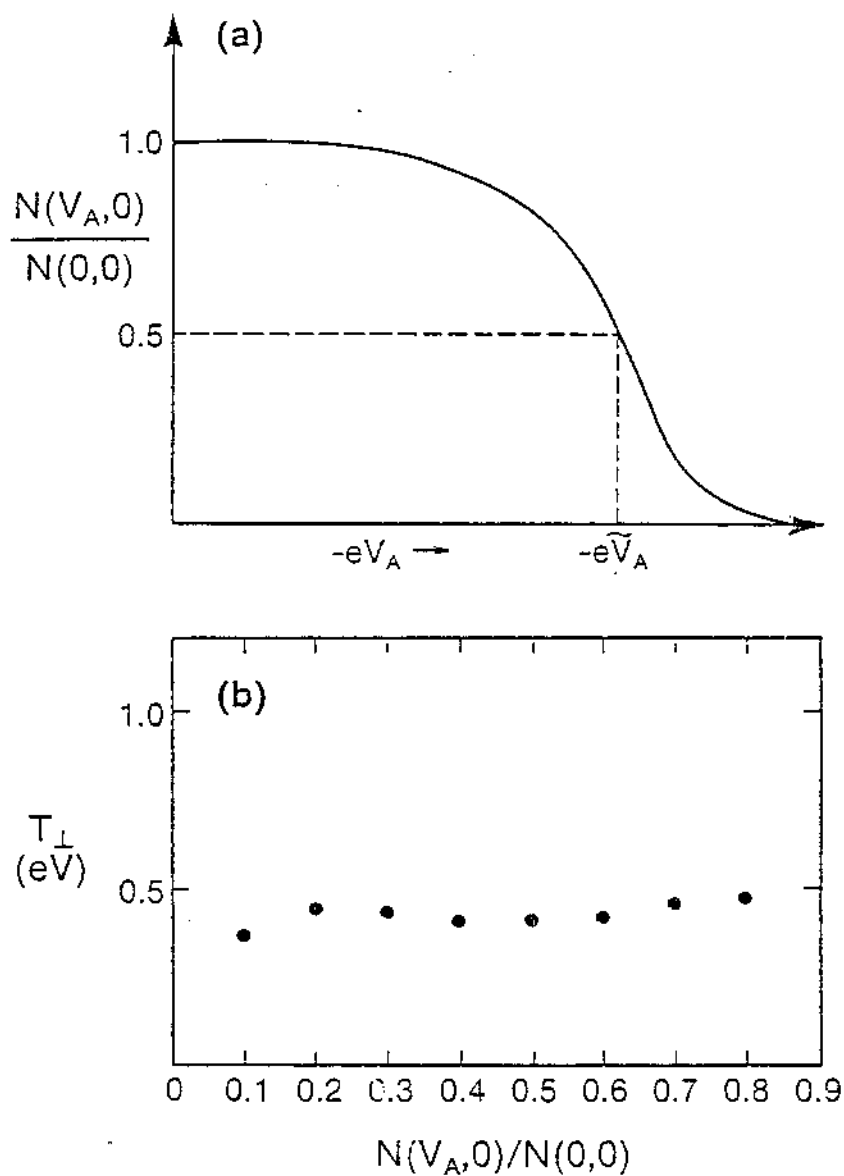
Figure 10. The transmitted portion of the total electron charge divided by the total charge is plotted against the maximum electrostatic barrier length, $-eV_A$, for the condition $\gamma = 0$ in (a). (b) shows $\langle E_\perp \rangle$ plotted as a function of relative transmitted charge, which is a function of V_A. The $\langle E_\perp \rangle$ values have errors of approximately $\pm 5\%$. $\tilde{V}_A$ is usually set to $\tilde{V}_A$, where $N(\tilde{V}_A, 0)/N(0, 0) = 0.5$ for all measurements of $\langle E_\perp \rangle$.

as a function of $\tilde{V}_A$. The x-axis is the relative signal, $N(V_A, 0)/N(0, 0)$. It can be seen that $\langle E_\perp \rangle$ is indeed independent of $\tilde{V}_A$ over a wide range. Measurements of $\langle E_\perp \rangle$ made as $\tilde{V}_A \to 0$, (i.e. $N(\tilde{V}_A, 0)/N(0, 0) \to 1$) and as $\tilde{V}_A \to \infty$ (i.e. $N(\tilde{V}_A, 0)/N(0, 0) \to 0$) were not made since each limit requires measuring two very small (and hence uncertain) slopes and then dividing them. We believe that the $\langle E_\perp \rangle$ measurement is to good approximation independent of $\tilde{V}_A$ when $N(\tilde{V}_A, 0)/N(0, 0) \sim 1/2$.

Although we expect $E_\parallel$ and $E_\perp$ to be somewhat coupled during the evolution of a velocity space anisotropy (due to the velocity dependence of the Coulomb cross-section), we also expect that the dis-assembly process would act to decouple $E_\parallel$ and $E_\perp$. This is due to the fact that the spatial separation of two electrons with the same $E_\parallel$, $E_\perp$ will most likely result in different parallel energies after the disassembly, which is dominated by space charge potential energy conversion. A study of the possible dependence of $\langle E_\perp \rangle$ as a function of V_A during the collisional relaxation was not undertaken. We be-lieve that the net effect any residual coupling would have on our meas-ured rates is small. However, this effect remains as a possible source of a small systematic error.

(ii) Parallel Temperature Measurement

The $T_\parallel$ measurement technique described here is not well suited for a precision measurement of the anisotropic relaxation rate since only the temperature of the energetic tail of the velocity distribution is actually measured. The average parallel kinetic energy of the entire distribution can be inferred if the distribution is Maxwellian. Hence the $T_\parallel$ measurement does serve as an independent check of the $T_\perp$ measurement when the plasma is in equilibrium. Also, data obtained with both the $T_\parallel$ and $T_\perp$ measurements at various times during the evolution of the anisotropic relaxation give striking evidence of the creation and subsequent relaxation of that anisotropy, as is shown in Figure 5. Thus, while the $T_\parallel$ data is not used in the analysis which yields the relaxation rates, the $T_\parallel$ measurement served a useful purpose in this study.

The measurement technique gives an experimentally simple method of measuring $T_\parallel$, the parallel temperature of a Maxwellian plasma, to an accuracy of about 10%. The method consists of slowly decreasing the dump barrier height, thus allowing the most energetic electrons to escape first. The rate at which charge escapes as the barrier height is reduced then yields $T_\parallel$, at least within the confines of several rather severe restrictions. These restrictions are mostly due to considerations of theoretical tractability and simplicity. Necessary corrections to the simple model are discussed. The experimental procedure and the analysis of the data is described.

The parallel temperature diagnostic used in this study is a result of the contributions of many in the Malmberg group. Measuring $T_\parallel$ by measuring the parallel kinetic energy of the dumped plasma must contend with the complications of the dump process itself converting the relatively large space charge energy of the plasma into parallel kinetic energy. The measurement technique used here represents a partial solution to this problem. It has the advantage of measuring $T_\parallel$ in one shot, but also has some disadvantages. These disadvantages are: $T_\parallel$ can be measured only on axis ($r = 0$); the value of $T_\parallel$ measured must be corrected for factors that vary with different plasmas, and each correction can be of the order of 10%; and, most importantly, the actual measurement is made only over the energetic tail of the parallel velocity distribution, $f(v_\parallel)$. If $f(v_\parallel)$ is not Maxwellian, then this measurement technique gives only an average energy scale characteristic of the energetic tail of $f(v_\parallel)$. See Appendix D. A technique which allows a more comprehensive measurement of $T_\parallel$, including measurement at $r \neq 0$ and effective measurement over the entire distribution, has been developed by Eggleston.[54] However, this technique is very computationally involved and time consuming, and was not used in this study.

The $T_\parallel$ measurement deals with the space-charge energy to kinetic energy conversion problem in a straightforward way. By employing a technique which allows a simple model of the dump

63

process to be made, a straightforward analysis of that model, at least during the initial stages of the dump, can be accomplished. The technique which simplifies the dump process is to slowly reduce the confining potential energy barrier by ramping V_d, the potential applied to the dump gate, to ground. This ramping is done on a time scale which is very slow compared to an electron axial bounce time, yet which is very fast compared to a collision time. This is the same time scale ordering required for the 1-D compression, see Appendix A. The relatively large bounce frequency insures that electrons in the plasma will encounter the dump gate barrier at a given barrier height, since the barrier doesn't essentially change over the time required for any electron to travel the length of the plasma. For simplicity, further assume that the dump gate is very long in comparison to its diameter. Then the maximum potential barrier height is given by $-eV_d$, and is essentially independent of radius. (It turns out that a quadratic radial dependence doesn't affect the measurement.) At some point during the slow reduction of the barrier height, the most energetic electrons will begin to escape past the barrier. We can then ask how many electrons escape as a function of V_d.

In the absence of any collisions, the sum of the potential and parallel kinetic energies of each electron remains essentially fixed throughout the process. We can then evaluate this sum at any axial position, and it is simplest to do so at $z = 0$, the axial center of the plasma. Each electron will escape past the dump barrier when this

sum exceeds $-eV_d$, the barrier height:

$$-e\phi(r, 0) + \frac{1}{2} mv_{\parallel}^2 v_{\parallel}^2 \geq -eV_d \qquad (3.\,C.\,ii.\,1)$$

is the condition for the escape of any electron at radius r. We expect the first electrons to escape will be on or near the axis ($r = 0$), where the space charge potential energy is the most negative.

We can now calculate the escaped charge as a function of the barrier voltage, V_d . Several simplifying assumptions and restrictions will be necessary to keep the calculation analytically tractable. Within these assumptions, we will find that at least initially the charge escapes from a region of a few λ_D about the axis and that the total escaped charge displays (to an accuracy of about 10%) an exponential dependence upon the barrier height $-eV_d$ with $T_{\parallel}$ as the characteristic scale. One of the restrictions necessary to derive this result is that $T_{\parallel}$ be measured only over the energetic tail of $f(v_{\parallel})$, the parallel velocity distribution of the confined plasma.

Assume that $f(v_{\parallel})$ is independent of r and z, and is normed so that its integral over all $v_{\parallel}$ is unity. The total number of escaped electrons, $Q_e(r_0; r_c)$, which pass through the collimator hole (of radius r_c centered on position r_0), is then calculated as a function of V_d by integrating $f(v_{\parallel})\, n(r, z)$, the initial confined electron distribution function, over all z; the collimator hole area; and $v_{\parallel}$, using equation (3.C.ii.1) as the lower velocity limit:

$$Q_e(r_o; r_c) = -e \int_{\text{all } z} dz \int_{\substack{\text{collimator} \\ \text{area}}} da\, n(r,z) \int^{\left[-\frac{2e}{m}(V_d - \phi(r,0))\right]^{1/2}} dv_{||}\, f(v_{||}) \ , \qquad (3.\,C.\,ii.\,2)$$

where $\phi(r,0)$ is the self-consistent potential:

$$\nabla^2 \phi(r,z) = 4\pi e\, n(r,z) \int_0^{\left[-\frac{2e}{m}(V_d - \phi(r,0))\right]^{1/2}} dv_{||}\, f(v_{||}) \ .$$

$$(3.\,C.\,ii.\,3)$$

Equation (3. C. ii. 3) simply adjusts the value of ϕ to reflect the diminished space charge as electrons escape. Strictly speaking, the instantaneous value of V_d must form part of the boundary conditions, but for long plasmas, end effects are unimportant and an infinite length plasma calculation of $\phi(r,z)$ suffices.

We restrict the analysis of equations (3. C. ii. 2) and (3. C. ii. 3) to the regime of approximately Maxwellian distributions of temperature $T_{||}$, and for V_d such that $-e(V_d - \phi)/T_{||} \gg 1$. Then to good approximation the upper limit of the $v_{||}$ integral in equation (3. C. ii. 3) can be set to infinity. So few electrons have escaped that we can approximate the potential by the initial potential, ϕ_o, so that $\phi(r,0) \cong \phi_o(r,0) = $ constant independent of V_d. Let the escaped charge calculated using this assumption be $Q'_e(r_o; r_c)$. We assume a given $f(v_{||})\, n(r,z)$ and ask when Q'_e significantly diverges from Q_e calculated using the fully self-consistent $\phi(r,z)$. This has been

done on a computer[55] for a plasma with a Maxwellian $f(v_\parallel)$, a density $n(r, z)$ that is constant in radius over several λ_D, and a length that is independent of r. The condition that $Q_e' \simeq Q_e$ is then found to be that the central density may only decrease by about 1%. Further, within this limit, electrons only escape from a region which is a few Debye lengths in radius about the axis. Thus the approximation $\phi(r, 0) \simeq \phi_0(r, 0)$ is valid for the near Maxwellian velocity distributions expected in this study, as long as: 1) the analysis is done only on the axis, and 2) the analysis is limited to observation to the first 1% of the escaped electrons. These electrons have velocities larger than about two thermal velocities $(2\bar{v}_\parallel)$.

(The above discussion is valid only for plasma columns whose radii are greater than a few Debye lengths, that is, plasmas whose space charge potential energy is much larger than its kinetic energy. For very dilute or very hot plasmas whose column radii are much smaller than a Debye length, temperatures can be measured at any radius, and $\phi(r, 0) \simeq 0$ is a good approximation which remains valid for most, if not all, of the disassembly.)

With a few more reasonable assumptions, equation (3. C. ii. 2) can be analytically integrated to give the dependence of Q_e upon V_d. We assume 1) a density that is constant over the collimator hole area, which is centered on the axis; 2) the plasma is long enough to neglect end effects; 3) the tail of the parallel velocity distribution is

Maxwellian with a temperature, $T_{\parallel}$, that is independent of radius.

We write the escape condition as $v_e = \left[-\frac{2\dot{e}}{m} (V_d - \phi_o(r, 0)) \right]^{1/2}$,

and rewrite equation (3.C.ii.2) as

$$Q_e(0, r_c) \cong -e L_p n_o \int_0^{r_c} r\, dr \int_{v_e}^{\infty} dv_{\parallel} f(v_{\parallel}) \qquad (3.C.ii.4)$$

where

$$f(v_{\parallel}) = \left(\frac{2m_e}{\pi T_{\parallel}} \right)^{1/2} \exp\left[-mv_{\parallel}^2 / 2T_{\parallel} \right]$$

We find $\phi_o(r, 0)$ from assumptions (1) and (2) and Poisson's equation

$$\phi_o(r, 0) \cong -\pi e n_0 \left[\left(1 + 2 \ln \frac{R_\omega}{r_c} \right) r_c^2 - r^2 \right] + \psi_> \qquad (3.C.ii.5)$$

over the range $0 \le r \le r_c$, where R_ω is the cylinder radius and $\psi_>$ is the constant contribution to the inner region $(r < r_c)$ potential due to all charge outside of r_c. Note $\phi(r, 0) = \phi_o + \pi e n_o r^2$ in the region of interest, where ϕ_o is the space charge potential on axis. (See Appendix D for an alternate form of equation (3.C.ii.4) suitable for an arbitrary velocity distribution).

Equation (3.C.ii.4) can then be integrated to give:

$$Q_e(0, r_c) \cong -n_o e L_p (2\lambda_D)^2 \left[\frac{x^2}{2} \operatorname{erfc}(x) + \frac{1}{4} \operatorname{erf}(x) - \frac{xe^{-x^2}}{2\sqrt{\pi}} \right]_{\beta}^{[\beta^2 + (r_c/2\lambda_D)^2]^{1/2}}$$

$$(3.C.ii.6)$$

where $erf(x)$, $erfc(x)$ are the error function and its complement, and $\beta^2 = -e(V_d - \phi_o)/T_{\parallel}$ is the smallest scaled energy of any of the escaped electrons on the axis. Since $\beta \geq 2$ by restriction (i.e., the electrons which have escaped on the axis have stayed within the restriction $v_{\parallel}/\bar{v}_{\parallel} \geq 2$), we use the asymptotic expansion of $erfc(x)$ to obtain the approximate solution

$$Q_e(0, r_c) \simeq -\left(\frac{n_o e L_p}{2\sqrt{\pi}}\right) \pi (2\lambda_D)^2 \frac{e^{-\beta^2}}{\beta} \left(1 - \frac{e^{-r_c^2/(2\lambda_D)^2}}{[1 + (r_c/2\lambda_D \beta)^2]^{1/2}}\right).$$

(3.C.ii.7)

As $r_c/2\lambda_D \to 0$ (small collimator hole limit),

$$Q_e(0, r_c) \to -\left(\frac{n_o e L_p}{2\sqrt{\pi}}\right) \pi r_c^2 \frac{e^{-\beta^2}}{\beta} ;$$

(3.C.ii.8)

and as $r_c/2\lambda_D \to \infty$ (large collimator hole limit),

$$Q_e(0, r_c) \to -\left(\frac{n_o e L_p}{2\sqrt{\pi}}\right) \pi (2\lambda_D)^2 \frac{e^{-\beta^2}}{\beta} .$$

(3.C.ii.9)

We then find that, upon taking the natural logarithm of $-Q_e(0, r_c)$ in equation (3.C.ii.7), and differentiating with respect to V_d,

$$\frac{1}{e} \frac{d}{dV_d} \ell n \, (-Q_e(0, r_c)) \simeq \frac{1}{T_{\parallel}} \left(1 + \frac{1}{2\beta^2} + P(r_c^2/(2\lambda_D)^2, \beta^2)\right),$$

(3.C.ii.10)

69

where $P(r_c^2/4\lambda_D^2, \beta^2)$ gives a small ($\sim 10^{-2}$ maximum) correction due to finite collimator hole size, and can be neglected. The $(2\beta^2)^{-1}$ term can be neglected at the 10^{-1} accuracy level (10%), since $\beta^2 \geqslant 4$.

The $T_{\parallel}$ measurement is implemented by digitizing the output of the collector amplifier, the gain of which is chosen so that the digitizer saturates when about 2%-5% of the total possible charge has escaped through the axially centered collimator hole. The clock rate is typically 1 MHz; the digitizer resolution is 10 bits; and there is 8K of digitizer memory. Another digitizer, which is driven by the same clock as the first digitizer, is used to measure V_d. The clock is triggered by a timing pulse which also starts a linear ramping of V_d towards ground. The ramping rate is chosen so that the 1-D expansion conditions are met. The digitized information is supplied to the system computer, which searches the Q_e data for the point of saturation, brackets this point with a window, and displays the Q_e and V_d data within this window on a monitor screen. Also displayed is the natural log of the Q_e data. The window is chosen to be large enough so that a properly zeroed baseline for the Q_e data can be calculated. If necessary, a linear slope can also be removed from Q_e. These manipulations (prior to taking the log) may be required to remove low frequency (acoustic) noise generated by microphonics in the EV device and its associated cabling. The logarithm of the treated Q_e is then taken (a very small

arbitrary lower bound to Q_e is enforced to prevent divergence of the log), and a linear regression algorithm is used to least-squares fit a straight line (between two experimenter chosen end points) to the logarithm of the Q_e data. The end points are visually chosen to cover the log data which is most nearly straight, and to include as many decades of Q_e data as possible, within the "nearly straight" restriction. This is typically 1.0-2.5 decades of Q_e; 3 decades of data can be displayed with 10 bit resolution. Figure 11 shows a sample of the Q_e and $\ln[Q_e]$ data, along with V_d data, as seen on the computer monitor screen.

The slope of V_d is similarly measured, using the same window. Since each slope is measured with respect to time (or clock rate) as the independent variable, it is easy to attain the desired slope by evaluating the ratio:

$$\langle \Delta \ln Q_e / \Delta t \rangle / \langle \Delta V_d / \Delta t \rangle \cong \langle \Delta \ln Q_e \rangle / \langle \Delta V_d \rangle \approx e T_{\parallel}^{-1} \qquad (3.\,C.\,ii.\,11)$$

The brackets denote the least-squares fitting of a single slope over the chosen region of ϑ^2; the value of $T_{\parallel}$ thus measured is about 10% lower than the actual $T_{\parallel}$ as can be seen from equation (3.C.ii.10).

A word should be said about the possibility of the measurement of Q_e being contaminated by a diocotron instability caused by the increasingly hollowed out radial density profile.[56] This instability could cause a local increase in plasma potential, which would in turn allow an excess of electrons to penetrate V_d. No obvious signature,
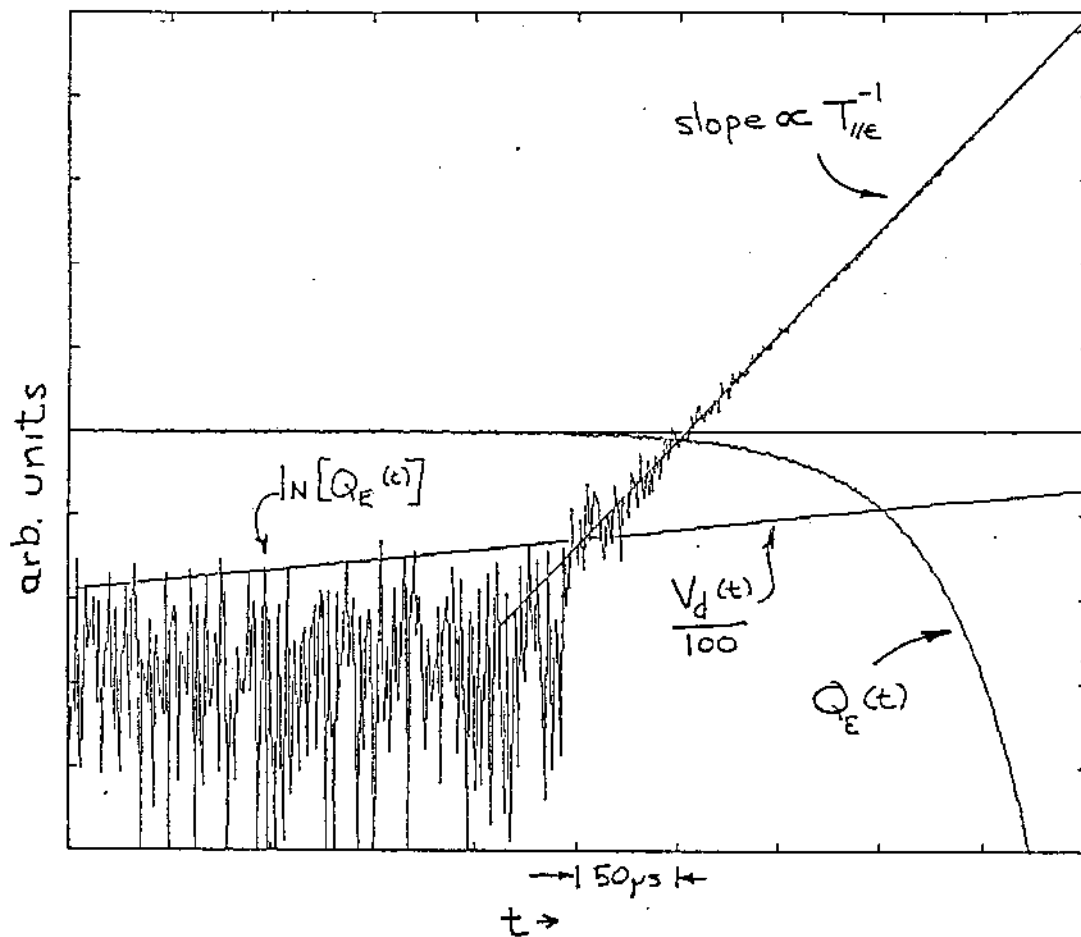
Figure 11. Plot of digitized $Q_e(t)$, $\ln |Q_e(t)|$, and $V_d(t)$ as functions of t. Imposed upon the $\ln |Q_e|$ data is a fitted straight line in the region of significant Q_e. The vertical logarithmic scale covers 4 decades. As can be seen, the behavior of $\ln|Q_e|$ is essentially linear over about 3 decades of Q_e data.

such as staircasing, is observed in the restricted region $\beta^2 \geq 4$, although staircasing has been observed when the central density has decreased by more than 10% or so. Since the conditions of the measurement restrict the hollowing to a very small amount, we believe there is no contamination due to the diocotron instability.

This constitutes the basic measurement of $T_\parallel$. As has been noted here, and is shown further in Appendix D, this measurement is really only a measure of the energy scaling of the high velocity ($v_\parallel \geq 2\bar{v}_\parallel$) tail of the parallel velocity distribution. Unlike the $\langle E_\perp \rangle$ measurement, it does not measure the average energy of the entire distribution, and thus we expect it to be an increasingly inaccurate description of the distribution as it further deviates from a Maxwellian.

Due to the relative unimportance this diagnostic has in obtaining the measured relaxation rates, a special effort to improve the accuracy was not undertaken. A short list of those corrections which were made is: (1) the fitted $T_\parallel$ was increased by approximately 10% (depending upon the range of β^2 actually fitted) to correct for the $(2\beta^2)^{-1}$ term in equation (3.C.ii.10); (2) the potential at the center of the finite length dump gate was used instead of the applied potential V_d (giving a reducing correction to $T_\parallel$ of approximately -10%, depending upon dump gate length); and (3), a correction of approximately +10% to +40% (depending upon the

confined plasma length and V_d) to $T_\parallel$ is made to account for the inevitable $T_\parallel$ cooling the fully confined plasma suffers as the plasma expands while V_d is ramped to ground. The correction is calculated by utilizing the density measurement to determine the fully confined axial path length, $L(2\overline{v}_\parallel)$, of those electrons with $v_\parallel = 2\overline{v}_\parallel$, and then estimating the correction from a 1-D axial expansion. The electrons are assumed deconfined when they cross the geometrical boundary separating the dump gate and confinement cylinder. The percentage correction, ε, is then calculated as a 1-D expansion (see Appendix A):

$$\varepsilon = \left(\frac{1}{2} L(2\overline{v}_\parallel) + \frac{1}{2} L_{geo}\right)^2 / L^2(2\overline{v}_\parallel) , \qquad (3.C.ii.12)$$

where L_{geo} is the geometric length of the confining volume.

There are additional effects which could conceivably also generate $\sim 10\%$ corrections to the value of $T_\parallel$. These include: (1) the effect of a finite V_d potential ramp rate, which can cause electrons at the far end of the plasma to exit at a lower potential barrier than expected, thus broadening the class of velocities that escape at a given V_d; (2) the effect of the plasma space charge on the analyzing potential (the effective barrier height); (3) the effect of the space charge on the axial position of deconfinement. There are probably others.

We conclude this section on the $T_\parallel$ diagnostic by noting that the many corrections to the basic measurement, both known and

unknown, argue against success in improving the accuracy beyond the 10% level. Fortunately, the measurement of relaxation rates does not depend upon an accurate measurement of $T_\parallel$. In this study, the $T_\parallel$ measurement was utilized only to provide an independent check on the $T_\perp$ temperature of a plasma in equilibrium, to illustrate the relaxation of the tail of the distribution, and as an initial indication of the validity of the 1-D compression model (see Appendix A). When used as a check of $T_\perp$ (with all corrections made), $T_\perp = T_\parallel$ to within about 10%, and the error in $T_\perp$ is believed to be about 5%. Figure 12 shows a comparison between measured values of $T_\perp$ and $T_\parallel$, and shows the values of $T_\parallel$ when all corrections are made. Finally, in order to avoid confusion, the symbol "$T_{\parallel e}$", meaning the "temperature" of the energetic tail of $f(v_\parallel)$, is used to denote a measured value using the $T_\parallel$ measurement technique.

(iii) Density and Potential Measurement

This measurement involves the use of a computer code to calculate the density and potential as functions of r and z from the measured data set. This data set consists of measurements of $Q(r)$, the amount of charge in a tube centered at radius r, whose cross-sectional area is that of the collimator hole and whose length extends axially through the plasma, and $T(r)$, the temperature. The computational technique was previously employed by Prasad to check theoretical predictions of plasma equilibria.[44] The technique was later
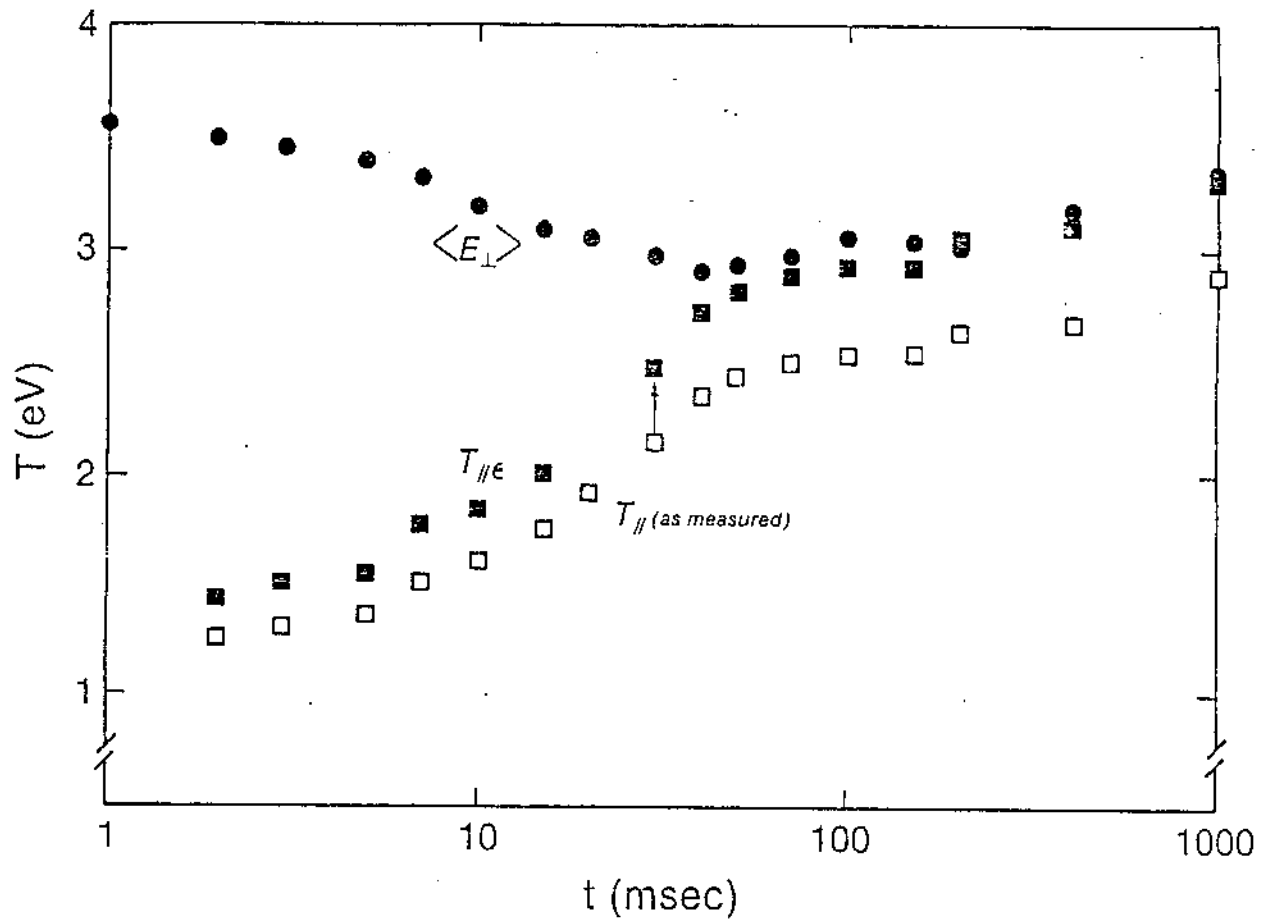
75

Figure 12. The measured values of $\langle E_\perp \rangle$ and $T_{\parallel e}$ are plotted on semi-log axes as a function of time. The raw $T_{\parallel e}$ data are given by the open boxes; each is the measured value $\Delta \ln |Q_e| / \Delta V_d$. The solid boxes represent corrected $T_{\parallel e}$ values.

modified to accept experimental data by Fine and Driscoll.[57] The code computes the density, $n(r,z)$, and the potential, $\phi(r,z)$, self-consistently using a 2-D form of Poisson's equation. Cylindrical symmetry is assumed. The confinement geometry and applied confinement potentials supply the boundary conditions. The measured $Q(r)$ and $T(r)$ data, when coupled with an assumption of local thermal equilibrium along field lines, provide equations of constraint from which $n(r,z)$ and $\phi(r,z)$ are uniquely determined.

There is one $Q(r)$ measurement made per plasma shot. $Q(r)$ is a measurement of the total charge that passes through the collimator hole (area $= A_c$), which is centered at radius r. $Q(r)$ is typically measured at 30 to 50 different radii. By neglecting the small radial polarization drift caused by the dump process (see Appendix F), we assume that the electrons remain at the same radius when dumped, and thus $Q(r)$, the number of electrons which pass through the collimator hole positioned at radius r, can be calculated from the confined plasma density $n(r,z)$ as

$$Q(r) = -e \iint_{A_c} dxdy \int_{\text{all } z} dz \, n(r,z) \simeq -eA_c \int_{\text{all } z} dz \, n(r,z) \quad (3.C.iii.1)$$

The collimator hole radius is 0.32 cm, which is typically one Debye length or smaller.

Applying the assumption of local thermal equilibrium along field lines, which can be written as

$$n(r, z) = C_o(r) \, e^{-e\phi(r, z)/T_{\parallel}(r)} \quad , \qquad (3.C.iii.2)$$

where $C_o(r)$ is determined by insertion of (3.C.iii.2) into (3.C.iii.1),

requires knowledge of $T_{\parallel}(r)$. We can deduce a value for $T_{\parallel}(r)$ by

measuring $T_{\perp}(r)$ when the plasma is in equilibrium. In equilibrium,

$T_{\parallel}(r) = T_{\perp}(r)$. The $T_{\parallel e}$ measurement employed in this study cannot

be directly used since it is valid only on the axis. $T_{\perp}(r)$ is typically

measured at 8-12 different radii. The large number of shots required

to measure $T_{\perp}$ usually has the effect of keeping the number of $T_{\perp}(r)$

data points smaller than the number of $Q(r)$ data points. Figure 3c

shows a typical set of $Q(r)$ and $T_{\perp}(r)$ measurements for a plasma

near equilibrium.

A computer program takes the $Q(r)$, $T_{\perp}(r)$ data as input and

self-consistently solves the 2-D Poisson equation,

$$\nabla^2 \phi(r, z) = 4\pi e n(r, z) \quad . \qquad (3.C.iii.3)$$

The program uses a fast Fourier transform to calculate an initial

potential $\tilde{\phi}(r, z)$ from the boundary conditions and an initial density

$\tilde{n}(r, z)$ calculated on an r, z grid from the assumption that $\tilde{n}(r, z)$ is

uniformly distributed in z between the confining end cylinders, and

from the requirement that measurements of this initial density repro-

duce the measured $Q(r)$. The grid typically has 64×128 cells.

(Care must be taken to insure at least two cell lengths per Debye

length in both r and z.) With $\tilde{\phi}(r, z)$ calculated, a new $\tilde{n}(r, z)$ is

calculated using (3.C.iii.1) and (3.C.iii.2). A variable percentage of the new $\tilde{n}(r,z)$ is added to the old $\tilde{n}(r,z)$ and a new $\tilde{\phi}(r,z)$ is calculated. This process is iterated until the new and old densities have a maximum percentage difference of less than 0.1% in any cell. At this point the final densities and potentials are self-consistent to about 0.1%; these are the measured values of $n(r,z)$ and $\phi(r,z)$.

A couple of points concerning the $Q(r)$ and $T_\perp(r)$ data should be made. The solution to (3.C.iii.3) using 64 cells in the radial direction requires values of $Q(r)$ and $T_\perp(r) = T_\parallel(r)$ at 64 different radii to fill these cells. The measured $Q(r)$ and $T_\perp(r)$ data set does not usually fit this requirement. Also, the exact location of the collimator hole center relative to the cylinder axis may be in error by up to about 1 mm. This means the actual positions of the $Q(r)$, $T_\perp(r)$ data displayed in Figure 3c could be shifted as a group to the right or left by up to 1 mm. 1 mm is greater than one cell length when a grid of 64 radial cells is used. The program handles this possible shift by first calculating the radial offset to the $Q(r)$ data that results in equal numbers of electrons for both $r < 0$ and $r > 0$, and then fitting smoothed curves through the average of the offset $Q(r)$, $T_\perp(r)$ data and the offset $Q(r)$, $T_\perp(r)$ data reflected through the axis. The values of $Q(r)$, $T_\perp(r)$ at the appropriate radii are then taken from these adjusted curves and supplied as input to the subprogram that calculates the self-consistent $n(r,z)$ and $\phi(r,z)$.

The accuracy of the n and ϕ measurement depends critically upon the accuracy with which the charge, $Q(r)$, is measured by the charge collection circuitry and the collection efficiency of the charge collecting electrode. (The $T_\perp$ and $T_{\parallel}$ measurements are not critically dependent upon the charge measurement accuracy, since the $T_\perp$ measurement involves ratios, and the $T_{\parallel}$ measurement involves the derivative of the log of Q.) The collecting electrode is typically biased from +100 V to +180 V, with cylinders A1-A4 biased from +9 V to +45 V, in order to enhance collection efficiency. The gain and total effective capacitance of the charge collection circuitry were carefully calibrated to about ± 3% overall.

The accuracy of the n and ϕ measurement depends upon an accurate measurement of $Q(r)$. A check of the accuracy of the $Q(r)$ measurement is made by integrating the measured $n(r, z)$ over the entire confinement volume and comparing the resultant total charge with a measurement of that total charge by utilizing the collimator plate, which has a separate charge collection circuit (similar to the circuit of the collecting electrode), as a collector. These agree to within about 1% to 2%. An independent check can be made by measuring the image charge on one central confinement cylinder when a long plasma is confined. From Gauss' Law, this measured image charge should be equal to the integral of the measured $n(r, z)$ over

the volume of the cylinder. This check also agrees to within 5%.[57] We thus consider the density $n(r, z)$ and potential $\phi(r, z)$ to be accurate to within 5%.

IV. Measurement of the Anisotropic Temperature Relaxation Rate

The anisotropic temperature relaxation can easily be measured after the initial anisotropy is created in the sample plasma. The temperature on axis is measured as a function of time after creation of the anisotropy. The density is measured after the plasma has relaxed. The difference between the instantaneous measurement of the mean perpendicular energy, $\langle E_{\perp}(t) \rangle$, and the final equilibrium temperature, T_f, displays an essentially exponential relaxation behavior. The measurement of the "temperature" of the tail of the parallel distribution, $T_{\parallel \epsilon}(t)$, is likewise analyzed, and shows similar relaxation behavior but with a longer characteristic time scale. This discrepancy in rates is explained by the energy dependence of the collisional Coulomb cross-section.

The data is also analyzed by applying a non-linear least-squares fit of the solution to the Ichimaru-Rosenbluth relaxation model equation (2.D.9). This equation is shown to produce near-exponential relaxation over the range of anisotropies utilized in this study. The rates obtained by this analysis statistically agree with the theoretical prediction of Ichimaru-Rosenbluth modified by the Montgomery-Joyce-Turner approximation to within about 5%, which is well within the approximate 10% uncertainty in the theoretical rate calculation.

Possible sources of systematic errors are analyzed, and an upper limit to overall systematic error of approximately 10% is estimated.

A. Raw Data Measurement

A relaxation measurement is made in the following sequence: 1) The plasma sample is prepared with the desired initial density and thermal equilibrium temperature $T_\parallel = T_\perp = T_i$. 2) The desired anisotropy is induced by a 1-D compression or expansion. 3) $\langle E_\perp(t) \rangle$, and $T_{\parallel e}(t)$, are measured on the axis at various times after the anisotropy is created. The times are chosen to cover the relaxation from the initial anisotropy to the equilibrium temperature T_f . 4) The density, $n(0, z)$, is measured after the anisotropy relaxes to equilibrium. 5) The raw data is then analyzed to reduce the measured relaxation to a single rate for comparison with theory.

The plasma sample preparation may include the use of the density fluctuation reduction technique; this allows the measurement of $\langle E_\perp(t) \rangle$, etc., with greater statistical accuracy for a given number of shots. The technique was discovered by K. Fine[57] late in the game, however, so there are many rates measured without its benefits.

From theoretical considerations we would like to keep the initial anisotropy as small as possible $(T_\parallel \simeq T_\perp)$; this would keep the $v_\parallel$ and $v_\perp$ distributions very close to Maxwellian throughout the relaxation. Practical considerations of the uncertainties involved in

measuring the temperatures would argue for large anisotropies ($T_{\parallel} \gg T_{\perp}$ or $T_{\parallel} \ll T_{\perp}$) so that they can easily be observed. The relevant quantity is the measured relative anisotropy defined as $(\langle E_{\perp}(t) \rangle - T_f)/T_f$, where T_f is the final equilibrium temperature. The initial anisotropy can be estimated from the 1-D approximation $(T_{\parallel}/T_{\perp})_i \simeq (L_u/L_c)^2$, where L_u, L_c are the plasma lengths estimated by the axial separation between the chosen confinement barrier cylinders when the plasma is uncompressed and compressed.

All relaxation rates are measured on the plasma axis ($r = 0$) using the 1/4" diameter collimator hole. The reasons for choosing the axis are twofold. First, the $T_{\parallel e}$ measurement is valid only on the axis. Second, the radial density and temperature variations are smallest on the axis, and, in fact, for all of the rates measured the density and temperature variations over one collector hole radius are negligible. For example, see Figure 3.

The density is easily measured after the anisotropy has relaxed and $T_{\parallel} = T_{\perp} = T_f$. A density measurement made during the relaxation of the anisotropy is more difficult to achieve, since $T_{\parallel}(r) \neq T_{\perp}(r)$, and $T_{\parallel}$ cannot be measured off the axis by the $T_{\parallel e}$ measurement. We would like to know if the density at $r = 0$ changes during the relaxation, and by how much. An estimate of the initial density is made by calculating $T_{\parallel}(r)$ from the measured values of T_f and $T_{\perp}(r)$, and supplying those calculated values along with the

measured $Q(r)$ data as input to the density solving computer code. A comparison of the average initial density (see equation (4.B.5)) estimated this way with the average density measured after the relaxation shows a difference on the order of 1%. The density is thus assumed to be constant during the relaxation. The average densities used in the analysis are therefore measured after relaxation to equilibrium.

The anisotropic temperature relaxation rate of a plasma with a given density and T_f is derived from an analysis of the time evolution of $\langle E_\perp \rangle$ measured at various times during the relaxation. Figure 5 shows a typical data set of measured temperature evolution. For completeness, and to graphically show that both the $v_\perp$ and $v_{\parallel}$ distributions do relax to equilibrium, both $\langle E_\perp \rangle$ and $T_{\parallel\varepsilon}$ data are plotted as functions of time. On this graph, the time, t, starts at the beginning of the plasma expansion. During times $t < 0$, the plasma is captured and prepared so that just before the expansion the plasma is close to global thermal equilibrium at temperature $T_i = 1.47$ eV. At $t = 0$, the expansion begins and lasts for approximately 1 msec. At the end of this expansion, the parallel temperature is lowered by approximately a factor of three, while the perpendicular temperature is only slightly affected. Note the two $T_{\parallel\varepsilon}$ measurements at $t < 0$ and $t = 1$ msec. (All of the $T_{\parallel\varepsilon}$ measurements incorporate all of the corrections discussed in section 3.D.ii.)

The time evolution of the relaxation is then measured at various times $t \geq 1$ msec by the $\langle E_\perp \rangle$ and $T_{\|\epsilon}$ measurements. Each $\langle E_\perp \rangle$ value requires hundreds of shots, and each $T_{\|\epsilon}$ value plotted is the average of a few hundred individual measurements of $T_{\|\epsilon}$. Characteristic error bars are shown on the $t = 10$ msec data points. The two solid lines are given by a simple exponential relaxation model least squares fitted to the data. This model is discussed in the next section. Note that there is data taken well after the relaxation has decayed which clearly shows that the final temperature, T_f, is essentially constant over a time comparable to the relaxation time.

The relaxation to equilibrium displayed by the $\langle E_\perp \rangle$ data is clearly more rapid than that displayed by the $T_{\|\epsilon}$ data. This difference is explained in the next section as due to the fact that the $T_{\|\epsilon}$ measurement extends only over the energetic tail of the parallel velocity distribution. The relaxation rate analyzed from $T_{\|\epsilon}$ data is then the rate at which a portion of the distribution relaxes. The rate displayed by the $\langle E_\perp \rangle$ data is due to an average of such rates over the entire distribution. It is for this reason that only rates derived from $\langle E_\perp \rangle$ evolution are compared with theory.

B. Simple Analysis of the Relaxation Rate

The relaxation data displayed in Figure 5 shows that the relaxation seems almost purely exponential. One is tempted to assume that the relaxation is indeed exponential and to then reduce the data to

a rate under this assumption. Such a course of action has the benefit of producing a rate which fairly accurately describes the experimental data without requiring an analysis of the data based upon the theoretical model of the relaxation proposed by I-R. This section discusses the analysis of the data using the simple exponential assumption. The data can also be reduced with the assumption that the theory of I-R describes the relaxation, and this procedure is followed in the next section.

We reduce the $\langle E_\perp \rangle$ data to a single rate by assuming a simple model of exponential relaxation of the anisotropy:

$$\langle E_\perp(t) \rangle - T_f = \exp\left[-\alpha t + \beta\right] \tag{4.B.1}$$

A weighted least squares fit of (4.B.1) to the data, with β and α as the fitting parameters, yields the rate. The data points are weighted by their calculated statistical errors.

The fitted value of β then gives the best fit value of the initial anisotropy. The fitted value of the parameter α is $\nu_\perp$, the measured relaxation rate. The statistical error in the value of $\nu_\perp$ is estimated by rewriting (4.B.1) as

$$\ln(\langle E_\perp(t) \rangle - T_f) = \ln \beta - \alpha t \quad . \tag{4.B.2}$$

The error in the fitted slope ($\nu_\perp$) is calculated from the statistical errors of two experimental points (one at $t = 0$ and one in the vicinity of $t = \nu_\perp^{-1}$). This serves as an estimate of the statistical error of

the fit. If there are other experimental points, the statistical error in $\nu_\perp$ is decreased as the square root of the number of points.

The same analysis procedure can also be applied to the $T_{\parallel \varepsilon}(t) - T_f$ anisotropy. As can be seen from the $T_{\parallel \varepsilon}(t)$ data of Figure 5, the measured value of $\nu_\perp$ using the $T_{\parallel \varepsilon}(t)$ data is significantly lower than the value found from the $\langle E_\perp(t) \rangle$ data. This is explained by the fact that the measurement of $T_{\parallel \varepsilon}$ is measured only in the energetic tail of the $v_\parallel$ distribution. The collisional relaxation of this high energy portion of the distribution is expected to be slower than that of the entire distribution.

This expectation comes from simple arguments. The relaxation rate is in some sense a measure of the collision frequency averaged over the distribution. The collision frequency, ν, is dependent upon the density and the velocity of the electrons:

$$\nu_{coll} \sim \sigma\, nv \qquad\qquad (4.B.3)$$

where σ is the collisional cross-section, and v is the relative velocity between two electrons. The Coulomb cross-section, σ, has the approximate form[50]

$$\sigma \simeq \frac{16\pi\, e^4}{m^2 v^4} \ln \Lambda \quad , \qquad\qquad (4.B.4)$$

where $\ln \Lambda$ is the Coulomb logarithm. The collision frequency is proportional to the inverse cube of the relative velocity between two

electrons. Therefore, the electrons in the energetic tail of the velocity distribution, which all have relatively large v, should relax at a slower rate than the bulk of the distribution, and this rate should become even slower as the measured portion of the distribution begins at higher energies in the tail.

A rough estimate of how much slower the $T_{\|\epsilon}$ measured anisotropy relaxes can be made by noting that the $T_{\|\epsilon}$ measurement covers only parallel velocities greater than or equal to about two parallel thermal velocities ($2\overline{v}_\|$). We approximate (4.B.3) as $\nu_\perp$, the bulk relaxation rate (as measured from $\langle E_\perp \rangle$ data), by calculating (4.B.3) for the average relative velocity of thermal particles interacting with a scattering background of thermal particles. The tail relaxation rate, ν_t, is similarly approximated for particles which have thermal perpendicular velocities and a parallel velocity of $2\overline{v}_\|$.

The important quantity is the relative speed between the scattering background particles and the given scattered particle. We first calculate this relative speed by choosing the scattered particles' direction of travel as the polar axis and finding the square of the average relative velocity between the scattered particle (of speed v_o) and the background particles (of speed $\overline{v}$ and random orietnation). The coordinate system is shown in Figure 13. When averaged over all angles, we find that the average relative speed is given by $v_r = \sqrt{\overline{v}^2 + v_o^2}$.
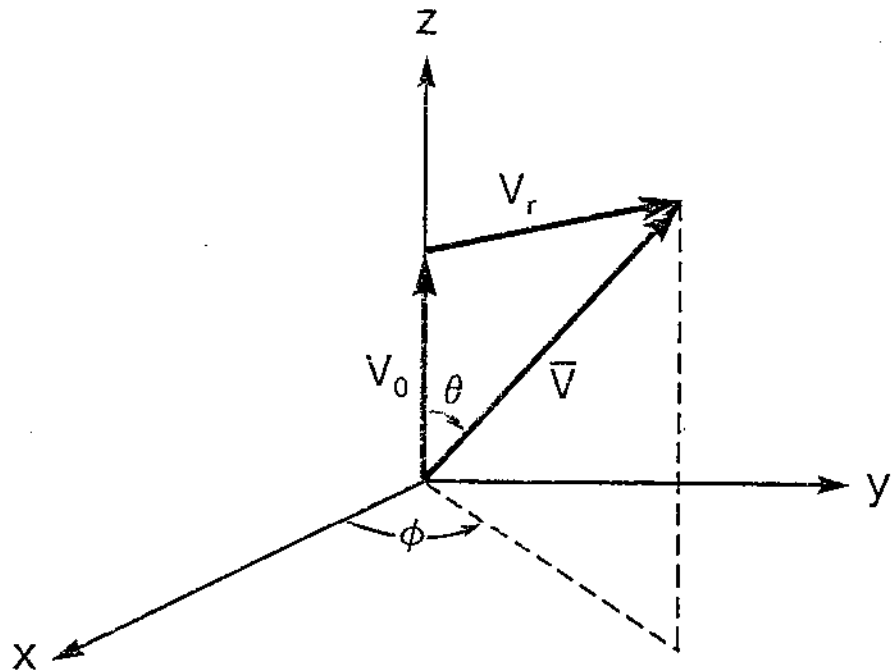
Figure 13. The coordinate system used to calculate the average relative speed, $(1/4\pi)\int d\Omega \, |\vec{v}_r|$, between a particle with speed v_o and background of particles uniformly distributed in velocity space with thermal speed $\bar{v} = 3T/m.$

The ratio of the energetic tail relaxation rate to the bulk rate is then roughly estimated as

$$\frac{\nu_t}{\nu_\perp} \sim \frac{(\overline{v}^2 + \overline{v}^2)^{3/2}}{(\overline{v}^2 + 2\overline{v}^2)^{3/2}} = \frac{(3T + 3T)^{3/2}}{(3T + 6T)^{3/2}} = 0.54 \qquad (4.B.5)$$

The data displayed in Figure 5 yield exponential relaxation rates $\nu_\perp \simeq 146$ sec and $\nu_t \simeq 90$ sec^{-1}, which gives a ratio of 0.61 - reasonably close to the estimated ratio considering the rough approximations used.

We wish to compare our measured rates with the predictions of the theory of Ichimaru and Rosenbluth. Their predicted rates are calculated over the entire (Maxwellian) distribution of $v_\parallel$ and $v_\perp$. We therefore compare with theory only the relaxation rates which result from analysis of $\langle E_\perp(t) \rangle$ evolution. The $T_{\parallel \varepsilon}(t)$ evolution data is used only to display the overall relaxation to a common equilibrium, as in Figure 5.

In Figure 14 we plot the simply derived rates (all measured at $B_z = 281$ Gauss) against the $(n/T_f^{3/2}) \ln \Lambda_e$ scaling expected from any rate which at root depends upon the basic electron-electron collision rate given by (4.B.3) and (4.B.4) plus the M-J-T approximation. For comparison purposes, the predicted rate of Ichimaru-Rosenbluth in the limit of small anisotropy (2.D.10) is plotted as the solid line. The two different types of anisotropies have different symbols. Open
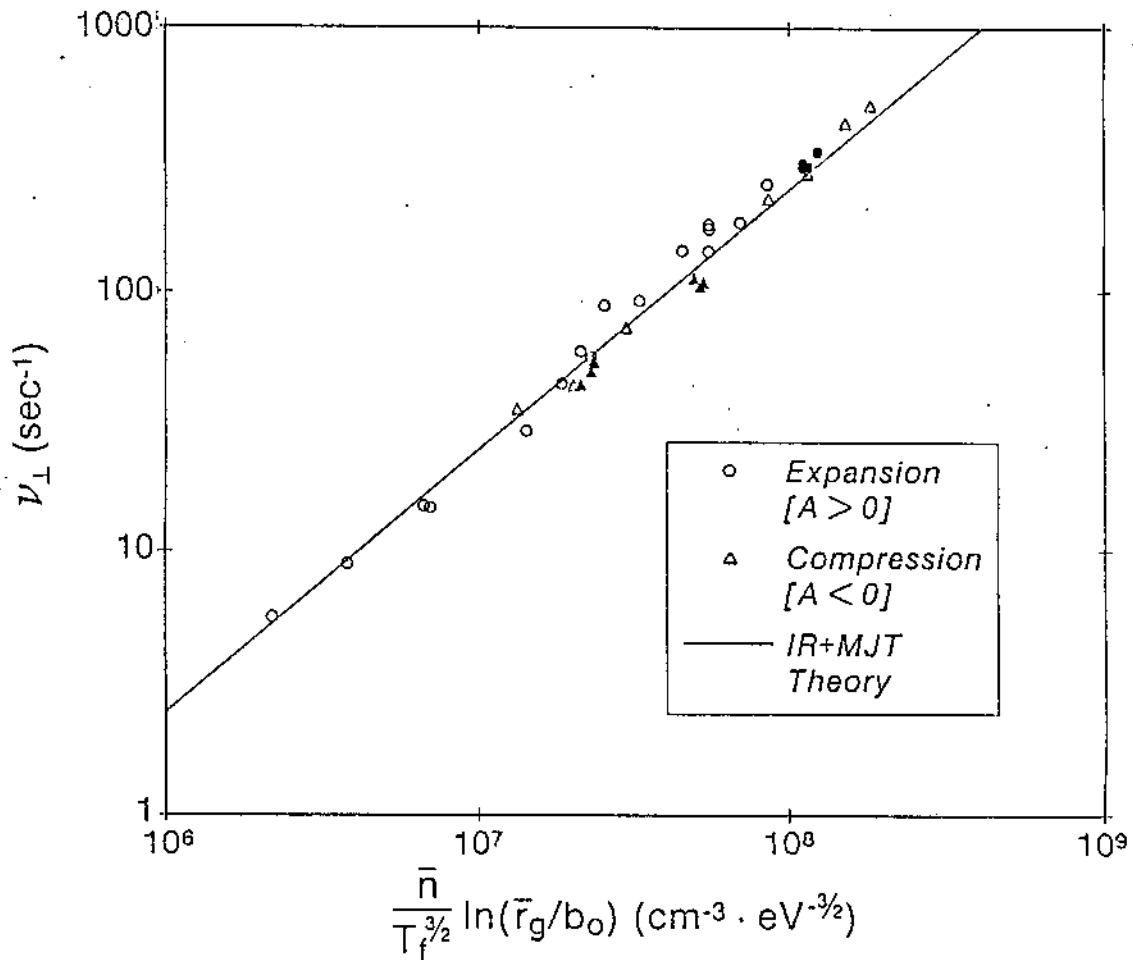
Figure 14. A plot of relaxation rates analyzed using a simple exponential model. The x-axis is the theoretically expected scaling of the relaxation rate: $\nu_\perp \propto \bar{n} \ln \Lambda_e / T_f^{3/2}$. A is the anisotropy parameter; $A \equiv T_\perp / T_\parallel - 1$. Open symbols have statistical errors of $\sim 15\%$, solid symbols $\sim 3\%$. The solid line is the absolute prediction of I-R with the M-J-T approximation in the limit of vanishing anisotropy.

symbols have estimated relative errors of about 15%, solid symbols about 3%.

We plot the data in Figure 14 using an average density, $\bar{n}$, in order to account for plasma end effects. The measured rates are derived from the evolution of the average perpendicular energy of all electrons along magnetic field lines at $r = 0$. The density along the field lines is not constant, at least in the end sheaths. The measured rates are then an axial average over rates at all axial positions. For comparison with theory, we assume the anisotropy remains independent of the axial coordinate, z, and compute an average density as:

$$\bar{n}(0) = \int_{\text{all } z} n(0, z)\, n(0, z)\, dz \Big/ \int_{\text{all } z} n(0, z)\, dz \, . \quad (4.B.5)$$

This average is essentially the average density in the vicinity of each electron. Using this averaging method is valid when the two velocity distributions are constant in z; this seems reasonable as long as the electron axial bounce frequency is very much larger than the collision rate. Equivalently, one can think of (4.B.5) as an axial average over collision frequencies when temperature is independent of axial position. This average density, $\bar{n}(0)$, is generally about 1-10% less than the central density $n(0,0)$, depending upon the plasma length and temperature.

93

C. Data Analysis Using the Ichimaru-Rosenbluth Rate Equation

In this section we show the relaxation predicted by I-R is approximately exponential, with the instantaneous rate only weakly dependent upon the value of a suitably parameterized anisotropy. The predicted behavior is then used as a model, which is least-squares fitted to the relaxation data. One of the fit parameters of this model is shown to be the relaxation rate in the limit of vanishing anisotropy. Rates measured with this model are then compared with the predicted rates of I-R.

The finite anisotropy evolution data is more properly compared with the theoretical prediction of that evolution when the data is reduced using the theoretical model of evolution. Strictly speaking, the I-R prediction of the evolution of a temperature anisotropy characterized by $T_{\parallel} \neq T_{\perp}$ was calculated only for Maxwellian $v_{\parallel}$ and $v_{\perp}$ distributions. The rate prediction of I-R is not self-consistent in the sense that it assumes the distributions will stay Maxwellian as the relaxation proceeds. Properly speaking, I-R calculate a prediction of the instantaneous rate presuming the distributions are Maxwellian.

If we assume that the distributions remain Maxwellian during the relaxation, then we can use the instantaneous rate prediction of I-R to describe the entire relaxation process. We believe that the actual experimental conditions are such as to make the approximation $\langle E_{\perp}(t) \rangle \simeq T_{\perp}(t)$ (i.e., the distributions remain Maxwellian) a

94

reasonably good one. First, the anisotropy starts off with essentially two Maxwellians that are not radically far from equilibrium (the initial anisotropy is not large). Second, thermal energy is essentially conserved during the relaxation. This implies that there is no external source or sink of energy which could locally disturb the distribution. Third, we believe there is no important collective process (waves) which is transferring energy via resonant electrons between the two distributions (see section D). This lack of resonance effects implies that there are no peaks or valleys generated in the distributions, and that the collisional process dominates the relaxation. Finally, since the electron-electron collision frequency is a smoothly decreasing function of speed ($\propto v^{-3}$), we expect that the initial Maxwellian will smoothly deform in time until equilibrium is reached. During this deformation the shape of the distribution should then be reasonably close to an intermediate Maxwellian characterized by a temperature $T_{\perp}(t) = \langle E_{\perp}(t) \rangle$. We therefore assume $\langle E_{\perp}(t) \rangle = T_{\perp}(t)$ is essentially Maxwellian for comparison purposes.

(There exists a method which could, in principle, experimentally verify the assumption of the distributions remaining nearly Maxwellian during the relaxation by measuring the $v_{\perp}$ distribution. It is discussed in Appendix E. At the present time, its development as a measurement of the $v_{\perp}$ distribution function is insufficient to allow an experimental verification of the assumption. The problem is

basically one of noise (fluctuations); the recent advent of the "noise killer" technique may allow further progress on this measurement.)

We deduce that to good approximation the thermal energy is a constant during the relaxation, i.e.

$$\frac{1}{3} T_{\parallel}(t) + \frac{2}{3} T_{\perp}(t) = T_f \quad . \qquad (4.\,C.\,1)$$

This deduction is based upon the measured constancy of $\langle E_{\perp}(t) \rangle$ and $T_{\parallel e}(t)$ after equilibration. For example, see the right side of Figure 5. The data from which Figure 5 was plotted extends in time for another order of magnitude. Analysis of this behavior yields an external thermal input source of approximately 10^{-4} eV/msec/el. This gives a correction to the simply analyzed relaxation rate that is less than 1%, and we neglect it. All rates are analyzed with the assumption (4.C.1).

We therefore use the constant energy form of the Ichimaru-Rosenbluth anisotropic rate equation written in terms of the measured quantities $\langle E_{\perp}(t) \rangle \equiv T_{\perp}(t)$, T_f, $\bar{n}(0) \equiv \bar{n}$, and B_z as our model of relaxation:

$$\frac{d}{dt} (T_{\perp} - T_f) = -\nu_{\perp}(T_{\perp}, T_f, B_z, \bar{n})(T_{\perp} - T_f) . \qquad (4.\,C.\,2)$$

Here

$$\nu_{\perp}(T_{\perp}, T_f, B_z, \bar{n}) = \frac{8}{5} \left(\frac{\pi}{m_e} \right)^{1/2} \frac{\bar{n} e^4 \ln \Lambda_e}{T_f^{3/2}} H(A) \qquad (4.\,C.\,3)$$

where $A = T_\perp/T_\parallel - 1$ is the parameterization of the anisotropy, which can be written as $A = 3(T_\perp - T_f)/(3T_f - 2T_\perp)$ under the constant energy assumption. $H(A)$ is given by (2.D.11). The modified Coulomb logarithm, $\ln \Lambda_e$, contains the B_z dependence as per the M-J-T approximation.

For convenience, we restate (2.D.11):

$$H(A) = \frac{15}{4} \frac{\left(\frac{2}{3}A + 1\right)^{3/2}}{A^2} \left[-3 + (A+3) \begin{cases} \tan^{-1}\sqrt{A}/\sqrt{A}; \ A > 0 \ \text{(expansion)} \\ \tanh^{-1}\sqrt{-A}/\sqrt{-A}; \ A < 0 \ \text{(compression)} \end{cases} \right]$$

$$(4.C.4)$$

Note that $H(A)$ behaves slightly differently for $T_\parallel < T_\perp$ $(A > 0)$ anisotropies than for $T_\parallel > T_\perp$ $(A < 0)$ anisotropies. In the limit of small anisotropy, $H(A) \to 1$ for both cases.

We restate equation (2.D.12):

$$\nu_{\perp o} \equiv \frac{8}{5}\left(\frac{\pi}{m_e}\right)^{1/2} \frac{\bar{n} e^4 \ln \Lambda}{T_f^{3/2}} \ ; \qquad (4.C.5)$$

and rewrite (4.C.2) as

$$\frac{d}{dt}(T_\perp - T_f) = -\nu_{\perp o} H(A)(T_\perp - T_f) . \qquad (4.C.6)$$

If $H(A)$ varies slowly enough as the finite anisotropy relaxes, then (4.C.6) indicates nearly exponential relaxation should be observed.

We use a computer to numerically integrate equation (4.C.6).
We first note that (4.C.6) can be written in terms of scaled variables
$\tau = \nu_{\perp o} t$ and $\mathcal{E} = (T_{\perp} - T_f)/T_f$, and rewrite (4.C.6) as

$$\frac{d\mathcal{E}}{d\tau} = -H \left(\frac{3\mathcal{E}}{1-2\mathcal{E}} \right) \mathcal{E} \qquad (4.C.7)$$

where $A = 3\mathcal{E}/(1-2\mathcal{E})$. Figure 15 shows a plot of the time evolution
of the logarithm of $|\mathcal{E}|$, for both compression and expansion anisot-
ropy cases, over a range which encompasses the largest experi-
mental anisotropies encountered in this study. The dashed line rep-
resents the evolution of $|\mathcal{E}|$ assuming $H(3\mathcal{E}/1-2\mathcal{E})$ is identically 1
(i.e., the evolution is purely exponential). The slope of $\log(|\mathcal{E}(\tau)|)$
at any τ is the instantaneous relaxation rate scaled to $\nu_{\perp o}$. As can
be seen from Figure 15, this rate does not change much over the
range of anisotropies measured, and therefore the relaxation is pre-
dicted by I-R to be nearly exponential.

We use the numerical solution to (4.C.7) as the model of relax-
ation written in scaled variables $\mathcal{E}, \tau$. The scaled time, τ, is given
by $\tau = \alpha t + \beta$. This parameterization of τ is completely analogous
to the parameterization used in the simple exponential model (4.B.1)
discussed in the previous section. The only differences between the
models are that the anisotropy is scaled in this model, and the expo-
nential function is replaced by a numerically generated function. The
value of the fitted parameter α gives $\nu_{\perp o}$, the measured relaxation
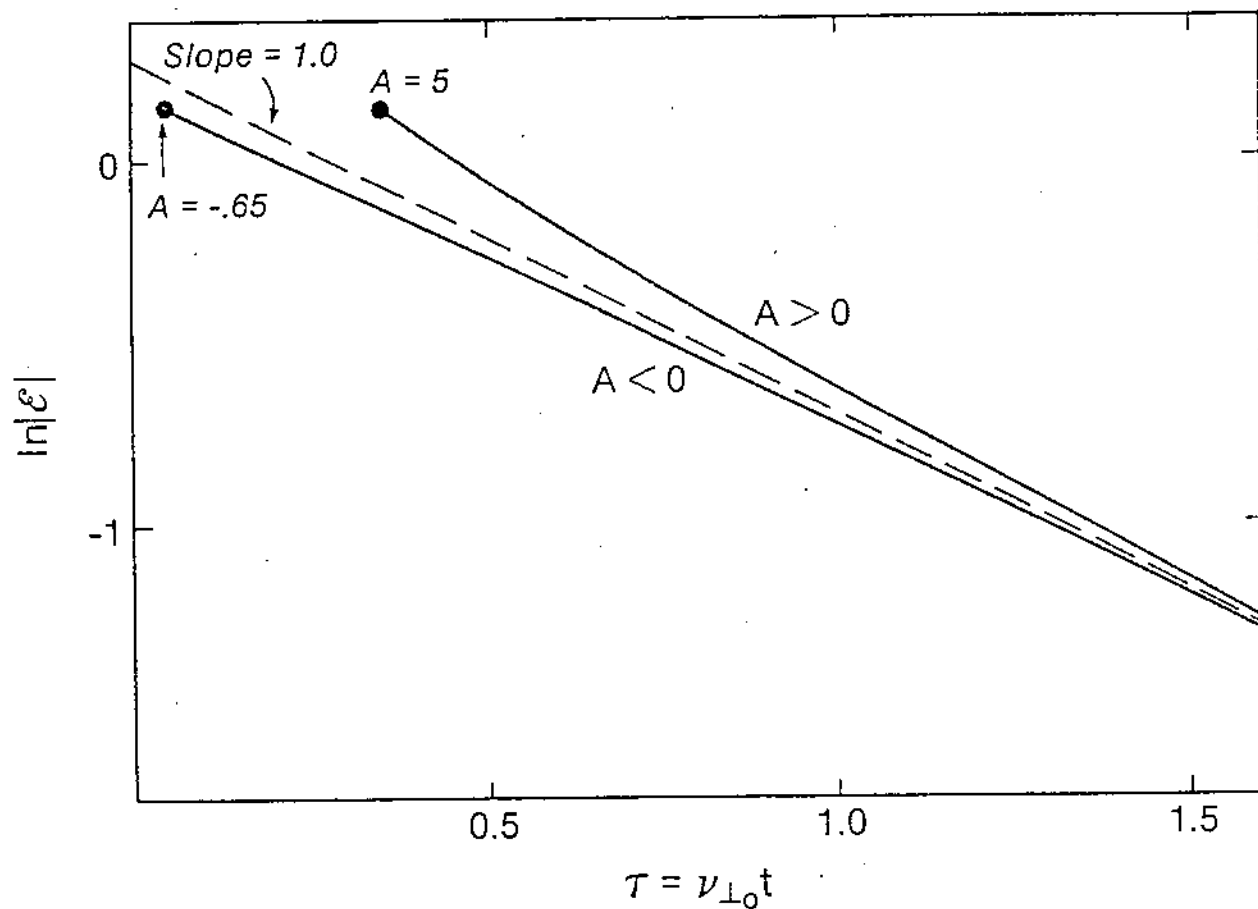
Figure 15. The predicted relaxation of the scaled energy $\mathcal{E} = (T_{\perp} - T_f)/T_f$ plotted as a function of scaled time $\tau = \nu_{\perp_0} t$. The relaxation of both positive and negative anisotropies are shown as solid lines. The dashed line represents pure exponential relaxation. The slope of the $\ln|\mathcal{E}|$ line at a given τ is the scaled instantaneous rate $\nu_{\perp}(r)/\nu_{\perp_0}$.

rate, for comparison with the theory prediction of I-R. Note that $\nu_{\perp o}$ is the relaxation rate in the limit of vanishing anisotropy; that is, $\nu_{\perp} \to \nu_{\perp o}$ in the limit $\mathcal{E} \to 0$.

A plot of the measured values of $\nu_{\perp o}$ is given in Figure 16. This figure represents the most important result of the investigation described in this dissertation. The measured values of $\nu_{\perp}$ are plotted against the expected scaling of rates predicted by the theory of I-R as modified by the M-J-T approximation. The plotted rates have members of both types of anisotropies: $A > 0$ (plotted as circles) and $A < 0$ (plotted as triangles). The characteristic errors of rates measured with the fluctuation reduction scheme (solid symbols) is about 3%; the others (open symbols) have errors of about 15%. The $\nu_{\perp o}$ prediction of the modified theory of I-R is given as the solid line; there are no adjustable parameters. It should be restated that the theoretical prediction is calculated using the "dominant term" approximation, which neglects terms of order $1/\ln \Lambda_e$. For these magnetized pure electron plasmas, $1/\ln \Lambda_e \sim 10\%$. Hence the theoretical prediction (the location of the solid line) is also uncertain to about 10%.

An error weighted least squares fit of the measured rates to a model that keeps the scaling of the modified I-R theory but allows the coefficient to vary, i.e. $\nu_{\perp o}^{fit} = \alpha \nu_{\perp o}^{I-R}$, gives $\alpha \simeq 0.95$ as the best fit value. This would give a line parallel to and only 5% below the solid line of Figure 16. This shows that the measured rates and the

100

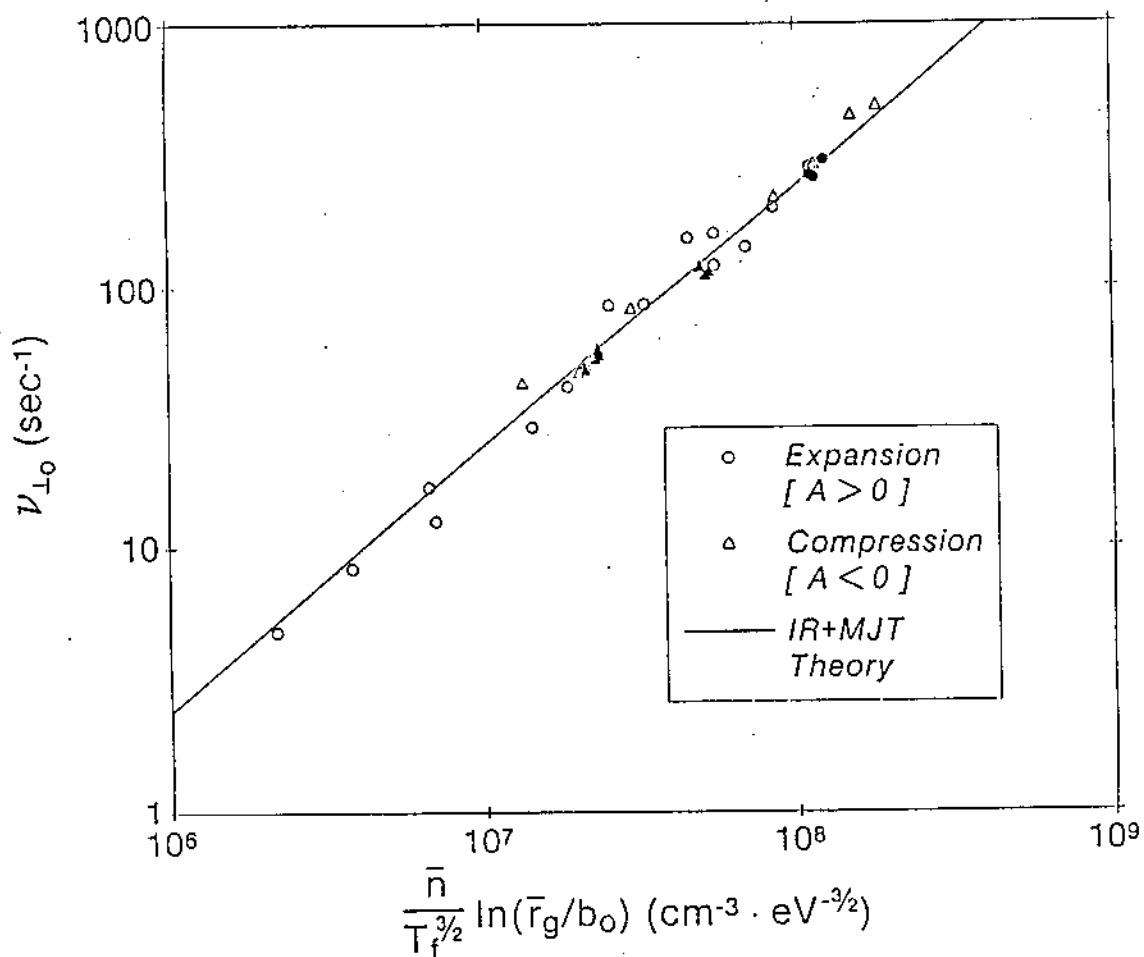Figure 16. Plot of fitted relaxation rates using the solution to the I-R rate equation as the model. The x-axis is the theoretical I-R rate scaling: $\nu_{\perp_o} \propto n \ln \Lambda_e / T_f^{3/2}$. A is the anisotropy parameter; $A = T_\perp / T_\parallel - 1$. Open symbols have ~15% error; solid symbols ~3%. The solid line is the absolute prediction of I-R with the M-J-T approximation in the limit of vanishing anisotropy.

absolute prediction of the modified theory of I-R agree to about 5%
over two decades of measured rates.

We can also plot these measured rates, appropriately scaled,
to display either the density or temperature scaling. Figure 17 shows
the rates multiplied by $T_f^{3/2} \ln \Lambda_e$ plotted against the measured dens-
ity n, and Figure 18 shows the rates divided by n $\ln \Lambda_e$ plotted
against the temperature dependence $T_f^{3/2}$. In both cases, the pre-
diction of Ichimaru-Rosenbluth is plotted as the solid line.

The measured rates unfortunately have too much scatter to
clearly delineate the logarithmic temperature dependence expected
from $\ln \Lambda_e$ ($\Lambda_e \propto T^{3/2}$). The dashed line of Figure 18 shows the
dependence the plotted data would take assuming there is no logarith-
mic temperature dependence. Since there is no theoretical prediction
which incorporates this assumption, the dashed curve was vertically
adjusted to coincide with the I-R prediction in the center of the data.
While the data does seem to better conform to the solid line, the data
is not good enough to exclude the dashed line as a correct model.

The question of whether or not the Montgomery-Joyce-Turner
approximation is valid can be somewhat more clearly answered by the
data, although the absence of B_z scaling data and the experimental
uncertainty in the data makes the affirmative indication less than com-
pelling. Figure 19 shows a plot of the measured rates vs the scaling
dependence of the weak field I-R theory (i.e., $\ln \Lambda = \ln \lambda_D / b_o$). The
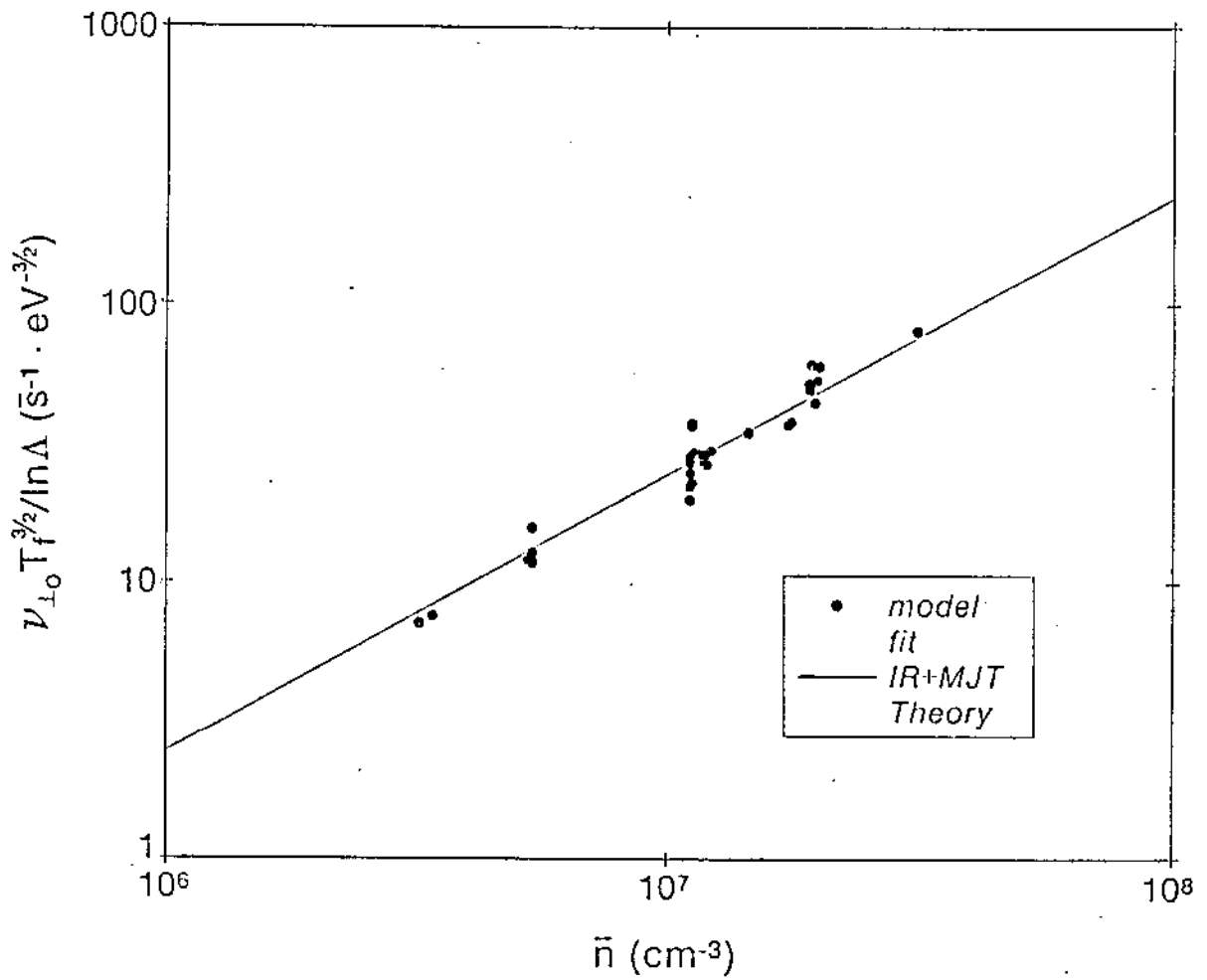
Figure 17. The measured rates are scaled by $T_f^{3/2}/\ln \Lambda_e$ and plotted against the measured density, $\bar{n}$. The theoretical prediction of I-R and M-J-T is the solid line.
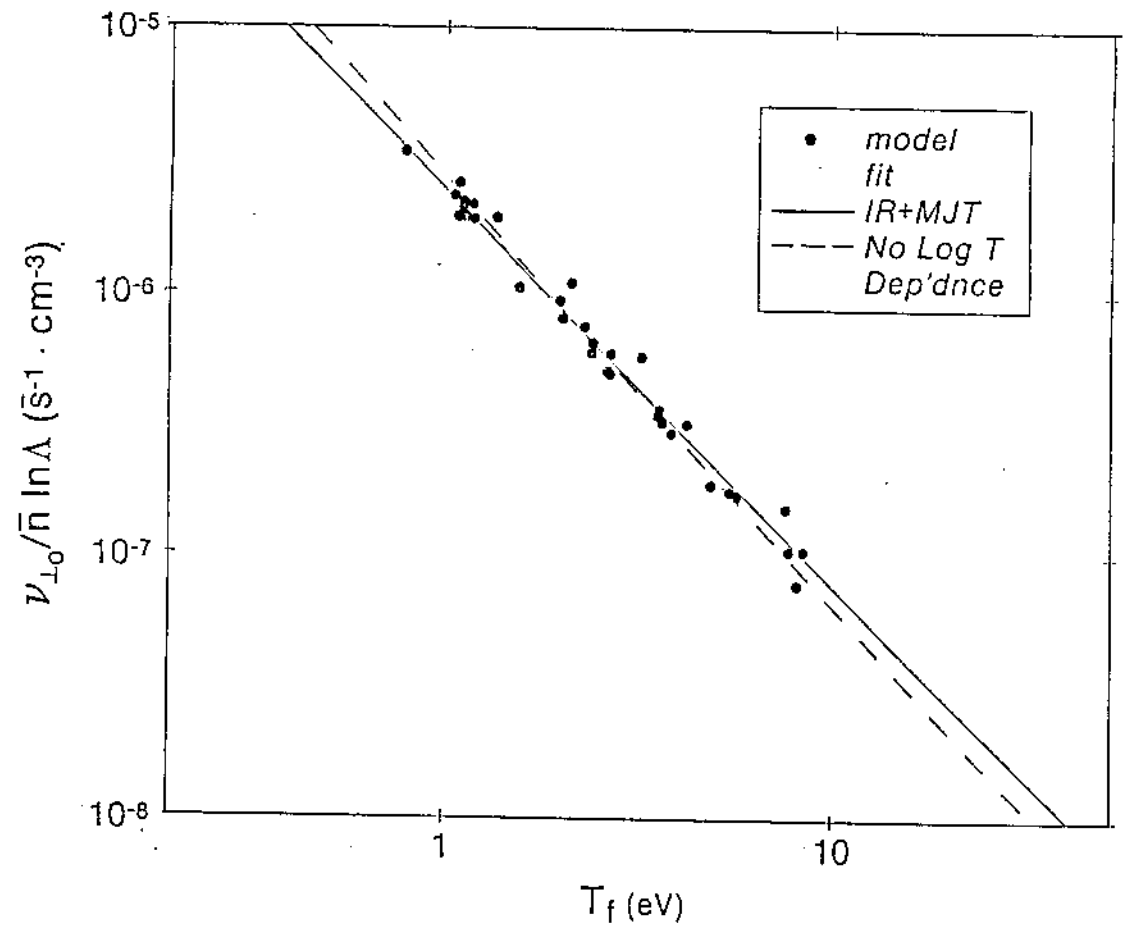
Figure 18. The measured rates are scaled by $(\bar{n} \ln \Lambda_e)^{-1}$ and plotted against the measured final equilibrium temperature, T_f. The absolute theoretical prediction of I-R and M-J-T is the solid line. The dashed line is the dependence the scaled rates would have if there was no $\ln(T_f^{3/2})$ dependence.

prediction of I-R is shown as the solid line. The prediction clearly lies above the measured data; the weighted best-fit line lies over 20% below the prediction.

Given that both the theoretical prediction of I-R and the best-fit line have uncertainties of the order of 10%, the indication of Figure 19 does not rule out $\ln \Lambda = \ln \lambda_D/b_o$. Since the separation between rate predictions using the $\Lambda_e = \bar{r}_g/b_o$ and $\Lambda = \lambda_D/b_o$ approximations for this plasma is only in the range of 20% or so, a clear delineation could be made only by demonstrating the logarithmic scaling of B_z. The EV device has a usable magnetic field that can be varied by about a factor of 5. This means a total deviation in rates of about 15% from the highest field to the lowest. Inasmuch as the fluctuation reduction technique doesn't seem to work as well at the lower fields, measuring this 15% deviation in the EV device will probably require a large number of measured rates for statistical analysis. (This is the same order of difficulty as delineating between the solid and dashed lines of Figure 18.) As of now, the best that can be said is that the M-J-T approximation in the magnetized regime ($\bar{r}_g \ll \lambda_D$) is indicated by our measured rates, but is not proven.

D. Sources and Estimates of Systematic Errors

There are several candidates for systematic error sources in the measurement of the anisotropic temperature relaxation rate and the comparison of those measured rates with theory. Setting
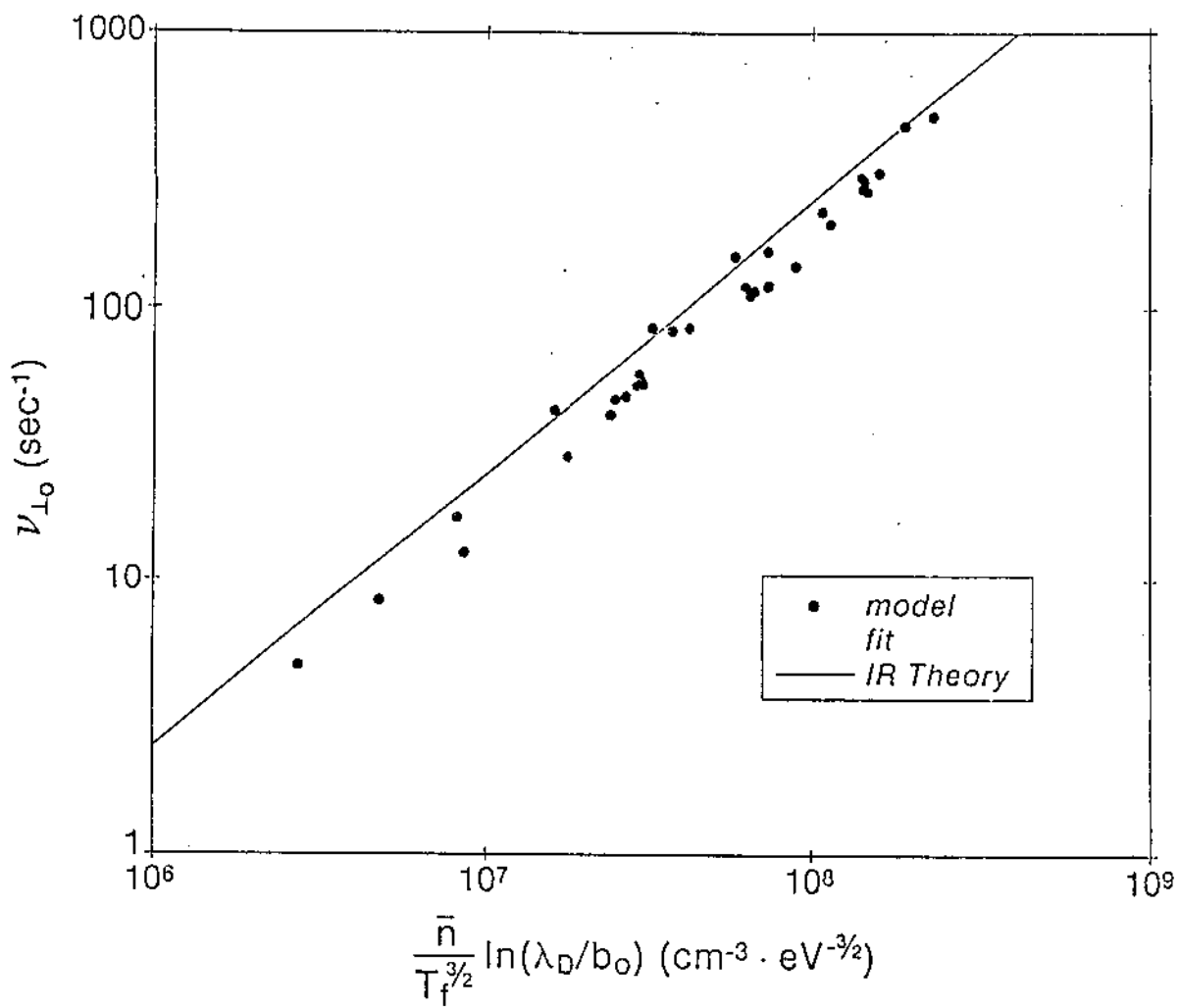
Figure 19. Measured rates $\nu_{\perp_0}$ plotted against the weak magnetic field rate calculation of I-R. The solid line is the absolute prediction of I-R in the weak field regime.

$\frac{d}{dt} T_f = 0$ (the constant thermal energy assumption) during the relaxation, for instance, is a deduction based upon some measured rates of change of T_f after equilibration. These rates all give $\dot{T}_f \sim 10^{-4}$ eV/msec, which would result in less than a 1% error in measured rates. However, $\dot{T}_f$ could conceivably be different during the relaxation. Linear systematic errors in the measurements of $\langle E_\perp \rangle$ and $\bar{n}$ (i.e., error proportional to $\langle E_\perp \rangle$ and n) wouldn't necessarily change the value of the measured rates, but would affect the comparison between experiment and theory. Both the density and temperature measurements are believed to be better than 5%.

Another neglected effect that could affect the measured rate is electron-neutral collisions. Such collisions can exchange parallel energy with perpendicular. We estimate the electron-neutral collision rate of using the simple rate equation

$$\nu_{e-n} \simeq \sigma n_n \bar{v}_e \qquad (4. D. 1)$$

where $\sigma \simeq 10^{-15}$ cm^2 is the approximate neutral cross-section, n_n is the neutral density in EV at pressures of 10^{-10} Torr ($n_n \simeq 3.3 \times 10^6$ neutrals/cc), and v_e is the electron thermal speed (the room temperature neutrals are essentially at rest). This crude model gives $\nu_{e-n} \sim 0.1$-1.0 sec^{-1}, increasing with the electron temperature, and thus electron-neutral collisions could give significant corrections to the measured rates only for those few rates measured

at the lower left of Figure 16. For most of the rates measured this effect should contribute less than 1%.

Collective effects could also affect the measured rates by providing alternate routes to equilibrium. The free energy associated with $T_\perp > T_\parallel$, for instance, could drive a collective instability which, in turn, could release the energy of the instability back into the parallel motion via resonant electrons.

Instabilities driven by features of the particle distribution in velocity space are often termed microinstabilities. Microinstabilities can be major sources of velocity space transport in magnetic mirror confinement devices. However, most of the microinstability problems associated with magnetic mirror devices are driven by peculiar velocity space distributions not usually found in electrostatic confinement devices such as EV. This peculiar distribution is characterized by a lack of low $v_\perp$ particles (due to the loss cone of the mirror). The relative abundance of high perpendicular energy particles gives a system with a lot of available free energy. The electrostatic confinement of EV has no similar loss cone.

Some of the microinstabilities associated with velocity space anisotropies have been treated by Davidson[59] in the linear approximation. Most are not applicable to the EV plasma for the reason given above, i.e. $\partial f(v_\perp)/\partial v_\perp^2 \leq 0$ throughout the relaxation. The three different cases which might apply are all found to predict suppression of instability rather than growth.

108

The first case is the electromagnetic Whistler (also known as the electron cyclotron) instability. Suppression of this instability is predicted for any reasonable anisotropy $T_\perp > T_\parallel$, due basically to the fact that $\omega_p^2 \ll \Omega^2$ for any plasma studied in EV. The second case, called the electrostatic ordinary mode instability, is suppressed by the low $\beta \equiv 8\pi nT/B_z^2$ of the studied plasmas. The third case, called the Weibel instability, is suppressed by the finite length and the low densities of the plasmas studied, at least for any reasonable $T_\perp > T_\parallel$. There could, of course, be other linear instabilities, as well as non-linear ones, which are present in the EV plasma during relaxation.

We believe that there is no significant enhancement of our measured rates due to instabilities. Our argument is a simple one, although it is not definitive. Our measured rates include both types of anisotropy, $T_\perp >$ and $< T_\parallel$. Each of the cases of instabilities studied above predict growth of only one or the other type of anisotropy (the 0-mode case can only go for $T_\parallel > T_\perp$). We argue that this holds true for any relevant instability. In that case, we would expect Figure 16 to show a marked deviation between expansion and compression generated rates at any given value of $n \ln \Lambda_e / T_f^{3/2}$. None are seen, which argues against rates contaminated by instability.

Any collective instability which is capable of changing $\mu = v_\perp^2/B$, the gyromotion adiabatic invariant, must have a frequency on the order

of Ω_c or higher. EV was not designed for diagnostics in this range ($\Omega_c \sim 1$ GHz), and the experimental evidence argued against expending the considerable effort that would be required to measure such phenomena with precision. From the evidence of Figure 16, we estimate that instability constitutes a systematic error source of 5% or less in the comparison between experiment and theory.

The last possibility considered as a source of systematic error was discussed in section C. This is the deviation of the two distributions from their respective Maxwellians $T_\perp$ and $T_\parallel$. We consider this deviation to be the most likely source of systematic error in the comparison between experiment and theory. Although it is difficult to estimate the magnitude of this error, we can make a very rough estimate of that magnitude. We note that $\nu_{\perp o}$ is the rate when $T_\parallel = T_\perp$, and that in theory the instantaneous rate, $\nu_\perp$, displays at most a 30%-40% deviation from $\nu_{\perp o}$ when the two temperatures differ by a factor of 6 (A = +5 or -5/6). This suggests that $\nu_{\perp o}$ is fairly insensitive to deviations of the entire velocity distribution from a Maxwellian of temperature T_f. Anisotropies of $A \simeq +5$ or -5/6 are typical of the initial stages of the relaxation where the distributions are approximately Maxwellian. We would expect the distributions to have the greatest deviation from Maxwellian form at about one collision time into the relaxation process. Figure 15 shows the deviation of $\nu_\perp$ from $\nu_{\perp o}$ to be about 10% at that time, and we expect the deviation of

the actual distributions from Maxwellian to change $\nu_\perp$ by at most the same percentage. We thus estimate the deviation of the measured $\nu_{\perp o}$ (measured from all values of $\nu_\perp$ during the relaxation) from the ideal $\nu_{\perp o}$ (as would be measured if the distributions remain Maxwellian) to be at most about 10%. We thus estimate the overall systematic error in our comparison between experiment and theory to be on the order of 10%. This is the same order of error as that given by the statistical (random) measurement error of the best-fit line to the measured rates.

V. Summary of Results and Conclusions

A. Summary of Results

This section is a summary of the important results of this investigation into anisotropic temperature relaxation in a magnetized pure electron plasma. A finite temperature anisotropy can easily be initially induced in the plasma by an axial compression or expansion that is approximately one dimensional. The initial anisotropy is described by two approximately Maxwellian electron velocity distribution functions which have different temperatures $T_\perp \neq T_{||}$. The magnetic field direction provides the parallel axis reference.

The initial anisotropy and its subsequent relaxation to equilibrium are measured on the plasma axis (where radial density and temperature gradients are small) by a technique which measures $\langle E_\perp \rangle$, the average energy of the perpendicular velocity distribution, for all electrons on the axis as a function of time. For comparison to theory, $\langle E_\perp \rangle$ is assumed to be the perpendicular temperature; that is, the perpendicular velocity distribution is assumed to be always Maxwellian during the relaxation.

The relaxation is shown to take place under conditions of nearly constant density and thermal energy. Hence the measured anisotropy can be characterized by the difference between $\langle E_\perp \rangle$ and the final equilibrium temperature, T_f. A typical initial anisotropy is graphically shown to relax approximately exponentially in Figure 5,

which plots $\langle E_\perp \rangle$ measurements as functions of time.

Also plotted in Figure 5 are $T_{\|\varepsilon}$ measurements. The $T_{\|\varepsilon}$ data also display the exponential decay of the anisotropy (here defined as $T_{\|\varepsilon} - T_f$), but this decay has a longer time scale than that of the $\langle E_\perp \rangle$ data. The different rates of relaxation for the $\langle E_\perp \rangle$ and $T_{\|\varepsilon}$ measurements of the same anisotropy are explained by the fact that the $T_{\|\varepsilon}$ measurement only measures the temperature of the energetic tail of the parallel velocity distribution. These more energetic tail electrons have a smaller average frequency of collisions with an average thermal electron, due to the (energy)$^{-2}$ dependence of the Coulomb cross-section. Thus the relaxation of the energetic tail electrons measured from $T_{\|\varepsilon}$ data is expected to display a slower rate than the relaxation of the entire distribution measured from $\langle E_\perp \rangle$ data. The difference in the two measured rates is shown to be in approximate accord with a simple collisional estimate of those two rates.

For comparison with theory, the relaxation rate is found from the measured $\langle E_\perp \rangle$ data by using the I-R theoretical prediction of that relaxation as a model, which is least-squares fit to the data to yield the measured rate. The relaxation rate is measured in this manner from relaxations of anisotropies initiated by both compression ($\langle E_\perp \rangle - T_f \leq 0$) and expansion ($\langle E_\perp \rangle - T_f \geq 0$) in plasmas of varying densities and final equilibrium temperatures. These rates are plotted

113

in Figure 16 against the theoretical scaling ($n \ln \Lambda_e / T_f^{3/2}$) predicted by I-R using the M-J-T approximation which allows the prediction of I-R to be used in the strongly magnetized regime. The measured rates statistically agree with the absolute theoretical prediction (there are no adjustable parameters; all variables are measured) to about 5%. The solid line plotted in Figure 16 is the absolute theoretical prediction (see equations (2.D.9) to (2.D.12)). The rates are measured over two decades in the expected parameter scaling. Both the density and final equilibrium temperature are individually varied over one decade.

The rates are also plotted in Figures 17 and 18 to show scaling with density and equilibrium temperature, respectively. The theoretical prediction of I-R plus M-J-T is plotted as the solid line in each figure. The dashed line of Figure 18 is the path the data would be expected to follow if there was no logarithmic temperature dependence. Although the data does seem to fit the solid line slightly better than the dashed line, statistically the dashed line dependence cannot be ruled out.

Finally, the data are compared with the weak field theory of I-R; i.e. the Coulomb logarithm ($\ln \Lambda$) is used instead of the M-J-T approximation ($\ln \Lambda_e$). A plot of the measured rates against this theoretical scaling ($n \ln \Lambda / T_f^{3/2}$) is given in Figure 19. The solid line is the absolute prediction of the theory. The data clearly lie below

the prediction, and in fact, the data statistically give a value which is over 20% below the prediction.

Estimates of the uncertainties in the measurements and the theory must be made before conclusions may be drawn from the comparison between experiment and theory. The rate prediction of I-R is calculated using Chandrasekhar's "dominant term" approximation, in which terms of relative order $(1/\ln \Lambda)$ are neglected. The M-J-T approximation $(\ln \Lambda \to \ln \Lambda_e)$ is then applied to the I-R rate calculation, and for our experiments $1/\ln \Lambda \sim 1/\ln \Lambda_e \sim 10\%$. Thus a more rigorous calculation of the theoretical rate may result in a change in the value of the rate prediction which is on the order of 10%.

The statistical nature of the measured rates is such that any best-fit line to the data is statistically accurate only to about 10%. The absolute prediction of I-R + M-J-T (see Figure 16) falls within this range, while the absolute prediction of I-R alone (see Figure 19) does not. There is also the possibility of systematic error, which is estimated to be at most on the order of 10%.

B. Conclusions

Our conclusions address two questions. The first, and most important, is whether or not the anisotropic temperature relaxation rate calculation of Ichimaru and Rosenbluth as modified by the approximation of Montgomery, Joyce and Turner correctly predicts the values of those rates measured in a magnetized electron plasma. The

excellent statistical agreement between the absolute prediction and the measured rates (to about 5%) over two decades leads unequivocally to the conclusion that the I-R + M-J-T calculation does indeed correctly predict the rate of relaxation. Agreement to 5% is remarkable, considering the number of approximations involved in the rate calculation (and in the general theory from which it is calculated), and considering the rates are measured from the relaxation of anisotropies which are only approximately Maxwellian.

The second question is whether or not the data is statistically accurate enough to verify the M-J-T approximation. A more rigorous rate calculation (one in which the dominant term approximation is not employed) could possibly lower the rate prediction of I-R by an amount on the order of 10%. This would bring the prediction into the range of statistical agreement with the data without requiring the M-J-T approximation. Thus we conclude that the data can neither conclusively verify nor reject the M-J-T approximation, although the data strongly supports the validity of the approximation.

References

1. J. R. Hiskes and A. H. Futch, Nucl. Fusion 14, 116 (1974).

2. R. J. Burke and R. F. Post, Phys. Fluids 17, 1422 (1974).

3. Lin et al., J. Appl. Phys. 26, 95 (1955); F. L. Mohler, Bur. Stand. J. Res. 21, 873 (1938).

4. L. Spitzer and R. Härm, Phys. Rev. 89, 977 (1953).

5. S. Ichimaru and M. N. Rosenbluth, Phys. Fluids 13, 2778 (1970).

6. S. Ichimaru, "Basic Principles of Plasma Physics (W. A. Benjamin, 1973), chs. 9 and 10.

7. D. Montomgery, L. Turner and G. Joyce, Phys. Fluids 17, 954 (1974).

8. D. Montgomery, G. Joyce and L. Turner, Phys. Fluids 17, 2201 (1974).

9. A. Einstein, Add. d Physik 17, 549 (1904); 19, 371 (1906).

10. L. Boltzmann, Wein. Ber. 66, 275 (1872).

11. S. Chapman and D. Cowling, "The Mathematical Theory of Non-Uniform Gases" (Cambridge Univ. Press, 1939). Comparison between theory and experiment is made in chapters 12-14.

12. E. Persico, Monthly Notices, R.A.S. 86, 93 (1926).

13. R. S. Cohen, L. Spitzer and P. McR. Routly, Phys. Rev. 80, 230 (1950).

14. S. Chandrasekhar, "Plasma Physics" (Univ. of Chicago Press, 1960), ch. 7.

15. L. D. Landau, Physic. Z. Sowjet. 10, 154 (1936).

16. D. C. Montgomery and D. A. Tidman, "Plasma Kinetic Theory" (McGraw-Hill, 1964).

17. M. N. Rosenbluth, W. M. McDonald and D. L. Judd, Phys. Rev. 107, 1 (1957).

18. S. Chandrasekhar, Rev. Mod. Phys. 15, 1 (1943).

19. S. Chandrasekhar, Astro. J. 97, 255, 263 (1943).

20. Gobor, Proc. Roy. Soc. A213, 73 (1952).

21. S. Gasiorowicz, M. Neuman and R. J. Riddell, Phys. Rev. 101, 922 (1956).

22. W. B. Thompson and J. Hubbard, Rev. Mod. Phys. 32, 714 (1960).

23. J. Hubbard, Proc. Roy. Soc. A260, 114 (1961).

24. R. Balescu, Phys. Fluids 3, 52 (1960).

25. A. Lenard, Ann. Phys. (N.Y.) 10, 390 (1960).

26. N. Rostoker and M. N. Rosenbluth, Phys. Fluids 3, 1 (1960).

27. N. Rostoker, Phys. Fluids 3, 922 (1960).

28. C. F. Kennel and F. Englemann, Phys. Fluids 9, 2377 (1966).

29. K. Matsuda, Phys. Fluids 26, 1247 (1983).

30. S. Chandrasekhar, "Principles of Stellar Dynamics" (Univ. of Chicago Press, 1942), ch. 2.

31. D. L. Book, ed., "NRL Plasma Formulary," pg. 33 (1983), revised.

32. L. Spitzer, Monthly Notices R.A.S. 100, 396 (1940).

33. L. Spitzer, "Physics of Fully Ionized Gases" (Wiley, 1962), ch. 5.

34. L. D. Landau and E. M. Lifshitz, "Course in Theoretical Physics," Vol. 1 (Pergamon, 1976), pp. 154-167.

35. P. Hjorth, to be published.

36. T. B. Kaiser, Phys. Fluids 22, 593 (1979).

37. K. Matsuda, Phys. Fluids 26, 1508 (1983).

38. J. H. Malmberg and J. S. deGrassie, Phys. Rev. Lett. 35, 577 (1975).

39. J. H. Malmberg and T. M. O'Neil, Phys. Rev. Lett. 39, 1333 (1977).

40. T. M. O'Neil, Comments Plasma Phys. Cont. Fusion 5, 231 (1980).

41. T. M. O'Neil, Phys. Fluids 23, 2216 (1980).

42. R. C. Davidson, "Theory of Non-Neutral Plasmas" (W. A. Benjamin, 1974), pg. 107.

43. T. M. O'Neil and C. F. Driscoll, Phys. Fluids 22, 266 (1979).

44. S. A. Prasad and T. M. O'Neil, Phys. Fluids 22, 278 (1979).

45. C. F. Driscoll, J. H. Malmberg and K. S. Fine, submitted to Phys. Rev. Lett. (1987).

46. C. F. Driscoll, K. S. Fine, and J. H. Malmberg, Phys. Fluids 29, 205 (1986).

47. The $\ell = 1$ diocotron wave is the rotation of the column's center of mass, which is offset from the symmetry axis, about the symmetry axis. It can be initially present due to a small mis-alignment of the filament with the symmetry axis.

48. R. C. Davidson, "Theory of Non-Neutral Plasmas" (W. A. Benjamin, 1974), pp. 66-78.

49. J. deGrassie, Ph.D. thesis, pg. 56.

50. L. Brillouin, Phys. Rev. 67, 260 (1945).

51. R. C. Davidson, "Theory of Non-Neutral Plasmas" (W. A. Benjamin, 1974), pp. 4-7.

52. J. S. deGrassie, Ph.D. thesis, pg. 81.

53. Hsu and Hirshfield, Rev. Sci. Instrum. 47, 236 (1976).

54. D. E. Eggleston et al., to be published.

55.   B. R. Beck, private communication.

56.   R. C. Davidson, "Theory of Non-Neutral Plasmas" (W. A. Benjamin, 1974), pp. 66-73.

57.   K. Fine and C. F. Driscoll, private communication.

58.   S. Ichimaru, "Basic Principles of Plasma Physics" (W. A. Benjamin, 1973), pp. 3-4.

59.   R. C. Davidson, "Handbook of Plasma Physics," Vol. I, ch. 3.3 (pp. 521-585), ed. M. N. Rosenbluth and R. Z. Sagdeev (North Holland, 1983).

60.   F. Reif, "Fundamentals of Statistical and Thermal Physics" (McGraw-Hill, 1965), pp. 158-159.

61.   K. Fine, private communication.

APPENDIX A: 1-D Compression and Expansion

An essentially one dimensional compression is used to create a particular velocity space anisotropy from an initial Maxwellian equilibrium. This anisotropy is characterized by two different approximately Maxwellian distributions, $f(v_\parallel)$ and $h(v_\perp)$, which, in turn, are characterized by unequal temperatures $T_\parallel \neq T_\perp$. The parallel direction is along the magnetic field and confinement geometry symmetry axis. This unusual compression is made possible by exploiting the wide separation of two fundamental frequencies of the plasmas studied - the relatively large axial bounce frequency, ω_B, and the perpendicular and parallel energy exchange rate, $\nu_\perp$. In the plasmas studied, $\omega_B \sim$ 1 μsec and $\nu_\perp \sim$ 10 msec.

(i) Theory - a simple model

A very simple conceptual model is first used to describe a compression applied to an electron plasma which initially has an equilibrium Maxwellian velocity distribution, $F_i(v_\parallel, v_\perp)$

$$F_i(v_\parallel, v_\perp) = f_i(v_\parallel) h_i(v_\perp) = C_i \exp\left(-\frac{m(v_\parallel^2 + v_\perp^2)}{2T_i}\right), \qquad (A1)$$

where C_i is a normalization constant, and $T_i = T_{\parallel i} = T_{\perp i}$ in the initial equilibrium temperature. The following discussion refers to Figure 20. The electrons are initially trapped in cylinders L1 and L2 between two end plates held at potential V_0. All electrons are assumed
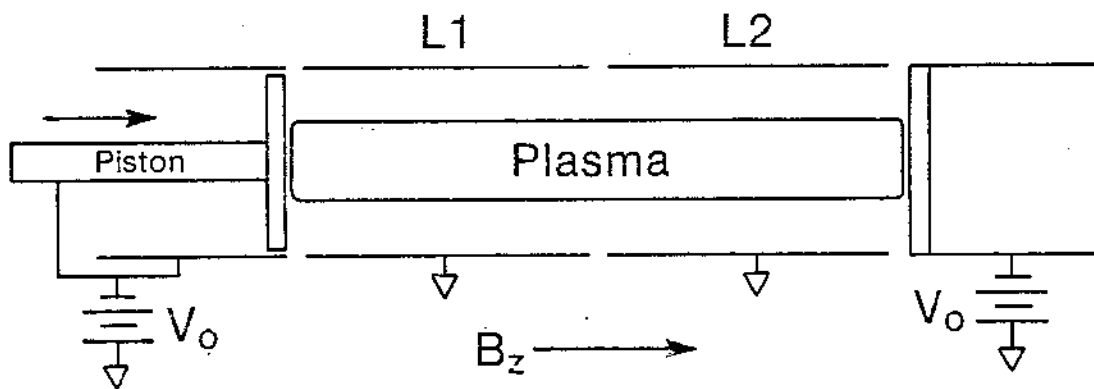
Figure 20. The movable plate on the left and the fixed plate on the right are held at potential V_o. The plasma length is assumed to be the separation between the plates.

to have their parallel motion exactly reflected by the plate potential at the plate face regardless of the magnitude of $v_{\|}$; the length of the plasma is then unambiguously given as the separation between the end plates. This approximation becomes more valid as the plasma length, L_p, to Debye length, λ_D, ratio increases. We can now ask how the electrons respond as L_p, which by assumption is the plate separation, is decreased from $L_p = (L_1 + L_2) \equiv L_i$ to $L_p = L_2 \equiv L_f$ by moving the piston towards the fixed plate. To further simplify the model, $v_\perp$ is assumed to be zero. All of the following discussion is equally valid for an expansion as well.

The bounce parallel motion of any electron can be thought of as an oscillator of frequency $\omega_B = \pi v_{\|}/L_p$, where $v_{\|}$ is the parallel speed. If the parameter L_p is changed slowly compared to ω^{-1}, then the axial bounce adiabatic invariant $\oint v_{\|} dz \equiv I_{\|}$ remains a constant during the change. For this simple system the integral is trivial; $I_{\|} = 2v_{\|}L_p$ at any point during the compression. By equating the values of $I_{\|}$ at the start and end of the compression, we find the ratio of final to initial velocities is $v_{\|f}/v_{\|i} = L_i/L_f$. Thus the parallel kinetic energy of the electron is changed by the ratio $\frac{1}{2}mv_{\|f}^2 / \frac{1}{2}mv_{\|i}^2 = (L_i/L_f)^2$. Since there are no collisions, $v_{\perp f} = v_{\perp i}$. Since all final parallel kinetic energies are scaled by the same factor, $L_i/L_f)^2$, the final velocity distribution is then

$$F_f(v_\parallel, v_\perp) = f_f(v_\parallel)\, h_f(v_\perp) = c_f \exp\left[-\frac{mv_\parallel^2}{2T_{\parallel f}} - \frac{mv_\perp^2}{2T_{\perp i}} \right] , \qquad \text{(A2)}$$

where

$$T_{\parallel f} = T_{\parallel i} \left(\frac{L_i}{L_f} \right)^2 \qquad \text{(A3)}$$

is the final parallel temperature and (L_i/L_f) is the compression ratio of initial to final plasma lengths. This model of compression then produces, to within the model approximations, an anisotropic velocity space distribution characterized by two Maxwellians of unequal temperature $T_\parallel \neq T_\perp$.

The temperature relationship (A3) can also be derived using thermodynamic arguments with an ideal gas approximation and the assumption of no collisions which transfer energy between the perpendicular and parallel degrees of freedom. An ideal gas which undergoes a quasistatic and adiabatic compression (adiabatic here means no heat transfer into or out of the gas) obeys the relationship[60]

$$V_f^{\gamma-1}\, T_f = V_i^{\gamma-1}\, T_i , \qquad \text{(A4)}$$

where V is the gas volume, and

$$\gamma = \frac{c_v + R}{c_v} , \qquad \text{(A5)}$$

where c_v is the molar specific heat at constant volume and R is the gas constant.

For an ideal gas, each degree of freedom adds $\frac{1}{2} R$ to c_v. The standard ideal gas then has $\gamma = 5/3$; there are three degrees of freedom. In the absence of any communication (collisions) between the perpendicular and parallel degrees of freedom, however, the parallel motions of the electrons can be thought of as the motions of a one-dimensional ideal gas. Then $\gamma = 3$, and (A4) becomes

$$(\pi A_{p_f} L_f)^2 T_f = (\pi A_{p_i} L_i)^2 T_i \qquad (A6)$$

which is identical to (A3), since A_p, the cross sectional area of the plasma, doesn't change.

(ii) Theory - a more complicated model

The above discussion misses any end effects associated with the Debye sheath at the plasma ends. The effect of a finite Debye sheath at the plasma ends will be considered in this section. The compression process will be assumed to preserve the axial bounce adiabatic invariant, but the details of the process will be left unspecified. A more realistic model of the compression process than the simple moving piston model will be considered in section (iv).

The following discussion refers to Figure 21. Consider the plasma to be initially confined in cylinders L_1 and L_2 with V_c, the potential applied to L_1, initially set to ground. L_2 is always grounded. The confinement gate potentials are fixed at V_0. The plasma is assumed to be in an equilibrium state; this means the
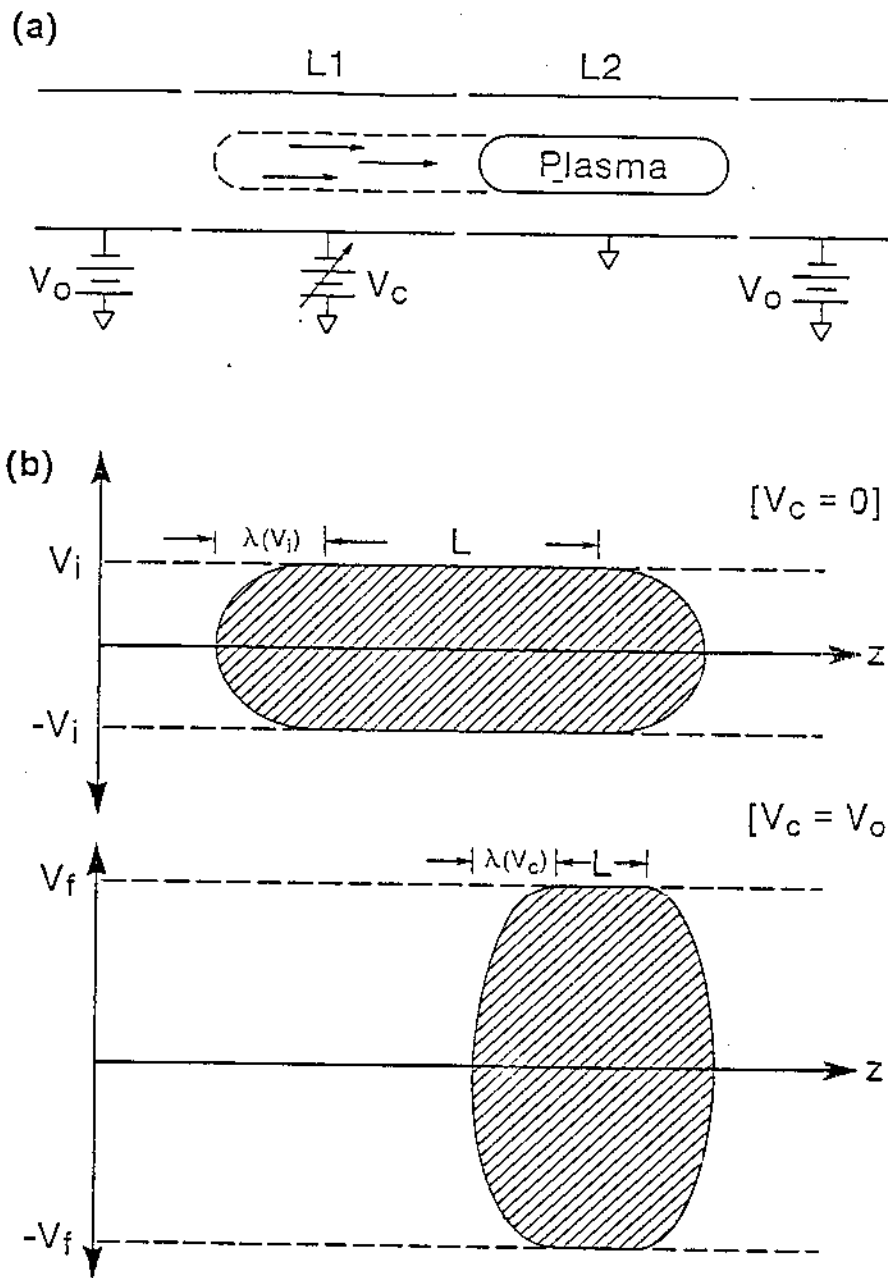
125

Figure 21. A 1-D compression is shown in (a); L1 and L2 are the
lengths of the two confining cylinders. Simple phase
space plots of the trajectory of a given electron when the
plasma is uncompressed and compressed are shown in (b),
along with the idealizations L, the length of the const
potential region, and $\lambda(v_i)$, the stopping distance. The
cross-hatched areas of both phase-space plots are equal,
since phase space volume is conserved for a 1-D com-
pression.

potential $\phi(r, z)$, is essentially constant in z except in the plasma end sheaths, where ϕ becomes more negative with a scale length of λ_D. V_c is then slowly lowered in such a way as to adiabatically compress the plasma into L_2 only; the compression is completed when $V_c = V_0$. There are assumed to be no collisions during the compress, and the axial bounce invariant, $I_{\parallel}$, is assumed to be preserved.

Regardless of the mechanism of compression, the phase space plots of a given electron in the initial and final configurations will look similar to the respective phase space plots in Figure 21(b). In this figure and throughout the rest of this section, the $\parallel$ subscript is suppressed. The cross-hatched areas must be equal, since $\oint v\, dz = I$ is constant. From the approximation that ϕ is constant in z over some plasma length L, the area, ϕ, enclosed by either curve in Figure 21(b) can be written as

$$\frac{I_o}{2} = v L + 2G v \lambda(v) = \text{constant} \tag{A7}$$

where $\lambda(v)$ is the distance an electron of velocity v travels into an end sheath. G is the ratio of the cross-hatched area in one end sheath region to the larger area $2v\lambda(v)$. G is, of course, determined by the details of the potential dependence in the end sheath, and could in general become a complicated function of v when V_0 is only barely sufficient to confine the plasma. For simplicity, we

assume that V_0 is sufficiently negative so that G is essentially independent of v. (For example, if the sheath potential varies as z^2, then the electron motion considered solely over both end sheaths is that of a simple harmonic oscillator. The electron's path in phase space is then half of an ellipse in a sheath region, and $G = \pi/2$.) Then (A7) can be rewritten as

$$\text{const} = v(L + 2G\lambda(v)) \equiv v L_{eff}(v) . \tag{A8}$$

For thermal electrons, $\lambda(v) \simeq \lambda_D$. The effective length, $L_{eff}(v)$, is now a function of electron velocity. $L_{eff}(v)$ is not equal to the distance between the electron's turning points (unless $G = 1$), nor is it equal to the geometric length of the containment volume. $L_{eff}(v)$ can also be a function of radius.

Since $L_{eff}(v)$ is now a function of velocity, any given compression of an initial Maxwellian will not result in a final Maxwellian. A crude estimate of ratio of the final velocity, v_2, to the initial velocity, v_1, is found by equating (A8) for two different effective lengths:

$$v_1(L_1 + 2G\lambda_1(v_1)) = v_2(L_2 + 2G\lambda_2(v_2)) . \tag{A9}$$

L_1, L_2 are now the respective constant ϕ region lengths, not the geometrical confinement lengths. The initial distribution is Maxwellian at temperature T_1, and the plasma has an initial Debye length λ_{D1}. We estimate the end sheath penetration distance as

128

$\lambda_1(v_1) \simeq \lambda_{D1} mv_1^2/T_1$. We further assume $L_{1,2} \gg 2G\lambda_{D1,2}$ (in our plasmas, $\lambda_D/L \sim 10^{-2}$). By assuming the compression results in an approximate Maxwellian at T_2 , we estimate $\lambda_{D2} \cong \lambda_{D1}(L_1/L_2)^{1/2}$, and $v_2^2/T_2 \simeq v_1^2/T_1$ for the purpose of calculating $\lambda(v_2)$. Thus we approximate $\lambda(v_2)$ in terms of v_1, L_1, L_2, λ_{D1} and T_1 as

$$\lambda(v_2) \simeq \lambda_{D1}(L_1/L_2)^{1/2}(mv_1^2/T_1) \ . \tag{A10}$$

Within these approximations, v_1/v_2 is found as

$$\frac{v_1}{v_2} \simeq \frac{L_2}{L_1}\left(1 + 2G\frac{\lambda_{D1}}{L_1}\left(\frac{mv_1^2}{T_1}\right)\left[\left(\frac{L_1}{L_2}\right)^{3/2} - 1\right]\right). \tag{A11}$$

For thermal electrons, $mv_1^2/T_1 = 1$. The percentage deviation of v_2 from the corresponding v_2' obtained if the compression were described by the simple piston model of compression ratio

$$\frac{L_{eff_2}}{L_{eff_1}} = \frac{L_2}{L_1}\left(1 + 2G\frac{\lambda_{D1}}{L_1}\left[\left(\frac{L_1}{L_2}\right)^{3/2} - 1\right]\right) \tag{A12}$$

is given by

$$\frac{v_2}{v_2'} \cong 2G\frac{\lambda_{D1}}{L_1}\left[\left(\frac{L_1}{L_2}\right)^{3/2} - 1\right]\left[1 - \frac{mv_1^2}{T_1}\right] \tag{A13}$$

For $L_1 = 2L_2$, $G \sim 1$, $\lambda_{D1}/L_1 \sim 10^{-2}$, (A13) is evaluated to be $v_2/v_2' = 0.04 (1 - mv_1^2/T_1)$. Thus, over a range $0 \le v_1 \le 2\bar{v}_1$, the resultant v_2 distribution is estimated to be within about 10% of the

Maxwellian distribution of velocities v'_2 determined by a simple pistonlike compression between two effective lengths $L_{eff_1} = (L_1 + 2G\lambda_{D1})$ and $L_{eff_2} = (L_2 + 2G\lambda_{D2})$.

Although this model of compression is admittedly crude (G, for instance, may also be a function of velocity, and $\lambda(v)$ may not simply scale with the kinetic energy), the estimate of the resultant velocity distribution's deviation from a Maxwellian (about 10% over the bulk of the distribution) is probably close to the actual case for the studied range of compressions and lengths. Thus the approximation that an initial Maxwellian results in a final Maxwellian after compression is seen to be reasonably good.

(iii) Experimental measurement of γ

An experimental determination of γ was made from $T_{\parallel\epsilon}$ data in order to see if an essentially 1-D compression was indeed the result of a compression of the studied plasmas. This determination is not meant to be an exact analysis of the compression, but rather it is to be viewed as a confirmation of the 1-D compression assumption.

An experimental measurement of γ can be made from measurements of $T_{\parallel\epsilon}$ (parallel tail energy scale) just prior to and just after a compression. These measurements must, of course, be corrected for the cooling experienced as the dump confinement voltage is reduced (see section 3. C.ii and equation (3. C.ii. 12).) The

130

effective lengths were estimated from the density and potential measurement data. The results are given in Figure 22. The plot shows the data points $(T_{\|\epsilon_f}/T_{\|\epsilon_i})$ vs $(L_{eff_i}(2\bar{v}_i)/L_{eff_f}(2\bar{v}_f))$. The solid line is the 1-D prediction of $\gamma = 3$. The data points are best fit by $\gamma = 2.88$. That the measured γ is very near 3 suggests that the one-dimensional adiabatic compression is a reasonably good model, at least for the higher energy electrons.

Because the collisionality of the electrons decreases with increasing energy as the 3/2 power, one can worry that the bulk of the electrons ($v \leq \bar{v} = (T_{\|}/m)^{1/2}$) may significantly depress γ when it is determined from measurements over the entire distribution. An indication of this averaged γ can be given by measuring $T_{\perp}$ just before and well after the compression, when the induced anisotropy has decayed to the final equilibrium. Then, assuming that there are no collisions during the compression and that there is conservation of energy during the anisotropic decay, the final temperature, T_{eq_f}, is found from

$$\frac{1}{3} T_{\|} + \frac{2}{3} T_{\perp} = T_{eq_f} \quad , \tag{A14}$$

where $T_{\|}$ and $T_{\perp}$ are measured at any time after the anisotropy is induced. With these assumptions, a 1-D compression will result in the following relationship:
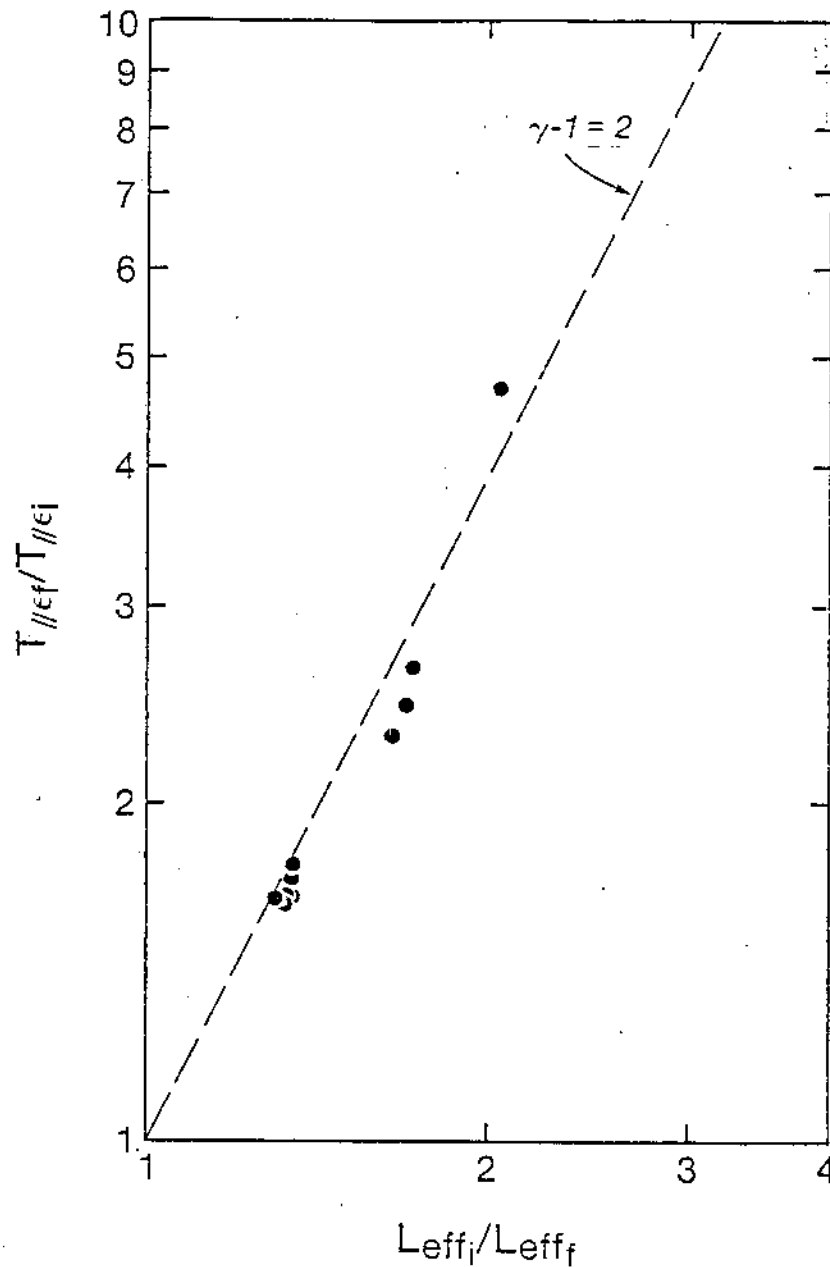
Figure 22. $T_{\|e_i}$ data is taken just before the compression, and $T_{\|e_f}$ is taken at the end of the compress potential ramp. The ratios are corrected for dump cooling using the estimate (3.D.ii.12), and are plotted against the estimated effective length ratios. The point at $T_f/T_i \sim 4.6$ is considered unreliable due to the large cooling correction required. The estimated errors in both the measured length and temperature ratios is about 10% for the other points. The dashed line is the $\gamma = 3$ theoretical prediction.

$$3 \left(\frac{T_{eq_f}}{T_{eq_i}} \right) - 2 = \left(\frac{L_i}{L_f} \right)^2 \quad , \tag{A15}$$

where $T_{eq_{i,f}}$ and $L_{i,f}$ are the equilibrium temperature and effective lengths before and well after the compression.

Figure 23 shows a plot of some data points (for both compression and expansion), where L_i/L_f is figured from lengths calculated using the density and potential diagnostic to find the region of essentially unchanging potential. The solid line is the relationship (A15). A best fit line through the origin gives $\gamma^* = 2.62$, but γ^* is not a measurement of γ since a straight line in these variables presupposes a 1-D compression with no collisions. Nevertheless, this plot indicates that $\gamma \sim 3$, and that both perpendicular and parallel distributions will be approximately Maxwellian after a compression albeit with different temperatures.

(iv) $T = 0$ compression in long cylinders

In this section we discuss a simple model of the process whereby a very long plasma, such as the plasma occupying Ll and L2 in Figure 21(a), is excluded from Ll by the application of a slowly changing potential, V_c, to Ll. We will find that, for a long, cold plasma, the plasma is axially excluded from the L_1 region in thin cylindrical shells of successively smaller radii. These shells enhance the density in L_2 at their respective radii. This model of

133

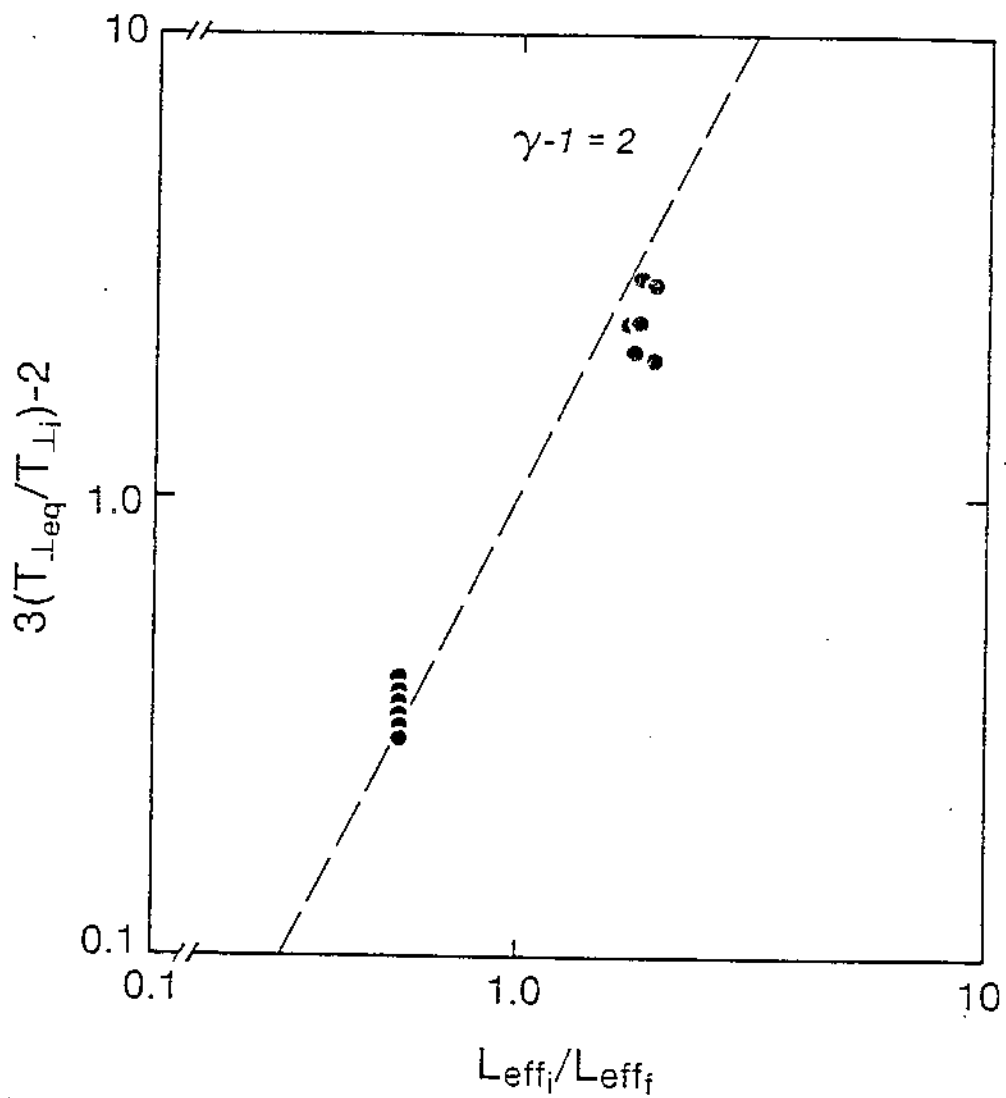Figure 23. Plot similar to Figure 22, but using $\langle E_\perp \rangle$ data. The dashed line is the 1-D prediction of theory.

axial compression is shown to conserve the adiabatic bounce invariant $I_\parallel$, and thus leads to the same general results as those of section (i) - (ii).

We insure a simple model by assuming that the plasma temperature is so low that R_2 , the radius of the plasma, is very many Debye lengths in extent. In the limit $R_2/\lambda_D \to \infty$, the kinetic energy of the electrons can be neglected. All electrons are assumed to remain on field lines.

The potentials $\phi_{1,2}(r)$ in L_1, L_2 are assumed to have negligible z dependence (long cylinders and plasma), at least when calculated well away from the ends of L_1, L_2 . We assume that the plasma will act in such a way as to keep the potential functions $\phi_1(r)$, $\phi_2(r)$ equal where possible; this means matching the potentials $\phi_1(r) = \phi_2(r)$ at all radii where $n_1(r)$ and $n_2(r) \neq 0$. When $V_c = 0$, this requirement is trivially satisfied. As V_c slowly changes from zero, however, the potential $\phi_1(r)$ is then given by the solution to the 2-D Poisson equation with V_c as the boundary condition and $\rho_1(r)$ as the density function:

$$\frac{1}{r} \frac{d}{dr} r \frac{d}{dr} \phi_1(r) = 4\pi e\, \rho_1(r) \ , \tag{A16}$$

By integrating in r twice, an integral equation for the potential at any radius is obtained:

$$\phi_1(r) = -4\pi e \int_r^{R_\omega} \frac{dr'}{r'} \int_0^{r'} r'' \rho_1(r'') \, dr'' + V_c \, . \qquad (A17)$$

R_ω is the cylinder wall radius and V_c is the boundary condition applied to L_1. As can be seen from (A17), changing V_c only changes the overall potential level of each electron in L_1, at least near the axial center of L_1; the functional form of $\phi_1(r)$ is unchanged. The potential $\phi_2(r)$ well within L_2 can be similarly found:

$$\phi_2(r) = -4\pi e \int_r^{R_\omega} \frac{dr'}{r'} \int_0^{r'} r'' \rho_2(r'') \, dr'' \, . \qquad (A18)$$

We then equate $\phi_1(r) = \phi_2(r)$ wherever $\rho_1(r)$ and $\rho_2(r)$ are both non-zero. Before the compression starts, $V_c = 0$, and $\rho_{10}(r) = \rho_{20}(r) \equiv \rho_0(r)$ for all r is the initial condition which satisfies $\phi_1(r) = \phi_2(r)$. When $V_c \neq 0$, $\rho_1(r) = \rho_2(r)$ over some range $r \leq R_1 < R_2$ where R_1 and R_2 are the plasma radii in L_1 and L_2, respectively. This is because the detailed balance of $\phi_1(r) = \phi_2(r)$ over this range requires the same radial dependence where there is plasma; this balance is only satisfied if $\rho_1(r) = \rho_2(r)$ in this region regardless of V_c.

Thus changing V_c causes the plasma in a cylindrical shell between R_1 and R_2 to be moved from L_1 into L_2. This causes $\rho_1(r)$ in the remaining plasma to be uniformly lowered (by some

factor less than V_c), and $\phi_2(r)$ to be identically lowered over the same radius (by the additional charge outside $r = R_1$).

The potential equality condition, $\phi_1(r) = \phi_2(r)$ for $r \leq R_1$ and the particle conservation equation, $-\Delta\rho_1(r) L_1 = \Delta\rho_2(r) L_2$ for $r > R_1$, can be written as one integral equation by equating (A17) and (A18) to yield

$$\int_{R_1}^{R_\omega} \frac{dr'}{r'} \int_{R_1}^{r'} dr'' \; r'' \rho_0(r'') \left[1 - H(r'' - R_2) \right] = - \frac{V_c}{4\pi e(1 + L_1/L_2)}$$

$$(A19)$$

where $H(x)$ is the Heaviside step function; i.e. $H(x) = 1$ for $x > 0$, $H(x) = 0$ otherwise. Equation (A19) can, in principle, be solved for R_1 as a function of V_c for a given initial density profile $\rho_0(r)$. For example, a constant density $\rho_0(r) = \rho_0$ gives the transcendental equation for R_1 :

$$R_2^2 \left(1 + \ln(R_\omega/R_2)^2 \right) - R_1^2 \left(1 + \ln(R_\omega/R_1)^2 \right) = \frac{V_c}{\rho_0 \pi e(1 + L_1/L_2)} \; .$$

$$(A20)$$

The prediction of the analysis is simple. As V_c is slowly changed, the radius of the plasma in L_1 shrinks. The density within that radius in L_2 stays constant, but the density in the outer radial regions is increased. Although the result (A20) neglects any temperature effects, i.e. particles have no parallel kinetic energy in this model, (A20) is expected to be approximately correct when the plasma

137

is many Debye lengths in radius.

Since this model of axial compression assumes that the electron's kinetic energy is negligible, it cannot directly address the question of compressive heating. We therefore look at an individual electron, and consider its kinetic energy as a function of V_c. In the spirit of the above compression model we start this electron at velocity V_z, in L_1 and follow it as V_c slowly changes from zero. We will find that the bounce adiabatic moment, $I_\parallel$, will again remain conserved if V_c is changed slowly enough, and that eventually the electron will be unable to enter L_1 from L_2.

The mechanism which changes v_{z1} is found in equation (A17). Assume an electron has velocity v_{z1} after it enters the radial Debye sheath region of the plasma in L_1, which has already been partially compressed. (See Figure 24.) The Debye sheath is, of course, due to a distribution of parallel velocities; the electrons with relatively large velocities will be able to surmount the axial potential gradient at the L_1-L_2 boundary, while slower ones won't. The electrons which do reach L_1 will remain in L_1 for approximately $2L_1/v_{z1}$ sec. During this time, V_c will change by an amount

$$\Delta V_c \cong \frac{dV_c}{dt} \frac{2L_1}{v_{z1}} \ . \tag{A21}$$

This means the potential energy of the electron has increased by $-e\Delta V_c$ when it is ready to re-enter L_2. Since there are no axial
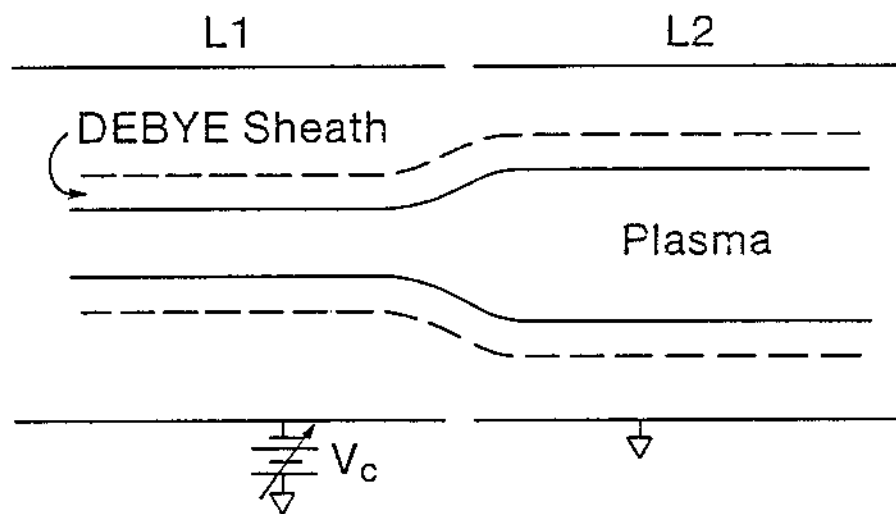
Figure 24. Partially compressed long plasma in the vicinity of the compress boundary.

electric fields in L_1 (except at the reflecting end and at the L_1-L_2 boundary), v_{z1} remains constant while the potential energy of the electron increases. To the approximation that there has been no change in density in L_2 (i.e. neglect the change in space charge from the particle compression), all of the gain in potential energy gained in traversing L_1 will appear as an increase in v_{z2}, the electron velocity in L_2.

If V_c is changed slowly enough, then the oscillatory description of the electrons' motion in L_1 and L_2 will contain a conserved bounce adiabatic invariant, $\oint v_z \, dz$. In this case, the slowly varying parameter of the motion is the field $\phi_1(r)$. The conservation of the adiabatic bounce invariant in turn means that all the compression results of sections (i) and (ii) will apply to this hybrid model as well. Thus this simple model of long plasma compression can also result in a 1-D compression providing the collision rate is also sufficiently low.

(v) Cyclic heating

The method of adjusting the initial temperature (before the anisotropy is induced for evolution studies) of the plasma is described by a simple model of alternate 1-D expansions and compressions interspersed with waiting periods which allow collisional equilibration between $T_\parallel$ and $T_\perp$. The final volume of the plasma is the same as the original, but final temperature has been increased due to the net increase in entropy caused by the two collisional processes. Since the

plasma lengths accessible to the EV device are limited, fine control of the final equilibrium temperature is provided by adjusting the amount of time available for collisions during the equilibration phase of the cycle. Many cycles can be put together to attain a large increase in the final temperature.

For simplicity, the 1-D adiabatic ideal gas compression model of sections (i) and (ii) is assumed, along with a long plasma assumption that compressions take a Maxwellian $v_\parallel$ to a new Maxwellian. Figure 25 shows a plot of parallel temperatures vs the L, the effective plasma length, around one heating cycle. An initial expansion was chosen: similar results are obtained for an initial compression.

State (a) starts in equilibrium $T_\parallel = T_\perp = T_0$ with length L_0. A 1-D (collisionless) expansion to length L_1 takes the plasma to state (b), where $T_\parallel = T_0 (L_0/L_1)^2 < T_\perp = T_0$. The plasma is then allowed to remain at length L_1 while collisions bring $T_\parallel$ and $T_\perp$ into equilibrium. The new equilibrium temperature at state (c) is calculated to be $T_1 = \frac{1}{3} T_0 (2 + (L_0/L_1)^2)$. Similar calculations can be made in taking the plasma to state (d) via a 1-D adiabatic compression, and to state (e) via collisional equilibration, which causes a further increase in entropy. In the final state (e), the plasma has returned to its original volume, and has an increased equilibrium temperature T_0':

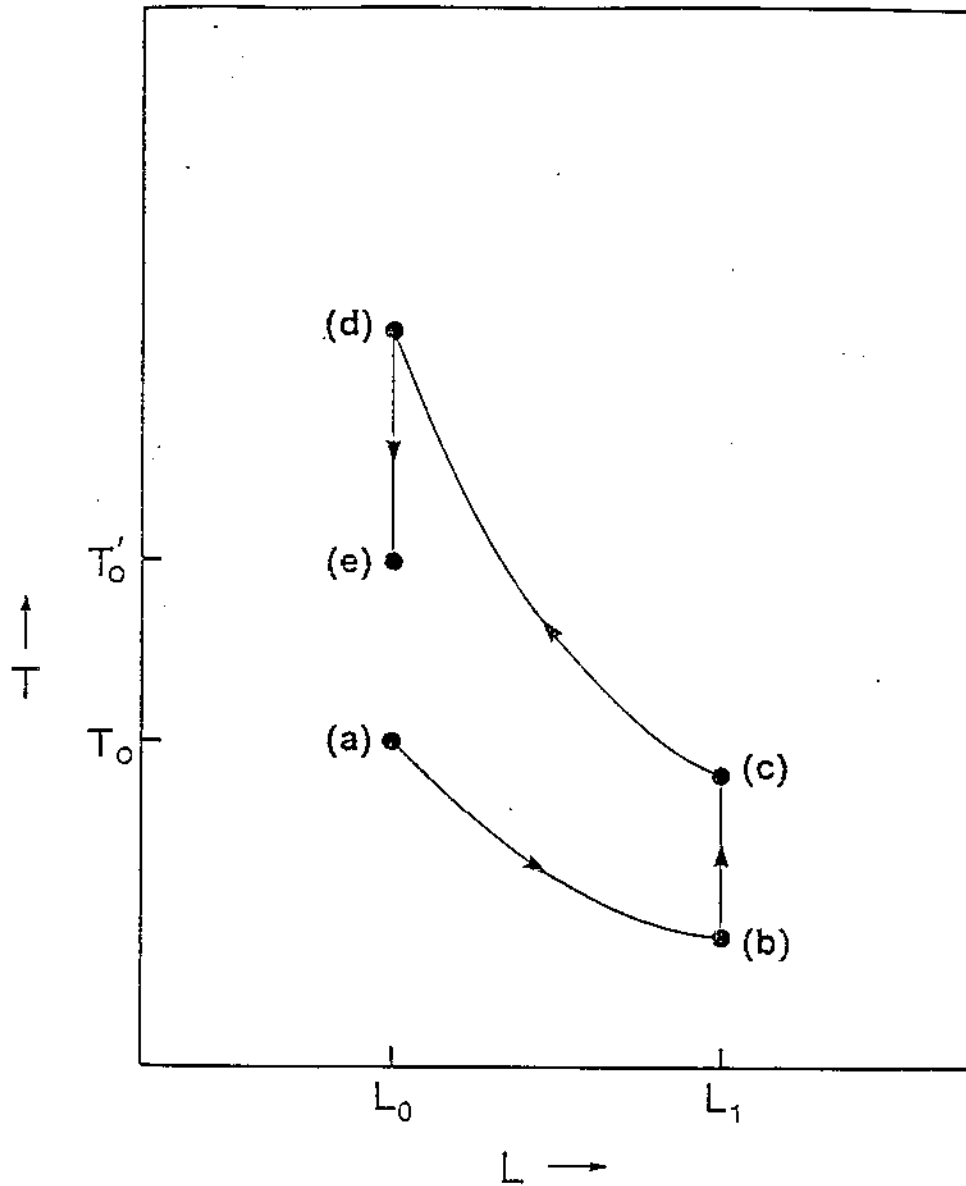$$T_0' = \frac{1}{9} T_0 (2 + (L_1/L_0)^2)(2 + (L_0/L_1)^2) \ . \qquad (A22)$$

141

Figure 25. The parallel temperature, T, plotted as a function of plasma length L over one full heating cycle. Full equilibration is assumed going from points (b) - (c) and from (d) - (e). The final temperature, T_o', is given by $T_o' = (T_o/9) [2 + (L_1/L_0)^2][2 + (L_0/L_1)^2]$. The difference $T' - T_o$ can be adjusted by reducing the time allowed for equilibration.

This increase in temperature is a result of net work done on the plasma by the compress potential's power supply. Figure 26 shows a p-V plot for the cycle; the net work done on the plasma is given by the cross-hatched area and is equal to $\oint p\,dV$ around the cycle. By using the ideal gas relationship $pV = NT$, the net work done on the plasma is given by

$$W_{net} = -\frac{NT_0}{3}\left(1 - \left(\frac{L_0}{L_1}\right)^2\right)\left(1 - \left(\frac{L_1}{L_0}\right)^2\right) \quad , \qquad \text{(A23)}$$

where N is the total number of electrons. There is no net work done associated with the plasma potential energy in this approximation. Equation (A22) is easily recovered from (A23) by using

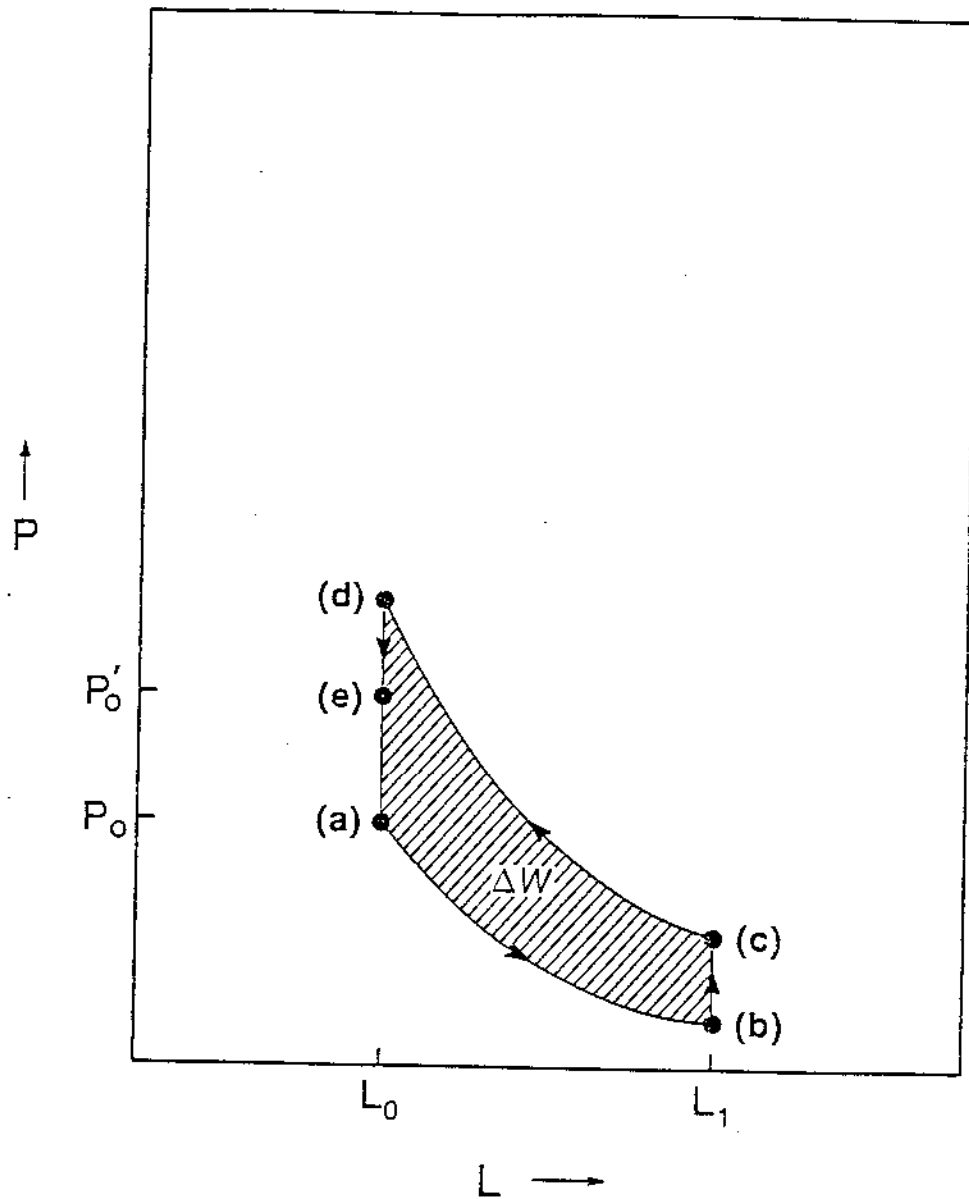$$\Delta W_{net} = C_v \Delta T = (3/2)\,N\,(T_0' - T_0).$$

Figure 26. The pressure as a function of length for the same case as Figure 25. The total work done on the plasma, ΔW, is the cross-hatched area.

144

APPENDIX B: Density Fluctuation Reduction Technique

This appendix describes a technique which drives down the level of fluctuations of the basic measurement, $Q(r)$, by as much as a factor of five. ($Q(r)$ is the number of electrons which pass through the collimator hole.) This in turn allows up to a fivefold decrease in the random error in the measurement of $T_\perp$ (and the relaxation rate derived from the $T_\perp$ evolution) for the same amount of data. The same decrease in random error would require up to 25 times as much data if the technique was not employed. This would take a prohibitively long time. The technique itself is a very simple one.

The technique is simply to tilt the magnetic field away from the axis defined by the confinement geometry after the plasma has been injected and confined. The technique, and some of its consequences, was first investigated by K. Fine. The field is tilted by the trimming coils, which were designed to remove the earth's magnetic field, and align the total field with the confinement geometry axis. These coils produce essentially uniform fields within the confinement volume that are perpendicular to the main solenoidal field and each other. By applying more perpendicular field than is necessary for alignment, the total field can be precisely tilted away from alignment. This additional perpendicular field is applied for several tenths of a second, starting just after the plasma is confined. The level of fluctuations in $Q(r)$ decline during the tilt period at an enhanced rate.[61]

145

At the end of the desired tilt period, the field is realigned with the confinement axis, and the rest of the experiment proceeds normally. Part of the tilt period is devoted to the time the changed perpendicular field requires to fully penetrate the stainless steel vacuum jacket. This time is on the order of a tenth of a second.

Figure 27 shows measurements of the root mean square percentage deviation of the fluctuations, σ, made on the axis as a function of the tilt angle in degrees, $\Delta\theta = \Delta B_x / B_z$, where ΔB_x is the perpendicular field magnitude. The RMS percentage deviation is defined as

$$\sigma = \left[\frac{1}{N} \sum_i (Q_i(0) - \bar{Q}_i(0))^2 \right]^{1/2} \Big/ \bar{Q}_i(0) \qquad (B1)$$

where $\bar{Q}(0)$ is the average value of the total number of electrons to pass through the axially centered collimator hole, and N is the number of measurements of $Q_i(0)$. B_z is 281 Gauss, and the plasma is contained within L1-L4. ΔB_x is turned on 30 msec after injection and is kept on for 0.8 sec. The plasma is dumped and $Q_i(0)$ is measured at 1 sec after inject. The line shown is the result of a fit by eye to the measured $\sigma(\Delta\theta)$ data taken at various values of $\Delta\theta$. There is a fivefold reduction in σ when $\Delta\theta \geq 0.5$ degrees; increasing $\Delta\theta$ beyond that doesn't yield much more improvement.

The technique becomes less effective as the length of the plasma is decreased. Therefore the technique was always employed
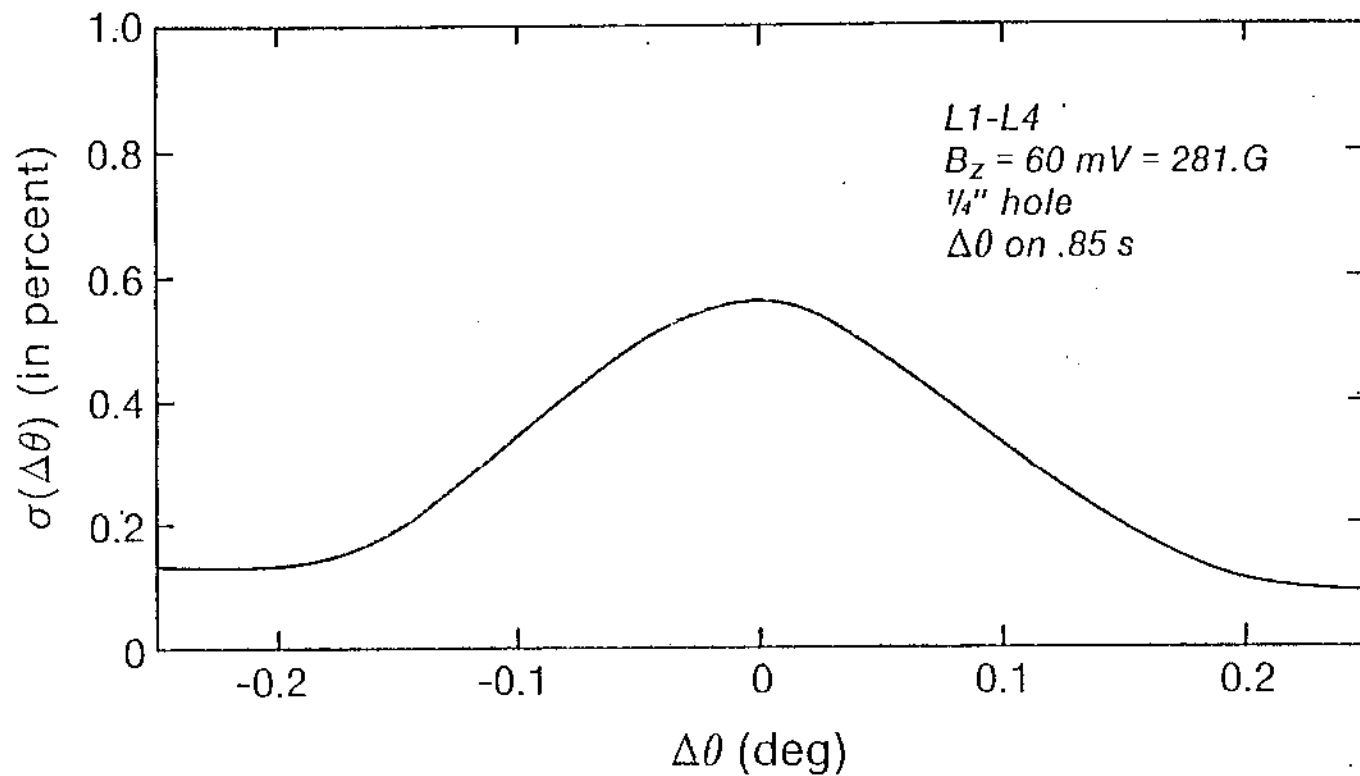
Figure 27. Plot of $\sigma(\Delta\theta)$, the percentage RMS deviation in individually measured $Q(r)$, as a function of $\Delta\theta \cong B_\perp/B_z$, the tilt angle between the magnetic field and the confinement symmetry axis. The 1/4" collimator hole is centered on the axis, and $B_z = 281$ Gauss. The solid line is determined by an eyeball fit to the $\sigma(\Delta\theta)$ data.

when the plasma length was a maximum; the effect is not destroyed by subsequent axial compression. The tilt angle which produces the minimum σ is a function of B_z. Figure 28 shows curves similar to that of Figure 27 for several values of B_z. The time the tilt was on is 1.9 sec for this series. Note that for the two lower fields σ displays a minimum at some particular value of $\Delta\theta = \Delta\theta_m$. Figure 29 plots $\Delta\theta_m$ as a function of B_z; where no minimum is found $\Delta\theta_m$ is set to be where σ no longer changes rapidly with $\Delta\theta$. $\Delta\theta_m$ seems to scale like B_z^2. At present, it is not known why there is not a well defined minimum of $\sigma(\Delta\theta)$ for $B_z = 281$ Gauss. Presumably the lack of a minimum can also be found at higher values of B_z.

The overall effect of this technique on the plasma can be seen in Figure 30, which shows the plasma radial profile at 2 sec both with and without utilizing the technique. There is a striking difference in the two profiles. This difference appears to be brought about by an enhanced internal rearrangement caused by the tilted field, along with an enhanced external transport (increased mean square radius). The temperature has risen and become more uniform, most probably due to a transformation of electrostatic energy to thermal energy as the plasma density profile changes.

There is as yet no theoretical model which describes the effect of the tilted field upon σ, although existing theories of resonant particle-wave interaction may eventually explain the transport features
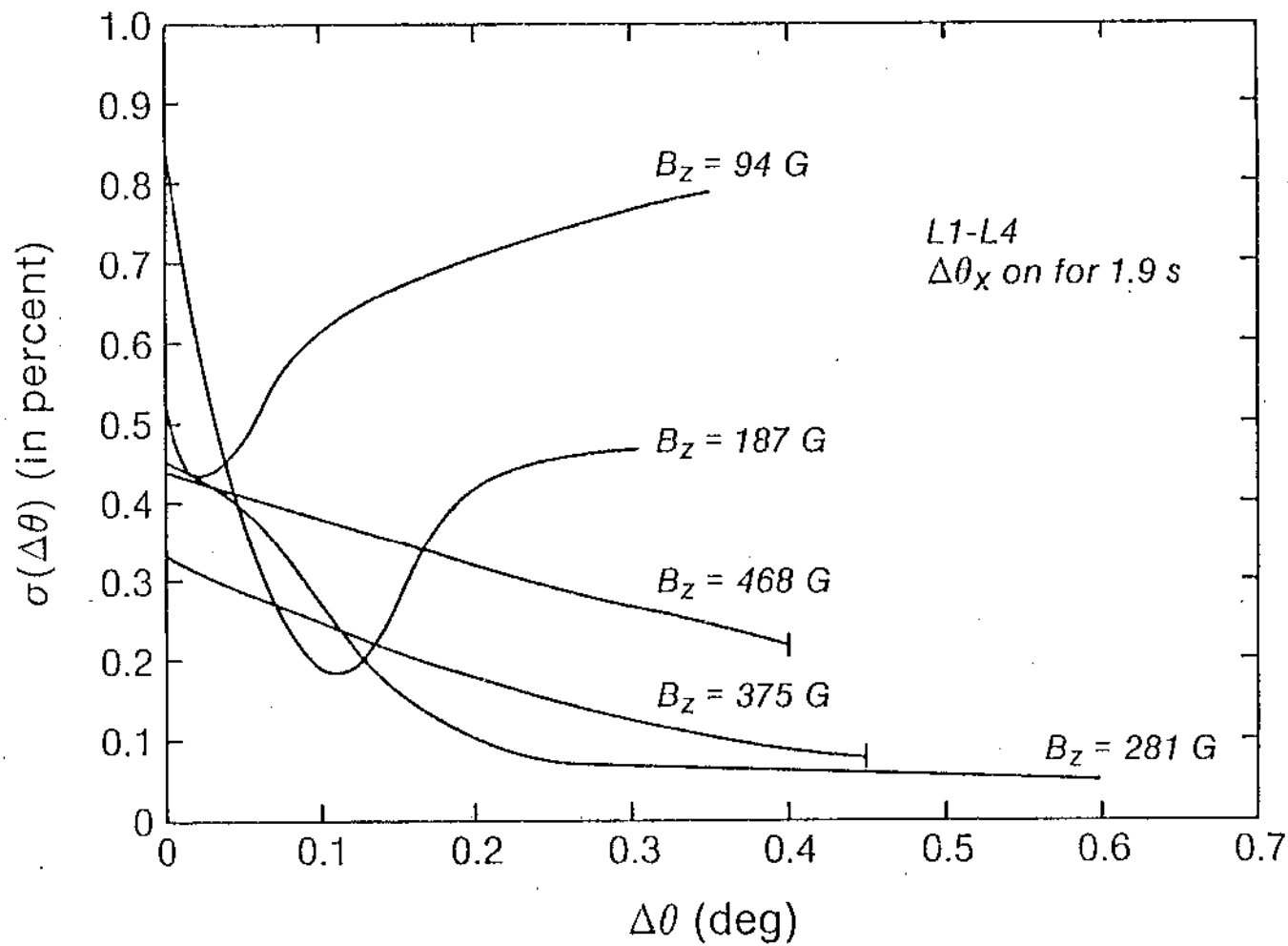
Figure 28. Plots similar to that of Figure 27 for various values of B_z. The three fitted lines representing $\sigma(\Delta\theta)$ data for $B_z \geq 281$ Gauss are plotted out to the maximum $\Delta\theta$ attainable with the B_z power supply.
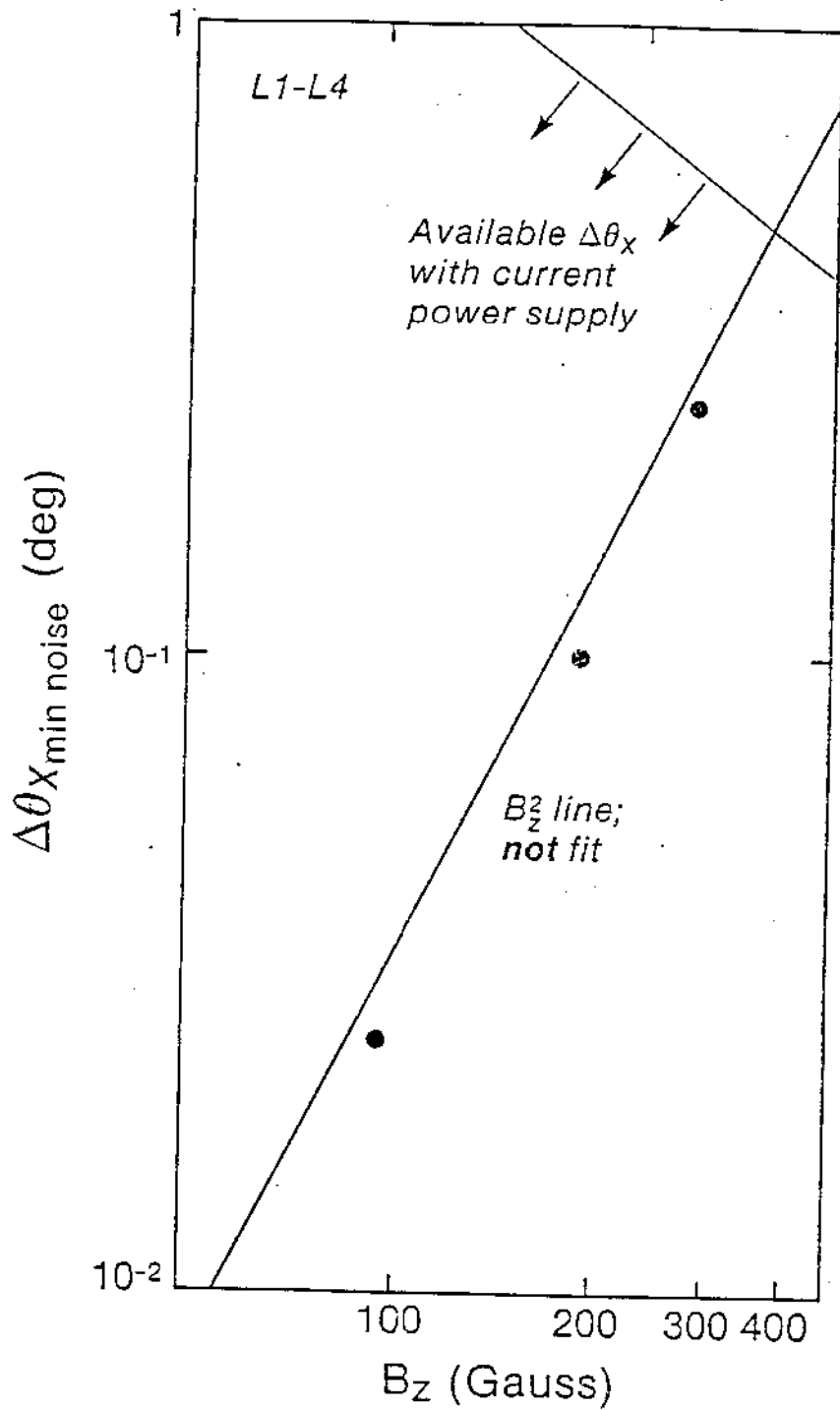
Figure 29. Plot of the most effective $\Delta\theta$ vs. B_z. Data taken from Figure 28. The most effective $\Delta\theta$ is either a minimum of $\sigma(\Delta\theta)$ or the value of $\Delta\theta$ where $\sigma(\Delta\theta)$ stops significantly changing.
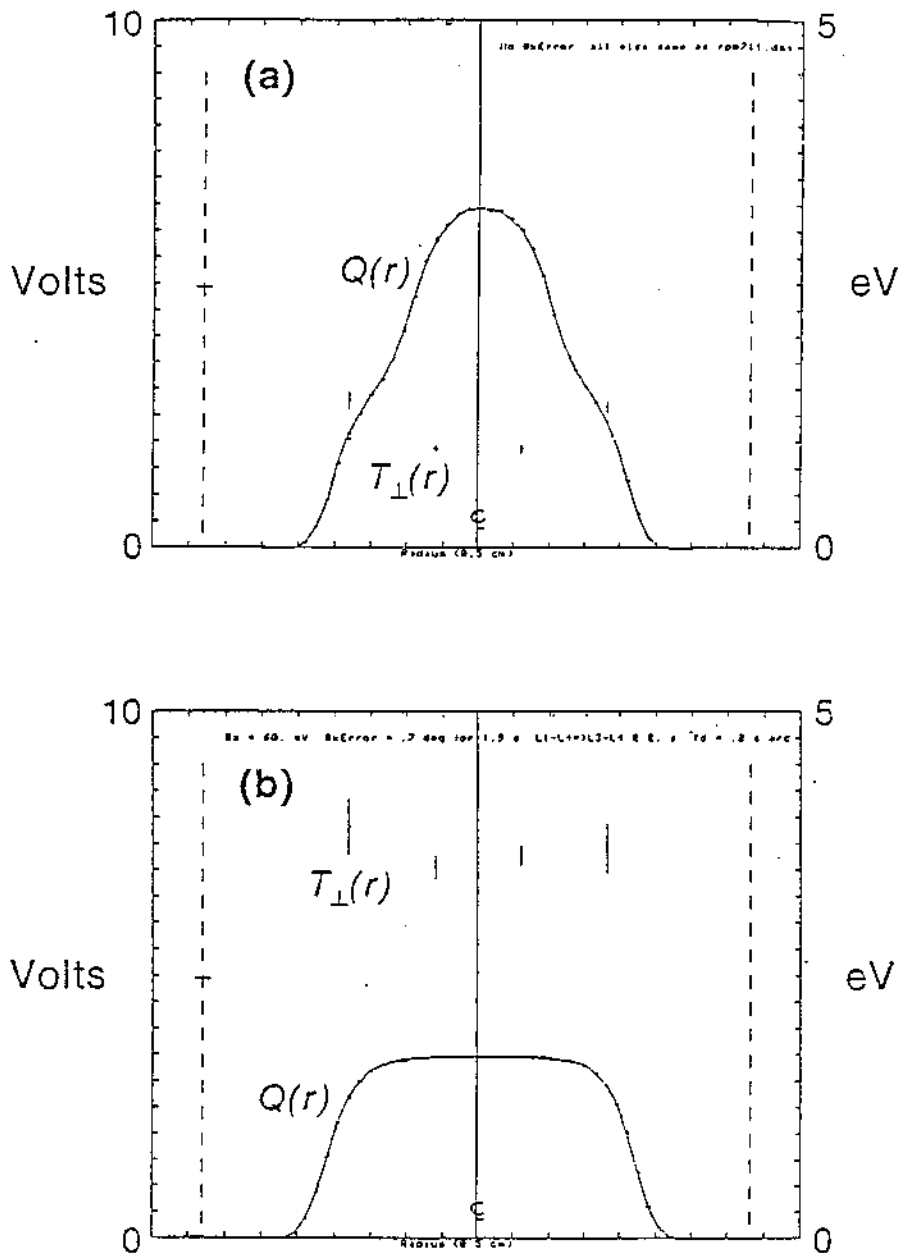
Figure 30. Radial density profiles (with 4 $\langle E_\perp \rangle$ data points also shown) taken at 2 sec both without any tilt (a), and with 1.9 s of $\Delta\theta = 0.35$ degrees of tilt (b). See Figure 3 for an explanation of the graph structure and scales. The total number of electrons is the same for graphs (a) and (b).

and the damping of the density fluctuations. Since the plasma is rotating in the lab frame, the static tilted field appears to oscillate in a frame rotating with the plasma, and therefore this "wave" could interact with both plasma collective modes and particles (wave-wave and wave-particle interactions if linear, or a more complicated interaction if non-linear). This effect has not been studied beyond the amount necessary to utilize it as a means of reducing σ and verifying that such reduction does indeed result in improvements in the measurement of $T_\perp$ and relaxation rates. Since the tilted field is realigned with the confinement axis several collisions times before an anisotropy is induced, any lingering disturbance to the velocity distribution should be removed by electron-electron collisions. Thus this tilted field technique should not affect any of our measured relaxation rates.

APPENDIX C: $T_\perp$: First Order Correction Technique

Figure 10a shows a typical curve of $N(V_A, \gamma = 0)/N(0,0)$, the fraction of incident electrons which pass through the analyzing cylinder A3, as a function of the negative potential, V_A, applied to A3. The secondary field, B_s, is equal to zero. Also shown is the relative fraction chosen for all $\langle E_\perp \rangle$ measurements, $N(\tilde{V}_A, 0)/N(0,0) = 0.5$. In general, the $\tilde{V}_A$ so chosen will depend upon the confined plasma's space charge potential and parallel kinetic energy distribution. $\tilde{V}_A$ is experimentally found by first measuring $N(0,0)$ and then $N(V_A, 0)$ on successive shots as V_A is decremented, until the desired ratio is bracketed. $\tilde{V}_A$ is then estimated by interpolation, and checked by measurement, and if necessary iterated until $N(\tilde{V}_A, 0)/N(0,0)$ is within 5% of the desired value. Greater accuracy in the choice of $\tilde{V}_A$ seems unnecessary.

The two derivatives, $\partial N(\tilde{V}_A, 0)/\partial V_A$ and $\partial N(\tilde{V}_A, 0)/\partial \gamma$, are then measured. Historically,[52] each was measured using a two-point method,

$$\frac{\partial N(\tilde{V}_A, 0)}{\partial V_A} \approx \frac{N(\tilde{V}_A + \Delta V_A, 0) - N(\tilde{V}_A, 0)}{\Delta V_A}, \qquad \text{(C1)}$$

and similarly for the γ derivative. $N(V_A, 0)$ is typically not a linear function of V_A, and so ΔV_A must be very small for an accurate slope measurement. Repeated measurements of $N(\tilde{V}_A, 0)$, etc., in general display statistical variations about some average value. If we assume

a "normal" or Gaussian distribution of values of standard deviation σ about the mean value, that ΔV_A has no associated measurement error, and that each point, $N(\tilde{V}_A + \Delta V_A, 0)$ and $N(\tilde{V}_A, 0)$, are measured J times, then the statistically derived standard error in the measurement of the slope is

$$\text{Std. Er.} = \frac{\left(\sigma^2_{(\tilde{V}_A + \Delta V_A)} + \sigma^2_{\tilde{V}_A}\right)^{1/2}}{J^{1/2}\,\Delta V_A} \tag{C2}$$

where the standard deviation, $\left[\sigma^2_{\tilde{V}_A}\right]^{1/2}$, is measured as

$$\sigma^2_{\tilde{V}_A} = \frac{1}{J-1}\sum_{i=1}^{J}\left[N_i(\tilde{V}_A, 0) - \overline{N}(\tilde{V}_A, 0)\right]^2 , \tag{C3}$$

and

$$\overline{N}(\tilde{V}_A, 0) = \frac{1}{J}\sum_{i=1}^{J}N_i(\tilde{V}_A, 0) \tag{C4}$$

is the mean value. Maintaining an acceptably small σ while decreasing ΔV_A requires $J^{1/2}$ to increase, which rapidly increases the total time each $\langle E_\perp \rangle$ measurement requires.

Unfortunately, a finite ΔV_A (and/or $\Delta \gamma$), leads to a first order systematic error in the measured $\langle E_\perp \rangle$ when slopes are measured using the approximation (C1). If we Taylor expand equations (3.C.i.2) and (3.C.i.3) about $\gamma = 0$ and $V_A = \tilde{V}_A$, respectively, we find, to first order,

154

$$-\frac{e\dfrac{\Delta N(\tilde{V}_A,0)}{\Delta \gamma}}{\dfrac{\Delta N(\tilde{V}_A,0)}{\Delta V_A}} \equiv \langle E_\perp \rangle_{\text{meas.}} \cong \langle E_\perp \rangle \left[1 + \frac{1}{2}\frac{f'(e\tilde{V}_A)}{f(e\tilde{V}_A)}\left(\Delta\gamma\frac{\langle E_\perp^2 \rangle}{\langle E_\perp \rangle} - e\Delta V_A\right)\right] \quad .$$

(C5)

The systematic error term can be of order 10% or larger.

This level of error can be reduced by simply centering the two point measurement on $\tilde{V}_A$ (and $\gamma = 0$), that is, measuring $N(\tilde{V}_A - (\Delta V_A/2), 0)$ and $N(\tilde{V}_A + (\Delta V_A/2), 0)$. The level of error due to finite ΔV_A is then second order in ΔV_A, $\Delta \gamma$. An alternate method, and the one used for this study, is to bracket $\tilde{V}_A$ (and $\gamma = 0$) with several different values of V_A (and γ). A least-squares curve fitting algorithm is then applied to the data, which in turn gives the desired derivative. This method is capable of measuring (although with decreasing accuracy), the higher order partial derivatives. By repeated differentiation of equations (3.C.i.2) and (3.C.i.3), it is easy to show that

$$\frac{(-e)^n\left(\dfrac{\partial^n N(\tilde{V}_A,0)}{\partial \gamma^n}\right)}{\left(\dfrac{\partial^n N(\tilde{V}_A,0)}{\partial V_A^n}\right)} = \langle E_\perp^n \rangle \quad ,$$

(C6)

where $\langle E_\perp^n \rangle$ is the nth moment of the perpendicular energy distribution. This information was not used, nor investigated, in this study.

There is another source of systematic error that must be addressed. When the secondary solenoid is energized so that $\gamma > 0$, the field lines in the confinement region are slightly convergent on the axis. The amount of convergence is dependent upon distance from the secondary solenoid. Thus if we follow the field lines which pass through the collimator hole back into the confinement region, we see them slightly diverge to cover a larger area. Hence, if the collimator hole is positioned at $r = 0$, there will be more electrons passing through the collimator hole when $\gamma > 0$ than when $\gamma = 0$. The situation when the collimator hole is off axis and the density is a function of radius is more difficult to predict. There may be more or fewer electrons, depending upon where the field lines which pass through the hole originate in the plasma. This effect makes the total number of electrons through the collimator hole, N_T, a function of γ. Let $N_m(\tilde{V}_A, \gamma)$ be the measured quantity, and let $N_0(\tilde{V}_A, \gamma)$ be the value $N_m(\tilde{V}_A, \gamma)$ would have if N_T were not a function of γ, i.e. if $N_T(\gamma) \equiv N_T(0)$. Then

$$N_m(\tilde{V}_A, \gamma) = N_0(\tilde{V}_A, \gamma) \frac{N_T(\gamma)}{N_T(0)} . \tag{C7}$$

Simple differentiation with respect to γ, along with isolating the desired quantity $\partial N_0(\tilde{V}_A, 0)/\partial \gamma$, yields

$$\frac{\partial N_0(\tilde{V}_A, 0)}{\partial \gamma} = \frac{\partial N_m(\tilde{V}_A, 0)}{\partial \gamma} - N_m(\tilde{V}_A, 0) \frac{1}{N_T(0)} \frac{\partial N_T(0)}{\partial \gamma} . \quad (C8)$$

The second term on the right hand side of the equation is the correction for varying sample size to the measured derivative. This correction is measured by measuring $\partial N_T(0)/\partial \gamma$ using the same method as the measurement of the slope $N_m(\tilde{V}_A, 0)/\partial \gamma$ except $\tilde{V}_A$ is set to zero. This correction can be of the order of 10% for measurements of $\langle E_\perp \rangle$ on axis, and can be larger when $r \neq 0$. We believe that the present method of measuring $\langle E_\perp \rangle$ is accurate to better than 5%.

APPENDIX D: $T_{||}$: Analysis for Arbitrary $f(v_{||})$

An alternate method of integration can be employed to obtain a simple analytical solution to equation (3.C.ii.4) when $f(v_{||})$ is left as an arbitrary function of $v_{||}$ (still independent of r). For simplicity, r_c is allowed to become infinite, although a finite r_c can be accommodated with an increase in the complexity of the results. Equation (3.C.ii.4) is restated using $v_E = 2e/m(v_d - \phi(r,0))^{1/2}$ as the minimum escape velocity:

$$Q_e \cong -\pi n_o e L_p \int_0^\infty d(r^2) \int_{v_E}^\infty dv_{||} f(v_{||}) \quad . \tag{D1}$$

The analysis is again performed within the restricted regime of $Q_e' \simeq Q_e$, i.e. where the potential $\phi(r,0)$ may be assumed unperturbed by the loss of Q_e. The radial density is assumed to be constant out to the radius where essentially no electrons escape to contribute to Q_e. For a Maxwellian $f(v_{||})$, this radius is a few λ_D. All the other restrictions of the $T_{||}$ restriction model are retained.

$$\phi(r,0) = \phi_o - \pi n_o e r^2 \tag{D2}$$

where ϕ_o is the potential at $r = 0$ and n_o is the density. An examination of the lower limit of the $v_{||}$ integral of (D1) shows a parabolic radial dependence to v_E,

$$v_E^2 = \frac{2e}{m} (V_d - \phi_o + \pi n_o er^2) , \qquad (D3)$$

which is of the parabolic form $y^2 = a(x - x_o)$. Figure 31 shows the area in $[v_\parallel, r^2]$ space over which $f(v_\parallel)$ must be integrated to yield Q_e. The lower bound of $v_\parallel$ is the parabolic line which crosses the $v_\parallel$ axis at $v_{\parallel o} = -\frac{2e}{m} (V_d - \phi_o)^{1/2}$. The analytic solution to equation (D1) essentially involves integrating $f(v_\parallel)$ over $v_\parallel$ to generate area element (I), then integrating these elements over r^2. However, advantage can be taken of the independence of $f(v_\parallel)$ from r^2 to form area element (II) first, and then integrating over $v_\parallel$. We simply solve (D3) for r_{max}^2:

$$r_{max}^2 = \left[v_E^2 - v_{\parallel o}^2 \right] \bigg/ \left(\frac{2\pi n_o e^2}{m} \right) , \qquad (D4)$$

which leads to the alternate integral form of (D1):

$$Q_e \cong -\pi n_o e L_p \int_{v_{\parallel o}}^{\infty} dv_E f(v_E) \int_0^{r_{max}^2} d(r^2) . \qquad (D5)$$

This is trivially integrated:

$$Q_e \cong -\frac{mL_p}{2en_o} \int_{v_{\parallel o}}^{\infty} dv_\parallel (v_\parallel^2 - v_{\parallel o}^2) f(v_\parallel) \qquad (D6)$$

where the integration variable has been rewritten as $v_\parallel$. From (D6), and the definition of $v_{\parallel o}$, it is easy to show that
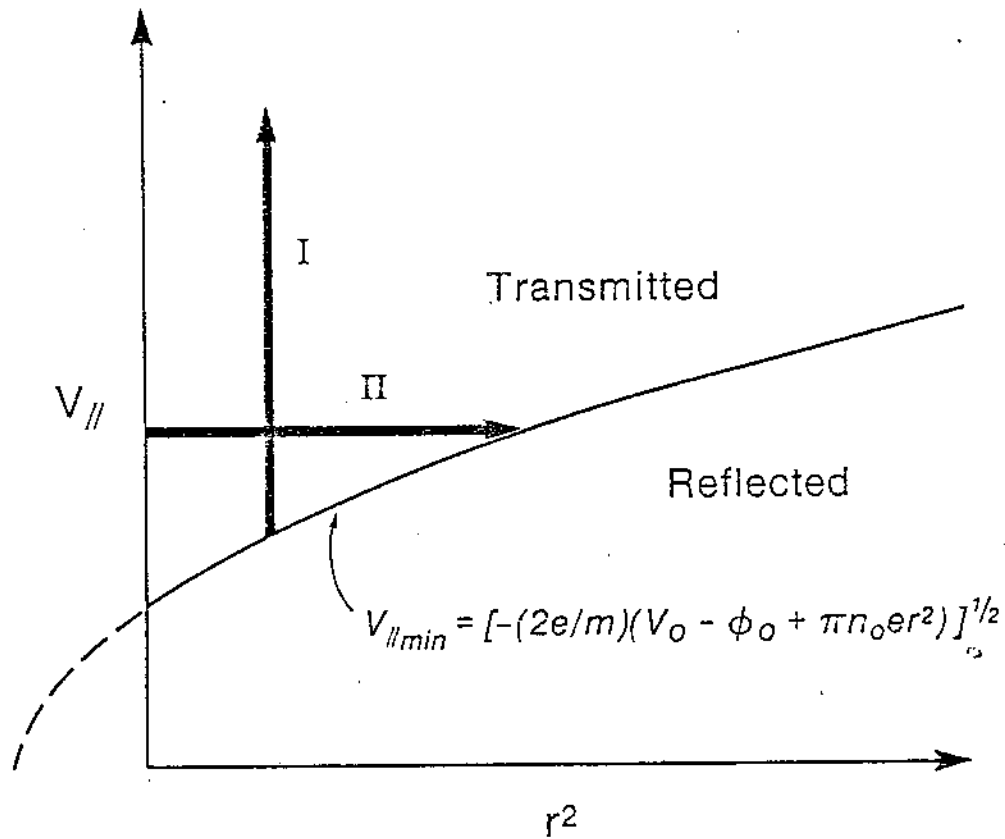
159

Figure 31. The transmission and reflection regions in $v_{\|}$, r^2 space. The lower boundary is given by the smallest $\bar{v}_{\|}$ that can penetrate the dump barrier at that radius. Area element I is found by integrating along $v_{\|}$; area element II is found by integrating along r^2.

160

$$\frac{1}{eQ_e} \frac{dQ_e}{dV_d} = \frac{d \ln Q_e}{d(eV_d)} = (\langle E_\| \rangle_> - E_{\|o})^{-1} , \tag{D7}$$

where $\langle E_\| \rangle_>$ is the average parallel kinetic energy of the electrons averaged over $f(v_\|)$ from $v_{\|o}$ to infinity, and $E_{\|o} = \frac{1}{2} m v_{\|o}^2$. Thus, for an arbitrary $f(v_\|)$, $[d \ln Q_e/d(eV_d)]^{-1}$ is the average energy in the tail of the distribution over the range of the slowest which escapes $(E_{\|o})$ to the fastest, minus the energy of the slowest to escape, $E_{\|o}$. If $f(v_\|)$ is in fact Maxwellian, at least over the range $v_{\|o} \leq v_\| \leq \infty$, i.e. $f(v_\|) \propto \exp(-m v_\|^2/2 T_{\|e})$ where $v_\| \geq v_{\|o}$, with $T_{\|e}$ the "temperature" of the tail, then $[\langle E_\| \rangle_> - E_{\|o}]^{-1}$ becomes identical with the right side of equation (3.C.ii.10) in the limit $r_c^2 \to \infty$, and $T_{\|e}$ is substituted for $T_\|$.

Other manipulations of (D6) are also instructive; for instance

$$\frac{dQ_e}{dV_d} \cong L_p \int_{v_{\|o}}^{\infty} dv_\| \, f(v_\|) \tag{D8}$$

or

$$-\frac{d^2 Q_e}{dV_d^2} \cong \frac{eL_p}{m} f(v_{\|o})/v_{\|o} \tag{D9}$$

can yield detailed information about the tail of $f(v_\|)$. Of course, to avoid scale errors in the value of $v_{\|o} = \left[\frac{2e}{m}(V_d - \phi_o)\right]^{1/2}$, ϕ_o must be known. Both L_p and ϕ_o can be accurately determined via the density measurement.

APPENDIX E: Measurement of $h(v_\perp)$

This appendix describes a measurement technique which allows the measurement of an arbitrary perpendicular velocity distribution function $h(v_\perp)$. This measurement uses the same hardware as the $T_\perp$ measurement. In its present state of development, this measurement gives only a rough picture of $h(v_\perp)$, but with improvements in technique this measurement may become a precision tool.

We start the discussion by rewriting equation (3.C.i.1), the expression for the number of electrons which pass through the electrostatic analyzer cylinder and secondary magnetic field solenoid combination:

$$N(V_A, \gamma) = N_T \int_0^\infty dE_\perp \int_{-eV_A + \gamma E_\perp}^\infty dE_\parallel \, f(E_\parallel) \, h(E_\perp) \; ; \qquad (E1)$$

with the same notation as in section 3.C.4.i. We emphasize that N_T is the total number of electrons which could possibly pass through to the collector. We take the partial derivative with respect to the analyzer potential V_A:

$$\frac{\partial N}{\partial V_A} = eN_T \int_0^\infty dE_\perp \, h(E_\perp) \, f(-eV_A + \gamma E_\perp) \, . \qquad (E2)$$

If we can so arrange $f(E_\parallel)$, the parallel energy distribution of the dumped electrons, so that it approximates a delta function

162

$$f(E_\parallel) \sim \delta(E_\parallel - E_o) \qquad \text{(E.3)}$$

where E_o is the parallel energy of the dumped electrons, then

$$\frac{\partial N}{\partial V_A} \sim e N_T \int_0^\infty dE_\perp \, h(E_\perp) \, \delta(-eV_A + \gamma E_\perp - E_o) \qquad \text{(E.4)}$$

$$\sim \frac{e N_T}{\gamma} \, h\left(\frac{E_A - E_o}{\gamma}\right) \qquad \text{(E.5)}$$

where $E_A = -eV_A$. Thus, to the approximation $f(E_\parallel) = \delta(E_\parallel - E_o)$, the change in the fractional number of passed electrons at analyzer energy E_A is proportional to the perpendicular energy distribution evaluated at the energy difference $E_A - E_o$, which is then magnified by a factor of γ. It is trivial to convert $h(E_\perp)$ to the corresponding perpendicular velocity distribution $h(v_\perp)$:

$$h\left(\left[\frac{E_A - E_o}{m\gamma/2}\right]^{1/2}\right) = -\gamma m \frac{\partial}{\partial E_A}\left(\frac{N(E_A, \gamma)}{N_T}\right) \qquad \text{(E.6)}$$

Fortunately, dumping the electrons in such a way as to approximate a monoenergetic beam is simply accomplished. Consider the dump gate potential to be fixed at V_o. Any electron in the confined plasma can escape past the dump gate if its total parallel energy, $U_\parallel = -e\phi(r,z) + \frac{1}{2}mv_\parallel^2(r,z)$, exceeds $-eV_o \equiv E_o$. Let V_p be the potential applied to the cylinder in which the plasma is confined.

163

(Figure 2a schematically shows a confined plasma, and for this case V_p would be applied to L1-L5.) Initially, V_p is set at ground, and $U_{\parallel} < E_o$ for all electrons. As V_p is slowly made more negative, $U_{\parallel}$ is increased by $-eV_p$, and eventually $U_{\parallel}$ reaches E_o. At that time, the electron escapes past the barrier, and ends up with parallel kinetic energy $E_{\parallel} = U_{\parallel} = E_o$. Thus each electron that escapes has parallel kinetic energy $E_{\parallel} = E_o$.

The selective deconfinement of electrons is then completely analogous to that of the slow dumping procedure used for the $T_{\parallel e}$ diagnostic (see section 4.C.4.ii). In this case, however, the final energy distribution of the deconfined electrons is ideally the single value E_o. In practice, the beam energy has some finite spread in energy from E_o to $E_o + \Delta$. This spread is primarily due to the fact that the rate of the slowly changing potential applied to the containment cylinders is not infinitesimally small, and that the electron axial bounce frequency is not infinitely large. The measurement's resolution of the structure of $h(E_{\perp})$ is then limited to a scale length of approximately Δ/γ.

The relevant quantity in this measurement is the relative signal, $N(V_A; \gamma)/N_T$. Unfortunately, N_T is not just the total number of electrons on field lines which pass through the collimator hole. If this were true, the measurement of N_T would be simple and the fluctuation level of N_T would be quite small (on the order of one

percent). However, in practice, N_T is limited to only a few percent of the total possible by the onset of a diocotron instability driven by the slow hollowing out of the plasma column.[21] (This instability is also mentioned in the $T_{\|e}$ diagnostic section.)

Consequently, the plasma is dumped in such a way as to only allow the slow deconfinement to proceed over a fixed range of V_p. When the end of this range is reached, the V_p is rapidly switched back to ground, and no more electrons can escape confinement. N_T is then the number of electrons which pass through the collimator hole while the containment voltage is varied over the fixed range. The fluctuation level of N_T produced this way is on the order of 5-10%, and thus a great number of shots are needed to produce an accurate measurement of $h(v_\perp)$.

Although very little development work has been done on this measurement, its potential can be seen from Figure 32, which shows traces of $N(V_A, \gamma)$ (in arb. units) plotted against V_A for the same plasma at various times after a compression has occurred. The distribution function, $h(E_\perp)$, is simply given by the product of the slope of the $N(V_A, \gamma)$ data times $\gamma/eN(0, \gamma)$. The parameter γ is held at 1 for all traces except two, where γ is set to zero to show the approximate resolution. $N_T = N(0, \gamma)$ is the value of the signal as $V_A \to 0$ and all electrons can pass through the analyzer.
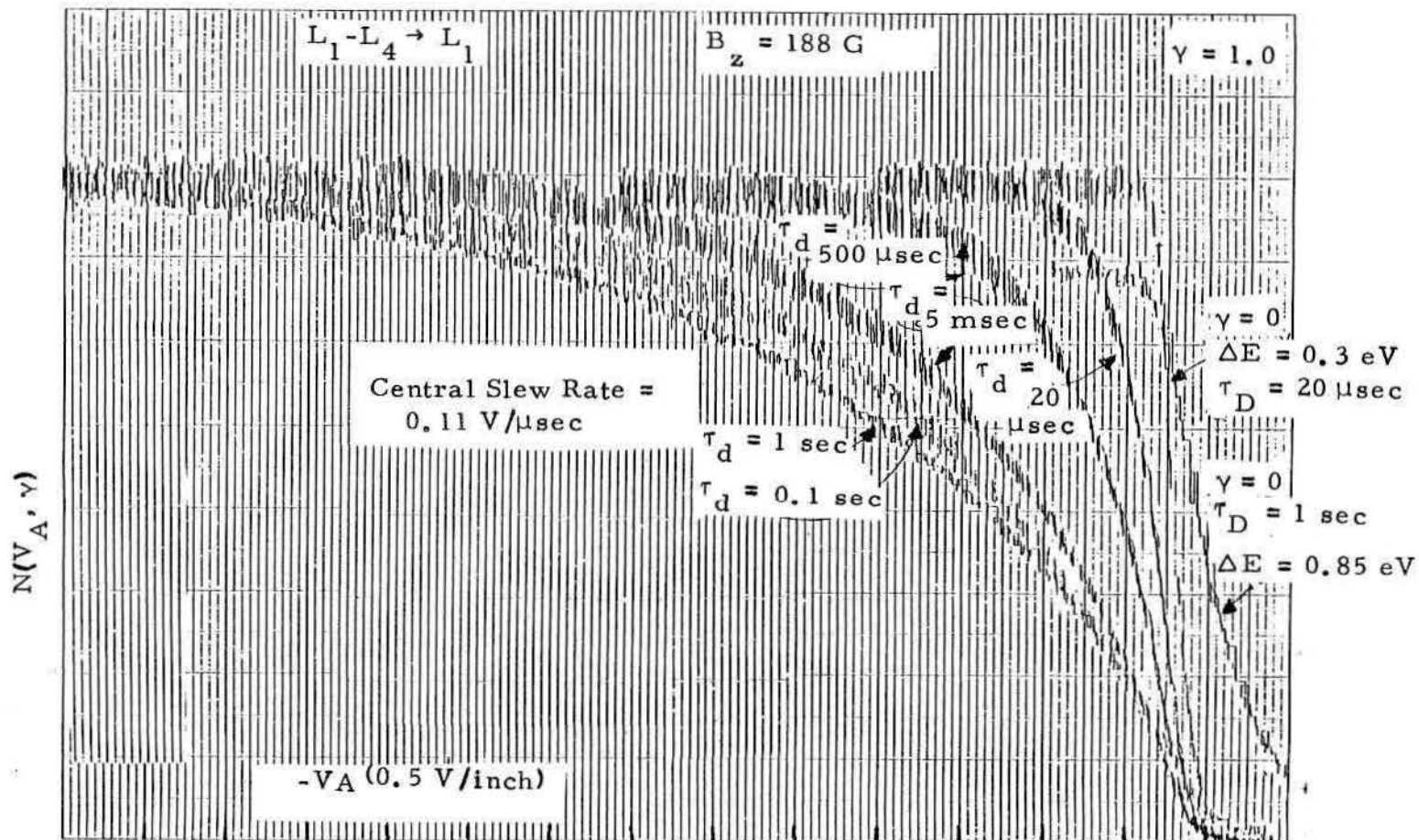
Figure 32. Plots of $N(V_A, \gamma)$ as functions of V_A. The plasma is initially compressed from L_1-L_4 into L_1 at $t=0$, and dumped at time τ_d for measurement of N. The collimator hole was centered on axis, and $\gamma=1$ for most of the shots. $B_z = 188$ G. There are two plots of $N(V_A, 0)$, which show the effective resolution width of the other plots. The plots were horizontally adjusted to line up at $N=0$, and vertically scaled to coincide at $N(0,0)$. The slope of each plot gives the perpendicular distribution $h(E_\perp)$ times a constant.

APPENDIX F: Polarization Drift

A time dependent radial electric field will impart a radial drift velocity to an electron in an axially magnetized plasma. This is a polarization drift, and can be thought of as arising from the effective azimuthal force an electron feels in an accelerated frame wherein the changing $\vec{E}_r \times \vec{B}$ azimuthal drift velocity is zero. This effective force is analogous to the centrifugal force of circular motion. The effective force in turn causes an $\vec{F} \times \vec{B}$ drift in that frame. For radial electric fields that vary in time, this results in a radial drift. This situation occurs naturally in the studied plasmas whenever they are compressed or expanded, and also during the dump process.

The magnitude of this polarization drift velocity is given by

$$v_p = - \frac{c}{\Omega B_z} \frac{d}{dt} E_r \, , \qquad (F1)$$

where Ω is the electron gyrofrequency and E_r is the radial electric field. The radial drift velocity of the gyro center is v_p. An estimate of the largest radial displacement expected from a dump, compress or expansion can be made by integrating (F1) to get

$$\Delta r = - \frac{c}{\Omega B_z} \Delta E \simeq \mp \frac{c}{\Omega B_z} E_r \, , \qquad (F2)$$

where ΔE has been approximated as $\sim \pm E_r$. E_r is approximated by the radial electric field from a uniform density plasma,

$$E_r = -2\pi e \, n_0 r \quad . \tag{F3}$$

Then, expressing the density, n_0, in terms of the plasma frequency, ω_p,

$$\Delta r \simeq \mp \frac{1}{2} \frac{\omega_p^2}{\Omega^2} r \quad . \tag{F4}$$

For the plasmas studied, $\omega_p^2/\Omega^2 < 10^{-2}$, but for plasmas near the Brillouin limit $(2\omega_p^2 = \Omega^2)$, Δr will be significant.

As long as the time rate of change of E_r is slow enough so that $\Omega^{-1} \ll E_r (dE_r/dt)^{-1}$, the gyromagnetic moment, μ, of the electron will remain constant. In our plasmas, the smallest $E_r (dE_r/dt)^{-1}$ is on the order of a microsecond, while $\Omega^{-1} \sim 1$ nanosecond. Thus $\mu = v_\perp^2/B$ remains constant, and when B is also constant, then $v_\perp^2$ is also constant. Therefore, even though the form of (F4) gives a uniform radial compression or expansion, there is no associated heating or cooling of the perpendicular degrees of freedom.

Of course, the dump process is much more complicated than a simple E_r, but the Δr associated with the dump is probably on the order of the estimate of (F4). This estimate gives a systematic error to our calculations of $n(r, z)$ and $\phi(r, z)$ on the order of $2(\Delta r/r)$; this is seen to be less than 1%. The closer the plasma gets to the Brillouin limit, the more consideration these errors must be given.

The systematic error in the $T_\perp$ measurement should be much smaller than 1%, since the measurement is basically a simple ratio of measured densities at constant r.

It is perhaps worth noting that this polarization displacement is necessary to conserve angular momentum. Since the compress, expand and dump processes are θ-symmetric, they impart no net torque to the plasma. The total canonical angular momentum of the plasma, $L_\theta = \sum_i r_i \left(P_{\theta i} - \frac{e}{c} A_\theta(r_i) \right)$, is then a constant. Here $\frac{e}{c} A_\theta(r_i) r_i = \frac{e}{c} \frac{B_z}{2} r_i^2$ is the field component of L_θ, and $r_i P_{\theta i} = m r_i^2 \dot{\theta}_i$ is the mechanical component, which consists of two parts; the individual gyromotion and the overall column rotation. The individual gyromotion portion remains fixed. The column rotation is determined by E_r, which is of course changed. Thus the change in L_θ due to the change in E_r must be balanced by a corresponding change in the field component; the mean square radius must change.